

**THE FIRST MEASUREMENT OF THE LEFT-RIGHT
CROSS SECTION ASYMMETRY
IN Z^0 BOSON PRODUCTION**

Ram Jacob Ben-David

SLAC-Report-442
May 1994

Prepared for the Department of Energy
under contract number DE-AC03-76SF00515

This document and the material and data contained therein, was developed under sponsorship of the United States Government. Neither the United States nor the Department of Energy, nor the Leland Stanford Junior University, nor their employees, nor their respective contractors, subcontractors, or their employees, makes any warranty, express or implied, or assumes any liability or responsibility for accuracy, completeness or usefulness of any information, apparatus, product or process disclosed, or represents that its use will not infringe privately-owned rights. Mention of any product, its manufacturer, or suppliers shall not, nor is it intended to, imply approval, disapproval, or fitness for any particular use. A royalty-free, nonexclusive right to use and disseminate same for any purpose whatsoever, is expressly reserved to the United States and the University.

THE FIRST MEASUREMENT OF THE LEFT-RIGHT
CROSS SECTION ASYMMETRY
IN Z^0 BOSON PRODUCTION

Ram Jacob Ben-David

*Stanford Linear Accelerator Center
Stanford University
Stanford, CA 94309*

May 1994

Prepared for the Department of Energy
under contract number DE-AC03-76SF00515

Printed in the United States of America. Available from the National Technical Information Service, U.S. Department of Commerce, 5285 Port Royal Road, Springfield, VA 22161.

ABSTRACT

The first measurement of the left-right cross section asymmetry (A_{LR}) in Z^0 boson production has been made with the SLAC Large Detector (SLD) at the SLAC Linear Collider (SLC). The measurement was performed at a center-of-mass energy (E_{cm}) of 91.55 GeV with a longitudinally polarized electron beam. The average beam polarization was $(22.4 \pm 0.6)\%$. Using a sample of 10,224 Z^0 decays, A_{LR} is measured to be $0.102 \pm 0.044(\text{stat}) \pm 0.003(\text{syst})$, which determines the effective electroweak mixing angle to be $\sin^2 \theta_W^{eff} = 0.2375 \pm 0.0056(\text{stat}) \pm 0.0004(\text{syst})$.

Acknowledgements

At this juncture in my life, I would like to take the opportunity to philosophize a bit (after all, I will soon be a *certified* philosopher) and to thank the people who have played active roles in helping me get to where I am today.

First, I would like to thank the members of my thesis committee: Professors Charlie Baltay, Kurt Gibble, Dimitri Kusnezov, Jack Sandweiss and Michael Schmidt, whose critiques of the initial draft of this thesis have led to a final version that is clearer and more concise. In addition, I'd like to thank my outside reader, Dr. Michael Murtagh, for being a good sport and taking the time to read my thesis.

I would especially like to thank my advisor, Charlie Baltay, for all his advice and encouragement. It was truly a pleasure learning the tricks of the trade from a master craftsman.

I would like to thank Steve Manly who superbly played the roles of advisor, colleague, and most importantly, friend. I would also like to thank Jack Sandweiss for the many insightful discussions about physics and life in general.

Many thanks to my SLD buddies: Phil Burrows, Richard Dubois, Scott Geary, Saul González, Sarah Hedges, Andrea Higashi and John Yamartino, for making my countless trips to SLAC so much fun. I would like to thank Peter Rowson, Morris Swartz, Hwanbae Park (my scanning buddy), Rob Elia, Mike Fero, Bruce Schumm and the rest of the Electroweak study group for all their help in the many aspects of this measurement. A special thanks goes to Peter, who not only seemed to never tire from my incessant questions: "Wait a minute, what about ...?", but would always have some witty response. To the rest of my SLD collaborators, those I had the privilege of working with and those I never met, I thank for making this experiment

possible through their hard work.

To my good friends Karen Ohl, Frank Rotondo and George Triantaphyllou, your friendship through the formative years of my becoming a particle physicist has meant a lot to me. Thanks to my office mate, Jeff Snyder, my comrade in the struggle to figure out the SLD software, only to have it change on us the following day.

I would like to thank Peter Martin and his supporting cast: Mary Kraus, Jean Ahern, Melissa Wiegand, Carole Devore and Brenda Alexy-Kuhn, who not only made my dealings with the Yale management and the outside world as painless as possible, but did it with a smile! I would also like to thank Will Emmet, Rochelle Lauer and John Sinnott for their excellent technical support. My deepest gratitude goes to Sara Batter and Jean Belfonti who have kept the best interests of the graduate students their number one priority.

A very special thanks goes to Aurel Faibis, Dani and Mina Ben-David, Norman Gelfand, Drasko Jovanovic and Dan Prober, whose presence at what in retrospect turned out to be the proverbial “fork(s) in the road” of my academic career, helped steer me down the path I eventually took.

To Arie Beck, my good friend from Tel Aviv University. I’ve always felt somewhat responsible for leading you down the path to high energy physics and then abandoning you to struggle on your own. I hope that in spite of that, you will find a niche where you will be happy.

I am truly indebted to my parents for making me what I am today. You have always tried to instill in me the principle that through hard work and determination I can achieve any goal I set for myself. I will be eternally grateful for your loving guidance throughout the years. I would also like to thank my family for all the love, support and patience you’ve had for me.

To Roni, my wife, your love, help, encouragement and ability to give so unselfishly of yourself over the years has played an essential role in my ability to achieve this goal. If it were not for your help in making many of the figures, typing in sections of text and proofreading this thesis, it would have taken me even longer to complete it. For all these reasons, I dedicate this thesis to you. I hope that someday, I will be able to return the favor.

This work has been funded, in part, by generous contributions from the RBD Fellowship Fund for Aspiring Husbands, contract K-061787.

Contents

Acknowledgements	v
List of Figures	xiii
List of Tables	xvii
1 Introduction	1
1.1 Definitions	2
1.1.1 Helicity States	2
1.1.2 Motion in Electromagnetic Fields	5
1.2 Theoretical Background	6
1.2.1 Electroweak Interactions	8
1.3 Longitudinally Polarized Cross Section	11
1.4 Electroweak Asymmetries	15
1.4.1 Left-Right Asymmetry	15
1.4.2 Forward-Backward Asymmetry	17
1.4.3 Polarized Forward-Backward Asymmetry	18
1.4.4 Discussion of A_{LR}	18
2 Experimental Apparatus	23
2.1 SLAC Linear Collider	23
2.1.1 Polarized Electron Source	24
2.1.2 Linear Accelerator	28
2.1.3 Energy Spectrometer	32

2.2	Polarimetry at SLAC	34
2.2.1	Compton Polarimeter	34
2.3	SLAC Large Detector	52
2.3.1	Vertex Detector	54
2.3.2	Drift Chamber	55
2.3.3	Cherenkov Ring Imaging Detector	57
2.3.4	Lead-Liquid Argon Calorimeter	60
2.3.5	Warm Iron Calorimeter	65
2.3.6	Luminosity Monitor	66
3	Event Selection	69
3.1	Trigger	70
3.2	Offline Filter	72
3.2.1	First Stage	74
3.2.2	Second Stage	78
3.2.3	Third Stage	79
3.2.4	Fourth Stage	80
3.3	Backgrounds	81
3.3.1	e^+e^- Interactions	82
3.3.2	Beam-Related and Cosmic-Ray Backgrounds	86
3.3.3	Background Estimation	88
4	Analysis	93
4.1	Experimental Systematic Uncertainties	93
4.1.1	Luminosity-weighted Average Polarization	94
4.1.2	Helicity Dependent Systematic Effects	95
4.1.3	Dependence on E_{cm} and Final States	99
4.2	Theoretical Uncertainties	102
4.2.1	Initial and Final State Radiative Corrections	102
4.2.2	QCD Contributions	102
4.2.3	Photon Vacuum Polarization Effects	103
4.3	Statistical Uncertainty	103

4.4	Result	103
5	Conclusions	105
5.1	Comparison with LEP	107
5.2	Comparison with Neutrino Measurements	109
5.3	Comparison with Atomic Measurements	109
5.4	Summary	110
5.5	Future Prospects	110

List of Figures

1.1	Fermion helicity states.	3
1.2	Helicity decomposition of vector and axial-vector interactions.	4
1.3	Gauge boson helicity states.	4
1.4	Weak-charged current interactions.	8
1.5	Neutral current interactions.	10
1.6	Allowed neutral current s -channel helicity combinations.	12
1.7	Lowest order diagrams for $e^+e^- \rightarrow \mu^+\mu^-$	12
1.8	Z^0 decays in the forward and backward regions of the detector.	17
1.9	Electroweak asymmetries versus $\sin^2 \theta_W$	20
1.10	Electroweak radiative corrections.	21
2.1	Polarized electron source.	24
2.2	GaAs conduction bands.	26
2.3	Effect of cesium on the electron work function.	27
2.4	Polarization of photoelectrons emitted from photocathodes.	28
2.5	Schematic of the SLAC Linear Accelerator (SLC)	29
2.6	The SLC damping ring.	31
2.7	Schematic of the SLC beam-energy spectrometer.	33
2.8	Feynman diagrams for Compton scattering.	35
2.9	Back-scattered Compton interaction.	36
2.10	Angular momentum diagrams for Compton scattering.	37
2.11	Angular momentum conservation in Compton back-scattering.	38
2.12	Compton interaction in the lab frame.	39
2.13	Overview of the SLD and the Compton polarimeter.	42

2.14	Schematic of the Compton polarimeter.	42
2.15	Compton electron detectors.	44
2.16	Compton analyzing powers.	51
2.17	Measured Compton asymmetry in the Cherenkov detector.	53
2.18	Quadrant view of the SLD.	54
2.19	Central drift chamber cell.	56
2.20	Schematic of the barrel CRID.	59
2.21	Schematic of the barrel CRID drift box.	60
2.22	Spectrum of measured Cherenkov angles in hadronic Z^0 decays.	61
2.23	The structure of a LAC cell.	62
2.24	Feynman diagram for the t -channel photon process.	67
2.25	Cell layout in the first LUM layer.	67
3.1	Example of hadronic Z^0 decay.	73
3.2	Example of a $\tau^+\tau^-$ final state.	74
3.3	Example of a e^+e^- final state.	75
3.4	Distributions of variables used in the first filter stage.	77
3.5	Scatter plot of E_{tot} versus E_{imb}	78
3.6	Scatter plot of S_4 versus Θ_{max} for all events passing the first stage.	79
3.7	Scatter plot of $\text{Min}(M_1, M_2)$ versus E_{imb}	80
3.8	E_{tot} for the final event sample.	81
3.9	Example of an $e^+e^- \rightarrow e^+e^-\gamma$ event	82
3.10	Endcap WAB event with leakage into the HAD layers.	83
3.11	WAB event in the barrel-endcap overlap region.	84
3.12	Feynman diagrams for (a) 2γ process and (b) $\gamma\gamma$ process.	85
3.13	Differential cross section for $e^+e^- \rightarrow \gamma\gamma$	86
3.14	High multiplicity SLC muon event.	87
3.15	Beam-gas/beam-wall event.	89
3.16	Cosmic-ray event.	90
4.1	Electron beam polarization for the final event sample.	94
4.2	Polarized Z^0 decays.	97

4.3	Energy dependence of A_{LR} for leptons and quarks.	100
4.4	Energy dependence of A_{LR} for hadrons and taus.	101
5.1	Comparison of A_e with LEP results.	108
5.2	Comparison of $\sin^2 \theta_W^{eff}$ with LEP results.	108
5.3	$\sin^2 \theta_W^{eff}$ (and M_W) versus m_t	111
5.4	$\sin^2 \theta_W^{eff}$ (and M_W) versus M_H	112
5.5	$\sin^2 \theta_W^{eff}$ (and M_W) versus Γ_{ee}	113

List of Tables

1.1	Standard model observables.	7
1.2	Weak quantum numbers.	9
1.3	Vector and axial-vector coupling constants.	11
1.4	m_t and M_H contributions to the radiative corrections of $\sin^2 \theta_W^{eff}$. . .	22
2.1	The SLC beam parameters measured during the 1992 run.	23
2.2	Systematic errors of the Compton polarimeter.	52
2.3	Vertex detector parameters.	55
2.4	Barrel CRID parameters.	58
2.5	Thickness of the LAC unit cells.	63
2.6	Readout structure of LAC layers.	63
2.7	Geometry of LAC barrel tiles.	64
3.1	The SLD trigger conditions.	71
3.2	Results of the background scan.	90
3.3	Results of the background analysis.	91
3.4	Summary of all types of background events.	92
4.1	Helicity dependent corrections to A_{LR}	99
4.2	Experimental uncertainties in the measurement of A_{LR}	104
4.3	Theoretical uncertainties in calculating A_{LR}	104
5.1	Corrections to A_{LR}	105

Chapter 1

Introduction

The left-right asymmetry, A_{LR} , is a direct manifestation of the parity violating nature of the weak interaction. The neutral-weak gauge boson, Z° , couples differently to the left-handed component of the weak-neutral current, J_μ^{NC} , than to its right-handed component. The difference arises from the $V - A$ (vector minus axial-vector) characteristic of the weak isotriplet currents, $J_\mu^i (i = 1, 2, 3)$. A pure $V - A$ interaction allows for the existence of only a left-handed weak-neutral current, J_μ^3 . However, the observed weak-neutral current, J_μ^{NC} , is an admixture of the $V - A$ interaction with the purely V interaction of the weak-hypercharge current, J_μ^Y . The V interaction contained in the weak-hypercharge current is responsible for the introduction of the right-handed component into the observed weak-neutral current. The amount of mixing between the $V - A$ and V interactions is parameterized as $\sin^2 \theta_W$, where θ_W is the Weinberg mixing angle. Measuring the difference in the coupling of the left-handed component of the weak-neutral current to the Z° relative to the coupling of the right-handed component of the weak-neutral current to the Z° is a direct measure of $\sin^2 \theta_W$.

At high energies, when the center-of-mass energy (E_{cm}) is ~ 100 GeV, radiative corrections resulting from virtual electroweak loops of particles, both known and unknown, cause the value of A_{LR} to vary from its tree level (without radiative corrections) value. Thus, a precision measurement of A_{LR} is sensitive to the masses of the top quark (m_t) and the Higgs boson (M_H), as well as to contributions from new

particles to these radiative loop corrections.

An overview of this thesis is as follows. This chapter will define terms and concepts used in the measurement of A_{LR} . In chapter 2, the accelerator, polarimeter and the SLD are described. The importance of the electron polarization and the detection of the Z^0 decays to the measurement of A_{LR} are highlighted in the sections describing the generation, transport and detection of the electron polarization, along with the section describing the lead-liquid argon calorimeter, used to detect the Z^0 decays. The criteria used to select events for this analysis are described in chapter 3. In chapter 4, the various systematic and theoretical uncertainties that go into the measurement are discussed and the result is calculated. Finally, in chapter 5, a comparison with other measurements is made and future prospects for the measurement are presented.

1.1 Definitions

Before becoming too involved with detailed calculations, it is important to develop some concepts and equations that will be used throughout this thesis.

1.1.1 Helicity States

1.1.1.1 Fermions

The equation of motion for a free fermion, of mass m , is derived from the Dirac equation

$$H\psi = (\boldsymbol{\alpha} \cdot \mathbf{p} + \beta m)\psi. \quad (1.1)$$

The four-component wavefunction ψ is an eigenstate of both the Hamiltonian H and the momentum operator \mathbf{p} . The 4×4 matrices $\boldsymbol{\alpha}$ and β are related to the Dirac γ matrices through the expression: $\gamma^\mu \equiv (\beta, \beta\boldsymbol{\alpha})$.

There is a two-fold degeneracy in the Dirac equation that gives rise to an additional observable. The operator

$$\boldsymbol{\Sigma} \cdot \hat{\mathbf{p}} = \begin{pmatrix} \boldsymbol{\sigma} \cdot \hat{\mathbf{p}} & 0 \\ 0 & \boldsymbol{\sigma} \cdot \hat{\mathbf{p}} \end{pmatrix}, \quad (1.2)$$

where $\hat{\mathbf{p}} \equiv \mathbf{p}/|\mathbf{p}|$ and $\boldsymbol{\sigma} \cdot \hat{\mathbf{p}}$, which gives the projection of the fermion's spin along its momentum direction, commutes with both H and \mathbf{p} . The operator $\frac{1}{2}\boldsymbol{\Sigma} \cdot \hat{\mathbf{p}}$ is called the helicity operator and has two eigenvalues, $\lambda = \pm\frac{1}{2}$, corresponding to the two helicity states in Fig. 1.1. Both Figs. 1.1(a) and 1.1(b) describe longitudinally



Figure 1.1: Fermion helicity states for (a) $\lambda = +\frac{1}{2}$ and (b) $\lambda = -\frac{1}{2}$.

polarized fermions. The $\lambda = +\frac{1}{2}$ state is referred to as a right-handed polarized (RH) state, where the spin is parallel to the direction of motion. Similarly, the $\lambda = -\frac{1}{2}$ state is referred to as a left-handed polarized (LH) state, where the spin is anti-parallel to the direction of motion.

For free particles, the wavefunction ψ can be written as

$$\psi = u(\mathbf{p})e^{-ip \cdot x}, \quad (1.3)$$

where $u(\mathbf{p})$ is a four-component spinor that will be written in the shorthand notation u (or u_f for a specific fermion).

It is useful to define the chirality projection operators

$$\mathbf{P}_R \equiv \frac{1}{2}(1 + \gamma^5) \quad \text{and} \quad \mathbf{P}_L \equiv \frac{1}{2}(1 - \gamma^5), \quad (1.4)$$

where the chirality operator γ^5 is equal to the product of the Dirac γ matrices: $i\gamma^0\gamma^1\gamma^2\gamma^3$. \mathbf{P}_R and \mathbf{P}_L project out the right- and left-handed chirality states of u :

$$u_R \equiv \frac{1}{2}(1 + \gamma^5)u \quad \text{and} \quad u_L \equiv \frac{1}{2}(1 - \gamma^5)u. \quad (1.5)$$

At high energies, $E \gg m$, the chirality operator is equal to $\boldsymbol{\Sigma} \cdot \hat{\mathbf{p}}$ [to $O(m/E)$] and the right- and left-handed chirality states are equal to the two respective helicity states. The vector current $\bar{u}\gamma^\mu u$ (where $\bar{u} \equiv u^\dagger\gamma^0$ describes the state of the scattered fermion) can be decomposed into RH and LH helicity states:

$$\bar{u}\gamma^\mu u = \bar{u}_R\gamma^\mu u_R + \bar{u}_L\gamma^\mu u_L, \quad (1.6)$$

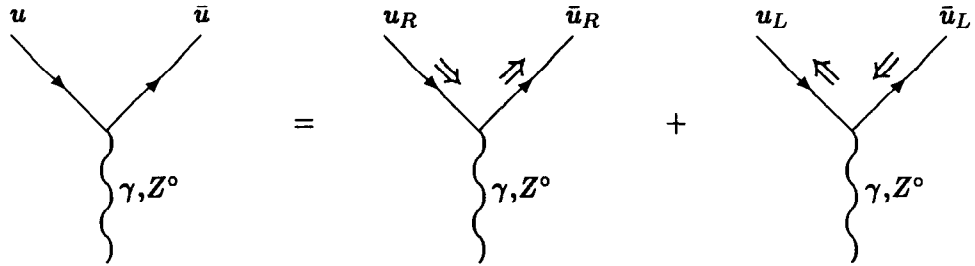


Figure 1.2: Helicity decomposition of vector and axial-vector interactions.

which are pictured schematically in Fig. 1.2. A similar decomposition can be done for axial-vector currents $\bar{u}\gamma^5\gamma^\mu u$. Thus, at high energies, both vector and axial-vector interactions conserve the helicity of the scattered fermion.

1.1.1.2 Gauge Bosons

Whereas λ described the spin-angular momentum states of $j_z = \pm 1/2$ for fermions, in the case of gauge bosons, the relevant longitudinal polarization or helicity states correspond to $j_z = \pm 1$.¹ The two polarization states are commonly called right-circularly polarized (RH), with $j_z = +1$, and left-circularly polarized (LH), with $j_z = -1$. Fig. 1.3 is a graphic representation of the two states.

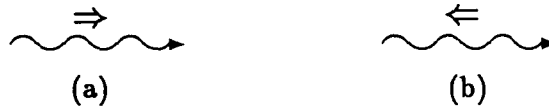


Figure 1.3: Gauge boson helicity states for (a) right-circularly polarized bosons and (b) left-circularly polarized bosons.

1.1.1.3 Polarization

The longitudinal polarization P of an ensemble of particles is defined as

$$P \equiv \frac{(\text{Number of RH particles}) - (\text{Number of LH particles})}{(\text{Number of RH particles}) + (\text{Number of LH particles})}, \quad (1.7)$$

obviously, $-1 \leq P \leq +1$.

¹The $j_z = 0$ state is allowed for massive gauge bosons, but will not come into play in this analysis.

1.1.2 Motion in Electromagnetic Fields

The equation of motion of the intrinsic spin \mathbf{s} of an electron in the laboratory system is given by the Thomas equation [1]

$$\frac{d\mathbf{s}}{dt} = \frac{e}{mc} \mathbf{s} \times \left[\left(\frac{g-2}{2} + \frac{1}{\gamma} \right) \mathbf{B} - \left(\frac{g-2}{2} \right) \frac{\gamma}{\gamma+1} (\boldsymbol{\beta} \cdot \mathbf{B}) \boldsymbol{\beta} - \left(\frac{g}{2} - \frac{\gamma}{\gamma+1} \right) \boldsymbol{\beta} \times \mathbf{E} \right], \quad (1.8)$$

where t , \mathbf{B} and \mathbf{E} are the time, magnetic field and electric field in the lab frame, e and m are the electron's charge and mass, $\boldsymbol{\beta}$ and γ are the Lorentz boost parameters and g is the gyromagnetic ratio of the electron.

The electron's equation of motion is

$$\frac{d\mathbf{p}}{dt} = e(\mathbf{E} + \boldsymbol{\beta} \times \mathbf{B}). \quad (1.9)$$

The solutions to these equations for two specific cases are of interest at the SLC.

$\boldsymbol{\beta}$ Colinear to \mathbf{B} and/or \mathbf{E} When the motion of the particle is along the direction of \mathbf{B} and/or \mathbf{E} , as is the case for linear accelerators,

$$\frac{d\mathbf{s}}{dt} = \mathbf{s} \times \left[\frac{e\mathbf{B}}{m\gamma} \right], \quad (1.10)$$

$$\frac{d\mathbf{p}}{dt} = e\mathbf{E}. \quad (1.11)$$

The spin precesses about the direction of motion and the particle is accelerated along the direction of motion.

$\boldsymbol{\beta}$ Transverse to \mathbf{B} At the SLC, particles are steered by passing them through dipole magnets, where the direction of motion is transverse to the magnetic field. Thus, the equations of motion reduce to

$$\frac{d\mathbf{s}}{dt} = \mathbf{s} \times \left[\frac{e}{mc} \left(\frac{g-2}{2} + \frac{1}{\gamma} \right) \mathbf{B} \right], \quad (1.12)$$

$$\frac{d\mathbf{p}}{dt} = \mathbf{p} \times \left[\frac{e}{mc\gamma} \mathbf{B} \right]. \quad (1.13)$$

Both \mathbf{s} and \mathbf{p} precess in the plane perpendicular to \mathbf{B} . However, they precess at different frequencies. Assuming \mathbf{s} and \mathbf{p} lie in the same plane, for every bend of angle θ_b that the momentum vector undergoes, \mathbf{s} will precess an additional $\Delta\theta$. The two are related through the relation

$$\Delta\theta = \left(\frac{g-2}{2}\right) \gamma\theta_b. \quad (1.14)$$

For $(g-2)/2 = (1.159652209 \pm 0.000000031) \times 10^{-3}$ and typical γ 's of 2,320 (energy of electron equal to 1.16 GeV, in the damping rings) and 88,063 (energy of electron equal to 45 GeV, in the arcs) this can lead to an appreciable deviation between the direction of the momentum vector and the spin vector.

1.2 Theoretical Background

The state of particle physics in 1993 can be accurately described by the $SU(3)_C \times SU(2)_L \times U(1)_Y$ theory of strong and electroweak interactions [2, 3]. This theory, combined with an isospin doublet of complex scalar fields that generates massive fermions and weak gauge bosons through the Higgs mechanism, makes up what is commonly called the minimal standard model (MSM).

At tree level, the dynamics of electroweak interactions in the MSM is determined by the three theoretical parameters: g , the weak-isospin coupling strength; g' , the weak-hypercharge coupling strength; and $\langle\phi_0\rangle$, the Higgs field vacuum expectation value. They are related to three observables that have been measured to high precision: α , the fine structure constant; G_F , the Fermi coupling constant; and M_Z , the mass of the Z° boson (see Table 1.1).

Because α and G_F are measured at lower energies than M_Z , one cannot directly solve the expressions for the three experimental observables in Table 1.1 for the three theoretical parameters. Before any comparison between the experimental observables and the theoretical parameters can be made, the effects of radiative corrections, resulting from virtual electroweak loops, to the tree level expressions must be included. These corrections introduce two more unknown parameters, the masses of the top quark (m_t) and the Higgs boson (M_H). In lieu of direct measurements of m_t and M_H ,

Experimental quantity	Theoretical expression [4]	Measured value [5, 6]	Relative error (ppm)
α	$\frac{1}{4\pi} \frac{g^2 g'^2}{\sqrt{g^2 + g'^2}}$	1/137.0359895(61)	0.045
G_F	$\frac{1}{\sqrt{2} \langle \phi_0 \rangle^2}$	$1.16639(2) \times 10^{-5} \text{ GeV}^{-2}$	17
M_Z	$\frac{1}{2} \langle \phi_0 \rangle \sqrt{g^2 + g'^2}$	91.187(7) GeV	77

Table 1.1: Standard model observables.

by making high precision measurements of two additional quantities, m_t and M_H can be constrained to be within certain values (in the absence of new physics).

Two quantities are prime candidates to be measured at the same energy as M_Z . The first is the mass of the W boson, M_W . At tree level, it is related to $\langle \phi_0 \rangle$ and g through the expression:

$$M_W = \frac{1}{2} \langle \phi_0 \rangle g. \quad (1.15)$$

When higher order loop corrections are included, M_W becomes sensitive to m_t and M_H .

The second quantity comes from the coupling of the vector and axial-vector components of a fermion-antifermion pair ($f\bar{f}$) weak-neutral current to the Z^0 . The vector and axial-vector coupling constants are

$$v_f = I_f^3 - 2Q_f \frac{g'^2}{g^2 + g'^2} \quad (1.16)$$

$$= I_f^3 - 2Q_f \sin^2 \theta_W, \quad (1.17)$$

$$a_f = I_f^3, \quad (1.18)$$

where I_f^3 is the third component of the weak isospin multiplet I (see Table 1.2) and Q_f is the charge of the fermion.² The ratio $g'^2/(g^2 + g'^2)$ is equal to $\sin^2 \theta_W$.

²Although v_f and a_f are two separate quantities, they are not measured individually. The different electroweak asymmetries measure the ratio of the two while the Z^0 decay widths of the different fermions measures their quadrature sum.

1.2.1 Electroweak Interactions

Electroweak interactions can be described by the symmetry group $SU(2)_L \times U(1)_Y$. The $SU(2)_L$ structure is made up of a weak-isotriplet of vector fields, $W_\mu^i (i = 1, 2, 3)$, that couple with strength g to weak-isotriplet currents, $J_\mu^i (i = 1, 2, 3)$. The $U(1)_Y$ weak-hypercharge symmetry group describes the coupling, with strength g' , of the weak-hypercharge vector field B_μ to the weak-hypercharge current J_μ^Y .

Weak-charged vector fields are created from linear combinations of W_μ^1 and W_μ^2 :

$$W_\mu^\pm = \sqrt{\frac{1}{2}}(W_\mu^1 \mp iW_\mu^2). \quad (1.19)$$

A positive (negative) weak-charged current interaction of W_μ^+ (W_μ^-) with an electron and neutrino is given by

$$\text{positive current: } -i\frac{1}{\sqrt{2}}g(J_\mu^+ W_\mu^+) = -i\frac{1}{\sqrt{2}}g[\bar{u}_\nu \gamma^\mu \frac{1}{2}(1 - \gamma^5)u_e]W_\mu^+, \quad (1.20)$$

$$\text{negative current: } -i\frac{1}{\sqrt{2}}g(J_\mu^- W_\mu^-) = -i\frac{1}{\sqrt{2}}g[\bar{u}_e \gamma^\mu \frac{1}{2}(1 - \gamma^5)u_\nu]W_\mu^-. \quad (1.21)$$

Fig. 1.4 shows a schematic representation of weak-charged current interactions with the vertex factor shown. The presence of \mathbf{P}_L in J_μ^\pm correctly describes the inherent left-hand nature of weak-charged currents.

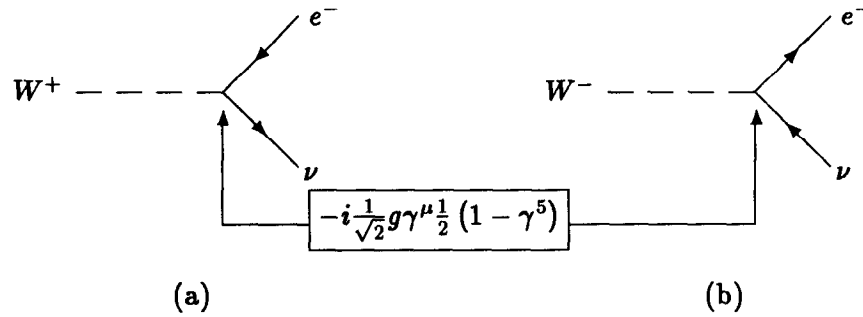


Figure 1.4: Weak-charged current interactions for (a) positive currents and (b) negative currents.

The neutral current interactions for any fermion-antifermion pair are expressed as

$$-igJ_3^\mu W_\mu^3 = -ig[\bar{u}_f \gamma^\mu \frac{1}{2}(1 - \gamma^5)I^3 u_f]W_\mu^3 \quad (1.22)$$

and

$$-ig'J_Y^\mu B_\mu = -ig'[\bar{u}_f\gamma^\mu Y u_f] B_\mu, \quad (1.23)$$

where the hypercharge Y is defined by the equation:

$$Q = I^3 + Y. \quad (1.24)$$

The electric charge of the particle is Q . Table 1.2 lists the values of I , I^3 , Q , and Y for the first generation of quarks and leptons (the quantum numbers for the remaining generations are the same).

Leptons	I	I^3	Q	Y	Quarks	I	I^3	Q	Y
ν_L	$\frac{1}{2}$	$\frac{1}{2}$	0	$-\frac{1}{2}$	u_L	$\frac{1}{2}$	$\frac{1}{2}$	$\frac{2}{3}$	$\frac{1}{6}$
e_L^-	$\frac{1}{2}$	$-\frac{1}{2}$	-1	$-\frac{1}{2}$	d_L	$\frac{1}{2}$	$-\frac{1}{2}$	$-\frac{1}{3}$	$\frac{1}{6}$
e_R^-	0	0	-1	-1	u_R	0	0	$\frac{2}{3}$	$\frac{2}{3}$
					d_R	0	0	$-\frac{1}{3}$	$-\frac{1}{3}$

Table 1.2: Weak quantum numbers for leptons and quarks.

The physically observed neutral interactions are not accurately described by W_μ^3 and B_μ . Instead, the physical fields are composed of linear combinations of W_μ^3 and B_μ :

$$A_\mu = B_\mu \cos \theta_W + W_\mu^3 \sin \theta_W, \quad (1.25)$$

$$Z_\mu = -B_\mu \sin \theta_W + W_\mu^3 \cos \theta_W. \quad (1.26)$$

The electromagnetic field A_μ is mediated by a massless vector boson, the photon. The neutral weak field Z_μ is mediated by the massive Z^0 vector boson. The amount of mixing between the neutral weak-isospin and weak-hypercharge fields is parameterized by θ_W .

Thus, by writing the electroweak-neutral interaction as

$$\begin{aligned} -igJ_3^\mu W_\mu^3 - ig'J_Y^\mu B_\mu &= -i \left(g \sin \theta_W J_3^\mu + g' \cos \theta_W J_Y^\mu \right) A_\mu \\ &\quad -i \left(g \cos \theta_W J_3^\mu - g' \sin \theta_W J_Y^\mu \right) Z_\mu \end{aligned} \quad (1.27)$$

$$= -ieJ_{em}^\mu A_\mu - i \frac{g}{\cos \theta_W} J_{NC}^\mu Z_\mu, \quad (1.28)$$

the term multiplying A_μ is identified as eJ_μ^{em} . The left-right symmetric electromagnetic current J_μ^{em} is

$$J_\mu^{em} = J_\mu^3 + J_\mu^Y \quad (1.29)$$

$$= \bar{u}_f \gamma^\mu Q_f u_f, \quad (1.30)$$

while the coupling strength e is

$$e = g \sin \theta_W = g' \cos \theta_W. \quad (1.31)$$

The weak-neutral current J_μ^{NC} can then be written as

$$J_\mu^{NC} = J_\mu^3 - \sin^2 \theta_W J_\mu^{em} \quad (1.32)$$

$$= \bar{u}_f \frac{1}{2} \underbrace{[\gamma^\mu (I_f^3 - 2\sin^2 \theta_W Q_f)]}_V - \underbrace{\gamma^\mu \gamma^5 I_f^3}_A u_f \quad (1.33)$$

$$= \bar{u}_f \gamma^\mu \frac{1}{2} [v_f - a_f \gamma^5] u_f, \quad (1.34)$$

where the V and A components have been isolated. Its coupling strength is $g/\cos \theta_W$.

The coupling strengths g and g' are not predicted by theory and must be determined by experiment. In practice, their values are inferred by experimental measurement of e and $\sin^2 \theta_W$.

A schematic representation of the neutral interactions is shown in Fig. 1.5 with the appropriate vertex factors. The vector and axial-vector coupling constants determine

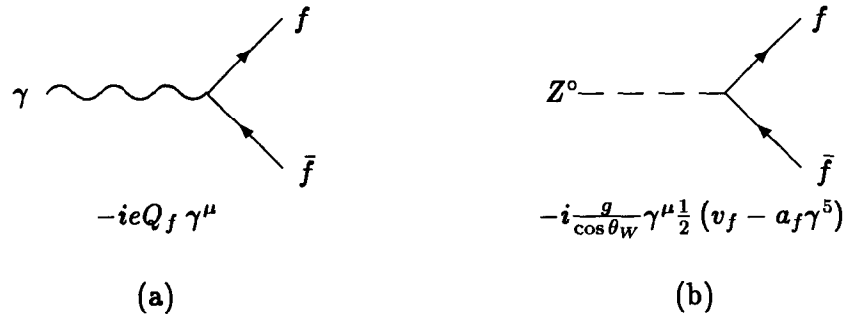


Figure 1.5: Neutral current interactions for (a) electromagnetic current interaction and (b) weak current interaction.

the relative strength that the V and A components of the fermion spinor couple to the Z° . To highlight the difference in the coupling of the RH and LH components of the fermion spinor to Z_μ , it is helpful to introduce the RH and LH coupling constants, g_R^f and g_L^f , that are linear combinations of v_f and a_f :

$$g_R^f \equiv v_f - a_f \quad \text{and} \quad g_L^f \equiv v_f + a_f. \quad (1.35)$$

Thus, the relevant portion of the vertex factor can be written as

$$v_f - a_f \gamma^5 = g_R^f \mathbf{P}_R + g_L^f \mathbf{P}_L, \quad (1.36)$$

where the $V - A$ character of the vertex has been rewritten as a sum of RH and LH projection operators, each with its own coupling strength. Table 1.3 lists the values of v_f , a_f , g_R^f , and g_L^f for the different particle flavors (for $\sin^2 \theta_W = 0.232$). Comparison of the magnitudes of g_R^f and g_L^f clearly shows the difference in the coupling of the RH and LH particles to the Z° , which gives rise to the left-right asymmetry.

Fermion flavor	v_f	a_f	g_R^f	g_L^f
ν_e, ν_μ, ν_τ	$\frac{1}{2}$	$\frac{1}{2}$	0	1
e^-, μ^-, τ^-	$-\frac{1}{2} + 2\sin^2 \theta_W = -0.04$	$-\frac{1}{2}$	0.46	-0.54
u, c, t	$\frac{1}{2} - \frac{4}{3}\sin^2 \theta_W = 0.19$	$\frac{1}{2}$	-0.31	0.69
d, s, b	$-\frac{1}{2} + \frac{2}{3}\sin^2 \theta_W = -0.35$	$-\frac{1}{2}$	0.15	-0.85

Table 1.3: Vector and axial-vector coupling constants.

1.3 Longitudinally Polarized Cross Section

In section 1.1 it was shown that at energies where $E \gg m$, vector and axial-vector interactions conserve the helicity of the incident fermion. Redrawing Fig. 1.2 in terms of the s -channel annihilation process exhibits the only allowed helicity combinations (see Fig. 1.6).

At the end of section 1.2.1, it was shown that the $e_L^+ e_R^-$ and $e_R^+ e_L^-$ couple with different strengths to the Z° . Those couplings are microscopic quantities. One infers

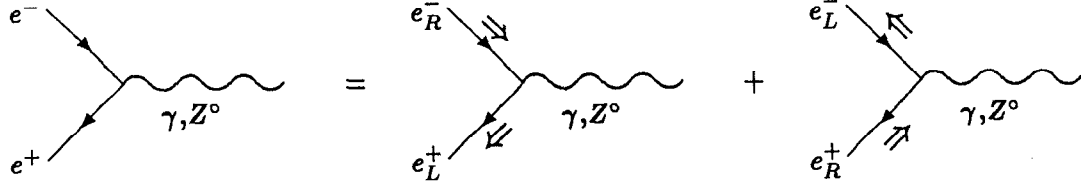


Figure 1.6: Allowed neutral current s -channel helicity combinations for $e_L^+ e_R^- \rightarrow \gamma$ or Z^0 and $e_R^+ e_L^- \rightarrow \gamma$ or Z^0 .

those microscopic quantities by measuring the macroscopic properties of electron and positron ensembles. This is done by polarizing the ensembles and measuring their cross section.

Consider the neutral current s -channel annihilation process $e^+ e^- \rightarrow \mu^+ \mu^-$ (the discussion will be the same for any $f\bar{f}$ pair except the $e^+ e^-$ that can scatter through the t -channel). The lowest order diagrams that contribute to the process are the electromagnetic and weak-neutral current interactions shown in Fig. 1.7.

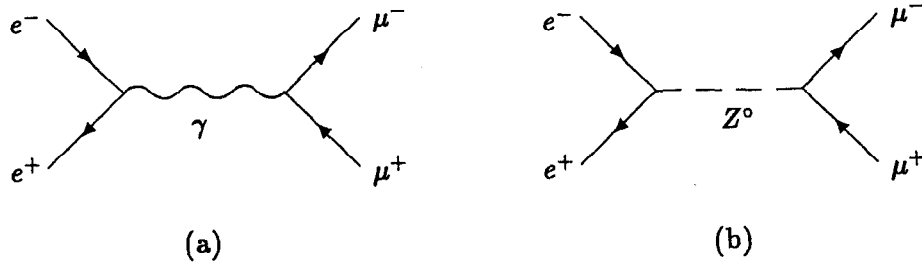


Figure 1.7: Lowest order (a) electromagnetic and (b) weak-neutral current diagrams for $e^+ e^- \rightarrow \mu^+ \mu^-$.

There are four different helicity combinations that make up the total cross section for the process. In the limit of negligible lepton masses ($\sqrt{s} \gg m_l$) their differential cross sections are [4]

$$\frac{d\sigma_{L1}}{d\Omega} \equiv \frac{d\sigma}{d\Omega}(e_R^+ e_L^- \rightarrow \mu_R^+ \mu_L^-) = \frac{\alpha^2}{4s} (1 + \cos\theta)^2 |Q_\mu + r g_{L2}^\mu g_L^e|^2, \quad (1.37)$$

$$\frac{d\sigma_{L2}}{d\Omega} \equiv \frac{d\sigma}{d\Omega}(e_R^+ e_L^- \rightarrow \mu_L^+ \mu_R^-) = \frac{\alpha^2}{4s} (1 - \cos\theta)^2 |Q_\mu + r g_{R2}^\mu g_L^e|^2, \quad (1.38)$$

$$\frac{d\sigma_{R1}}{d\Omega} \equiv \frac{d\sigma}{d\Omega}(e_L^+ e_R^- \rightarrow \mu_L^+ \mu_R^-) = \frac{\alpha^2}{4s} (1 + \cos\theta)^2 |Q_\mu + r g_{R2}^\mu g_R^e|^2, \quad (1.39)$$

$$\frac{d\sigma_{R2}}{d\Omega} \equiv \frac{d\sigma}{d\Omega}(e_L^+ e_R^- \rightarrow \mu_R^+ \mu_L^-) = \frac{\alpha^2}{4s} (1 - \cos\theta)^2 |Q_\mu + r g_L^\mu g_R^e|^2, \quad (1.40)$$

where

$$r = \frac{\sqrt{2} G_F M_Z^2}{s - M_Z^2 + i M_Z \Gamma_Z} \left(\frac{s}{e^2} \right), \quad (1.41)$$

$$s = E_{cm}^2, \quad (1.42)$$

Γ_Z is the width of the Z^0 resonance, Q_μ is the charge of the μ in units of e (this is left explicitly in the equations so that the generalization to all fermions will be easier) and θ is the angle the μ^- scatters relative to the direction of the incident e^- .

The unpolarized cross section is found by averaging over the initial states and summing over the final states. This is based on the assumption that all initial states are equally probable. When the initial state has a preferred orientation, as is the case with polarized beams, the initial states are added, weighted by the probability that the ensembles of electrons and positrons were prepared in that specific helicity configuration. Those probabilities are simply the number of RH (LH) electrons $N_R^-(N_L^-)$ and positrons $N_R^+(N_L^+)$ divided by the total number of electrons N^- and positrons N^+ , respectively. Thus, the cross section for polarized electrons and positrons is

$$\frac{d\sigma}{d\Omega} = \left(\frac{N_L^-}{N^-} \right) \left(\frac{N_R^+}{N^+} \right) \left(\frac{d\sigma_{L1}}{d\Omega} + \frac{d\sigma_{L2}}{d\Omega} \right) + \left(\frac{N_R^-}{N^-} \right) \left(\frac{N_L^+}{N^+} \right) \left(\frac{d\sigma_{R1}}{d\Omega} + \frac{d\sigma_{R2}}{d\Omega} \right). \quad (1.43)$$

N_R^-, N_L^-, N_R^+ and N_L^+ are related to the electron and positron polarizations, P_- and P_+ , through the expressions:

$$P_- \equiv \frac{N_R^- - N_L^-}{N_R^- + N_L^-} \quad \text{and} \quad P_+ \equiv \frac{N_R^+ - N_L^+}{N_R^+ + N_L^+}. \quad (1.44)$$

Eq. 1.43 can be rewritten as

$$\frac{d\sigma}{d\Omega} = \frac{1}{4} \left[(1 - P_- P_+) \frac{d\sigma_u}{d\Omega} + (P_+ - P_-) \frac{d\sigma_p}{d\Omega} \right], \quad (1.45)$$

where

$$\frac{d\sigma_u}{d\Omega} \equiv \frac{1}{4} \left[\left(\frac{d\sigma_{L1}}{d\Omega} + \frac{d\sigma_{L2}}{d\Omega} \right) + \left(\frac{d\sigma_{R1}}{d\Omega} + \frac{d\sigma_{R2}}{d\Omega} \right) \right], \quad (1.46)$$

$$\frac{d\sigma_p}{d\Omega} \equiv \frac{1}{4} \left[\left(\frac{d\sigma_{L1}}{d\Omega} + \frac{d\sigma_{L2}}{d\Omega} \right) - \left(\frac{d\sigma_{R1}}{d\Omega} + \frac{d\sigma_{R2}}{d\Omega} \right) \right]. \quad (1.47)$$

Each of the differential cross sections $\frac{d\sigma_u}{d\Omega}$ and $\frac{d\sigma_p}{d\Omega}$ has a contribution from the pure γ and Z^0 exchanges and the γ - Z^0 interference term. They can be decomposed into the following components:

$$\frac{d\sigma_u}{d\Omega} = \frac{d\sigma_u^\gamma}{d\Omega} + \frac{d\sigma_u^{\gamma Z}}{d\Omega} + \frac{d\sigma_u^Z}{d\Omega}, \quad (1.48)$$

where

$$\frac{d\sigma_u^\gamma}{d\Omega} = \left(\frac{\alpha^2}{4s}\right) Q_\mu^2 [1 + \cos^2 \theta], \quad (1.49)$$

$$\begin{aligned} \frac{d\sigma_u^{\gamma Z}}{d\Omega} = \left(\frac{\alpha^2}{4s}\right) \frac{1}{2} Q_\mu^2 \text{Re}(r) \{ & [1 + \cos^2 \theta] [g_L^e + g_R^e] [g_L^\mu + g_R^\mu] \\ & + 2 \cos \theta [g_L^e - g_R^e] [g_L^\mu - g_R^\mu] \}, \end{aligned} \quad (1.50)$$

$$\begin{aligned} \frac{d\sigma_u^Z}{d\Omega} = \left(\frac{\alpha^2}{4s}\right) \frac{1}{4} |r|^2 \{ & [1 + \cos^2 \theta] [(g_L^e)^2 + (g_R^e)^2] [(g_L^\mu)^2 + (g_R^\mu)^2] \\ & + 2 \cos \theta [(g_L^e)^2 - (g_R^e)^2] [(g_L^\mu)^2 - (g_R^\mu)^2] \}, \end{aligned} \quad (1.51)$$

and

$$\frac{d\sigma_p}{d\Omega} = \frac{d\sigma_p^\gamma}{d\Omega} + \frac{d\sigma_p^{\gamma Z}}{d\Omega} + \frac{d\sigma_p^Z}{d\Omega}, \quad (1.52)$$

where

$$\frac{d\sigma_p^\gamma}{d\Omega} = 0, \quad (1.53)$$

$$\begin{aligned} \frac{d\sigma_p^{\gamma Z}}{d\Omega} = \left(\frac{\alpha^2}{4s}\right) \frac{1}{2} Q_\mu^2 \text{Re}(r) \{ & [1 + \cos^2 \theta] [g_L^e - g_R^e] [g_L^\mu + g_R^\mu] \\ & + 2 \cos \theta [g_L^e + g_R^e] [g_L^\mu - g_R^\mu] \}, \end{aligned} \quad (1.54)$$

$$\begin{aligned} \frac{d\sigma_p^Z}{d\Omega} = \left(\frac{\alpha^2}{4s}\right) \frac{1}{4} |r|^2 \{ & [1 + \cos^2 \theta] [(g_L^e)^2 - (g_R^e)^2] [(g_L^\mu)^2 + (g_R^\mu)^2] \\ & + 2 \cos \theta [(g_L^e)^2 + (g_R^e)^2] [(g_L^\mu)^2 - (g_R^\mu)^2] \}, \end{aligned} \quad (1.55)$$

with

$$\text{Re}(r) = \frac{\sqrt{2} G_F M_Z^2 (s - M_Z^2)}{(s - M_Z^2)^2 + M_Z^2 \Gamma_Z^2} \left(\frac{s}{e^2}\right), \quad (1.56)$$

$$|r|^2 = \frac{2 (G_F M_Z^2)^2}{(s - M_Z^2)^2 + M_Z^2 \Gamma_Z^2} \left(\frac{s}{e^2}\right)^2. \quad (1.57)$$

When $\sqrt{s} = M_Z$ the γ - Z^0 interference terms drop out and $\frac{d\sigma_Z^Z}{d\Omega} \gg \frac{d\sigma_\gamma^Z}{d\Omega}$. At the SLC, only the electrons are polarized ($P_+ = 0$). Generalizing eq. 1.45 to all fermion final states (exclusive of the e^+e^- final state), the cross section for longitudinally polarized electrons can be written as

$$\begin{aligned} \frac{d\sigma}{d\Omega} = & \left(\frac{\alpha^2}{4s}\right) \frac{1}{2} \frac{(G_F M_Z^2)^2}{(s - M_Z^2)^2 + M_Z^2 \Gamma_Z^2} \left(\frac{s}{e^2}\right)^2 \times \\ & \left\{ [(g_L^e)^2 + (g_R^e)^2] [(g_L^f)^2 + (g_R^f)^2] (1 + \cos^2 \theta) \right. \\ & + [(g_L^e)^2 - (g_R^e)^2] [(g_L^f)^2 - (g_R^f)^2] (2 \cos \theta) \\ & - P_- [(g_L^e)^2 - (g_R^e)^2] [(g_L^f)^2 + (g_R^f)^2] (1 + \cos^2 \theta) \\ & \left. - P_- [(g_L^e)^2 + (g_R^e)^2] [(g_L^f)^2 - (g_R^f)^2] (2 \cos \theta) \right\}. \end{aligned} \quad (1.58)$$

It is interesting to note that two of the terms have even spatial parity and two have odd parity, while two terms are even under a sign change in the polarization and two are odd.

1.4 Electroweak Asymmetries

Given the polarized cross section in eq. 1.58, one can isolate the various coupling constants by measuring asymmetries of the cross section.

1.4.1 Left-Right Asymmetry

The left-right asymmetry A_{LR} is defined as the ratio of the difference of the helicity cross sections, $\sigma_L \equiv \sigma(e_R^+ e_L^- \rightarrow Z^0)$ and $\sigma_R \equiv \sigma(e_L^+ e_R^- \rightarrow Z^0)$, for Z^0 production to the total cross section.

This is simply the ratio of odd to even polarization components, with even spatial parity:

$$A_{LR} \equiv \frac{\sigma_L - \sigma_R}{\sigma_L + \sigma_R} \quad (1.59)$$

$$= \frac{(g_L^e)^2 - (g_R^e)^2}{(g_L^e)^2 + (g_R^e)^2} = \frac{2v_e a_e}{v_e^2 + a_e^2} = \frac{2(1 - 4\sin^2 \theta_W)}{1 + (1 - 4\sin^2 \theta_W)^2} \quad (1.60)$$

$$= A_e, \quad (1.61)$$

where

$$\sigma_L \equiv \int_{-1}^{+1} \frac{d\sigma(P_- = -1)}{d(\cos \theta)} d(\cos \theta) \quad \text{and} \quad \sigma_R \equiv \int_{-1}^{+1} \frac{d\sigma(P_- = +1)}{d(\cos \theta)} d(\cos \theta). \quad (1.62)$$

A_{LR} has been expressed in several common notations. For the present discussion, the most illuminating notation is that of the RH and LH coupling constants. It clearly shows that A_{LR} is a direct measure of the difference in the strength that the Z^0 couples to LH electrons versus its coupling to RH electrons. For $|P_-| < 1$, the experimentally measured asymmetry is

$$A_{LR}^{exp} = P_- A_{LR} = \frac{N_L - N_R}{N_L + N_R}, \quad (1.63)$$

where $N_R(N_L)$ is the number of RH (LH) Z^0 decays observed in the detector. In addition, it has been assumed that the luminosities for RH and LH electrons are equal. The case when this assumption is not valid will be dealt with in section 4.1.2.

In practice, the integrals of eq. 1.62 must be modified to include the effects of the detector's response function³ $\epsilon_f(\theta, \phi)$ to the final state fermion. The integrands in eq. 1.62 are replaced with the product of the differential cross section and the detector's response function. The integrals of terms in the expression for the differential cross section (eq. 1.58) that are linear in $\cos \theta$ will equal zero only if either:

- $\epsilon_f(\theta, \phi) = \epsilon_f(\pi - \theta, \pi + \phi)$: the detector's response function has even spatial parity,

or

- $\epsilon_f(\theta, \phi) = \epsilon_{\bar{f}}(\theta, \phi)$: the detector's response function to fermions is equal to that of antifermions, $\epsilon_{\bar{f}}(\theta, \phi)$.

Quantitatively, all that is being said is that the two Z^0 decay modes depicted in Fig. 1.8 have an equal probability of being detected. The SLD has an azimuthally symmetric solenoidal magnetic field which ensures the equality of the response to particles and antiparticles, even in the presence of detector nonuniformities. In addition,

³The detector's response function parameterizes the detector's acceptance and efficiency at detecting the final state fermion of a specific decay mode. Each decay mode can have a different $\epsilon_f(\theta, \phi)$.

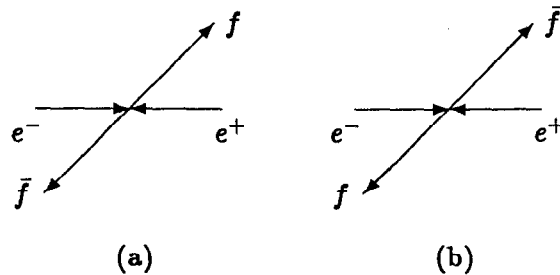


Figure 1.8: Z^0 decays with the final state fermion in the (a) forward and (b) backward regions of the detector.

the SLD calorimeter has a high degree of uniformity and polar symmetry so that the detector's response function is even under parity transformations. Therefore, both conditions are satisfied and the integrals of terms in the differential cross section that are linear in $\cos \theta$ are equal to zero.

1.4.2 Forward-Backward Asymmetry

For unpolarized beams, the forward-backward asymmetry for a final state fermion f , A_{FB}^f , is defined as the ratio of the difference of cross sections between detecting the final state fermion in the forward region ($\cos \theta > 0$) and backward region ($\cos \theta < 0$) to the total cross section (see Fig. 1.8). This is just the ratio of odd parity to even parity components that are even in polarization:

$$A_{FB}^f \equiv \frac{\sigma_F - \sigma_B}{\sigma_F + \sigma_B} \quad (1.64)$$

$$= \frac{3}{4} \frac{[(g_L^e)^2 - (g_R^e)^2]}{[(g_L^e)^2 + (g_R^e)^2]} \frac{[(g_L^f)^2 - (g_R^f)^2]}{[(g_L^f)^2 + (g_R^f)^2]} \quad (1.65)$$

$$= \frac{3}{4} A_e A_f, \quad (1.66)$$

where

$$\sigma_F \equiv \int_0^{+1} \frac{d\sigma}{d(\cos \theta)} d(\cos \theta) \quad \text{and} \quad \sigma_B \equiv \int_{-1}^0 \frac{d\sigma}{d(\cos \theta)} d(\cos \theta). \quad (1.67)$$

To measure A_{FB}^f one must be able to identify the final state decay particles. This has only been done for the three lepton channels and the heavier quarks, b and c ,

whose presence can be separated, with limited efficiency and purity, from the other quark channel decays.

1.4.3 Polarized Forward-Backward Asymmetry

When the electrons are polarized, it is possible to isolate the coupling constants of the final state fermion f by forming the polarized forward-backward asymmetry $A_{FB}^{pol,f}$ that is the ratio of terms that are odd and even in the product of the spatial parity and polarization:

$$\begin{aligned} A_{FB}^{pol,f} &\equiv \frac{[\sigma_F(P_- = -1) - \sigma_F(P_- = +1)] - [\sigma_B(P_- = -1) - \sigma_B(P_- = +1)]}{[\sigma_F(P_- = -1) + \sigma_F(P_- = +1)] + [\sigma_B(P_- = -1) + \sigma_B(P_- = +1)]} \\ &= \frac{\sigma(P_- \cos \theta < 0) - \sigma(P_- \cos \theta > 0)}{\sigma(P_- \cos \theta < 0) + \sigma(P_- \cos \theta > 0)} \end{aligned} \quad (1.68)$$

$$= \frac{3}{4} \left[\frac{(g_L^f)^2 - (g_R^f)^2}{(g_L^f)^2 + (g_R^f)^2} \right] \quad (1.69)$$

$$= \frac{3}{4} A_f, \quad (1.70)$$

where $\sigma(P_- \cos \theta)$ is shorthand notation for the integrals of the preceding equation.

1.4.4 Discussion of A_{LR}

The following are some of the highlights of the A_{LR} measurement:

- It is a simple measurement. One just has to detect Z^0 decays and the corresponding initial electron polarization state, independent of the final state⁴ (excluding the e^+e^- final state⁵).

– 96% of all *visible* decays contribute. This is compared to only ~4% of *visible* decays for either A_{FB}^μ or A_{FB}^b .⁶

⁴This is correct up to terms of $O[(\Gamma_Z/M_Z)^2]$ that are not shown in the denominator of eq. 1.59. Their contribution will be discussed in section 4.1.3.

⁵The e^+e^- final state, which contributes ~4% to the overall *visible* decays, is omitted for reasons that will be discussed in section 3.2.

⁶The fraction of all *visible* Z^0 's that decay into $\mu^+\mu^-$ is ~4%. The fraction of all *visible* Z^0 's that decay into $b\bar{b}$ is ~19%. It is assumed that the b or \bar{b} is detected through a semileptonic decay mode that will include a e^\pm or μ^\pm in the decay products. These decay modes account for 21.4% of all b or \bar{b} decays [7].

Since virtually all final states contribute, there is almost no systematic error that results from measuring a specific Z^0 decay mode. The only significant source for systematic errors in A_{LR} is from the measurement of the electron polarization which is completely decoupled from the measurement of the Z^0 's. The uncertainty in measuring A_{LR} is given by

$$\delta A_{LR} = \sqrt{\frac{1 - (A_{LR}^{exp})^2}{(P_-)^2 N}} \oplus A_{LR} \left(\frac{\delta P_-}{P_-} \right), \quad (1.71)$$

where N is the total number of Z^0 's detected. The first term is the statistical error and the second is the systematic error resulting from the measurement of the polarization. With enough statistics, one is limited only by the precision of measuring the electron polarization.

- It is a robust measurement that is insensitive to:
 - Acceptance effects (as long as one isn't preferentially accepting RH or LH polarized Z^0 's).
 - Resolution effects: one does not need to have a high resolution detector, one only needs to be able to differentiate between Z^0 decays and any background event present in the detector.
 - Luminosity inefficiency: one does not necessarily have to detect an extremely high percentage of the events, as long as there is no left-right bias in the detected events.
- There is a small theoretical uncertainty (see section 4.2), dominated by the uncertainty in calculating the value of α at the Z^0 mass:

$$\delta A_{LR}^{theory} = 0.0025. \quad (1.72)$$

- It is insensitive to initial state radiative corrections.
- Compared with the other asymmetries, it combines three desired traits in the most favorable way.

- Magnitude: A_{LR} is larger than the other asymmetries (except for $A_{FB}^{pol,b}$) making it easier to measure experimentally.
- Sensitivity to $\sin^2 \theta_W$: A_{LR} is the most sensitive of all asymmetries to $\sin^2 \theta_W$ (see Fig. 1.9).

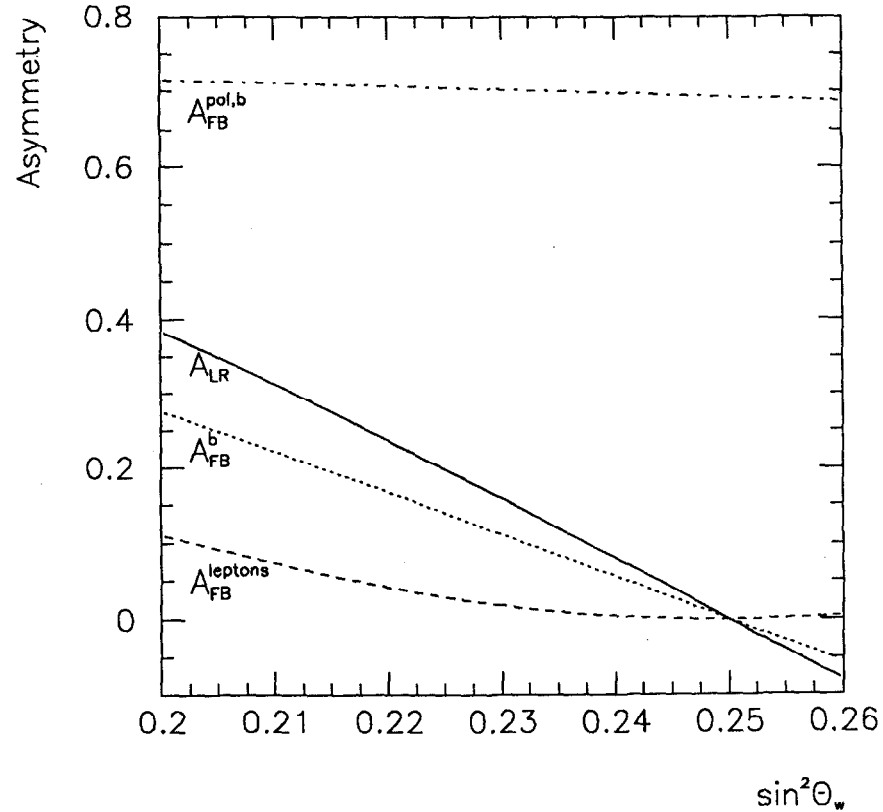


Figure 1.9: Electroweak asymmetries versus $\sin^2 \theta_W$.

- Independence of final states: Because A_{LR} is virtually independent of the final state, it is the least sensitive of the asymmetries to QCD corrections, making it perfectly suited for precision tests of the electroweak sector of the MSM.
- The enhanced sensitivity to $\sin^2 \theta_W$ makes A_{LR} very sensitive to virtual electroweak corrections and new particles that come into the loop corrections shown in Fig. 1.10. This point will be discussed in section 1.4.4.1.

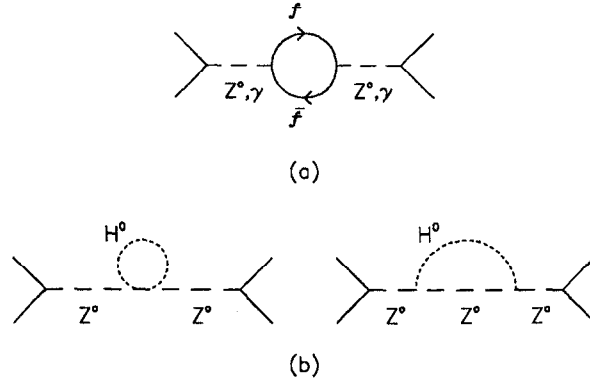


Figure 1.10: (a) Oblique electroweak radiative corrections and (b) Higgs loops corrections.

1.4.4.1 Radiative Corrections

It has become conventional to absorb the effects of radiative corrections into the vector and axial-vector coupling constants, thereby creating “effective” coupling constants [8]. Redefining the couplings in such a manner allows the different observables to maintain their tree-level forms. Using these effective couplings A_{LR} becomes

$$A_{LR} = \frac{2v_e^{eff} a_e^{eff}}{(v_e^{eff})^2 + (a_e^{eff})^2} = \frac{2(1 - 4\sin^2 \theta_W^{eff})}{1 + (1 - 4\sin^2 \theta_W^{eff})^2}, \quad (1.73)$$

where

$$a_e^{eff} = -\frac{1}{2} \left(1 + \frac{\Delta\rho}{2} \right), \quad (1.74)$$

$$v_e^{eff} = a_e^{eff} [1 - 4(1 + \Delta k)s_0^2] \quad (1.75)$$

$$= a_e^{eff} [1 - 4\sin^2 \theta_W^{eff}]. \quad (1.76)$$

The quantities $\Delta\rho$ and Δk contain all the electroweak radiative corrections not included in the photon vacuum polarization contribution. The quantity s_0^2 is equal to the tree level $\sin^2 \theta_W$ (defined in eq. 1.17) corrected only for photon vacuum polarization effects (contained in $\Delta\alpha$) in the following manner:

$$s_0^2(1 - s_0^2) = \frac{\pi}{\sqrt{2}G_F M_Z^2} \left(\frac{\alpha}{1 - \Delta\alpha} \right). \quad (1.77)$$

For $(1 - \Delta\alpha)/\alpha = 128.8 \pm 0.1$ [9], $s_0^2 = 0.23136$. Thus, $\sin^2 \theta_W^{eff}$ is given by

$$\sin^2 \theta_W^{eff} = s_0^2(1 + \Delta k). \quad (1.78)$$

The electroweak radiative corrections are related by the expression:

$$\Delta\rho \approx -\left(\frac{c_0^2 - s_0^2}{c_0^2}\right) \Delta k. \quad (1.79)$$

In the limit of large m_t , $\Delta\rho$ can be broken up into two components:

$$\Delta\rho = \Delta\rho_t + \Delta\rho_H, \quad (1.80)$$

with

$$\begin{aligned} \Delta\rho_t &\approx \frac{3G_F}{8\pi^2\sqrt{2}} m_t^2 \\ &= 0.0026 \left(\frac{m_t}{M_Z}\right)^2, \end{aligned} \quad (1.81)$$

$$\begin{aligned} \Delta\rho_H &\approx -\frac{3G_F M_W^2 \tan^2 \theta_W}{8\pi^2\sqrt{2}} \ln\left(\frac{M_H^2}{M_Z^2}\right) \\ &= -0.0006 \ln\left(\frac{M_H^2}{M_Z^2}\right). \end{aligned} \quad (1.82)$$

Note the quadratic dependence on m_t while there is only a logarithmic dependence on M_H . The difference arises from the way each is accounted for in the loop calculations of Fig. 1.10. Table 1.4 shows how various values of m_t and M_H contribute to Δk .

$m_t(\text{GeV})$	Δk	$M_H(\text{GeV})$	Δk
100	-0.0045	100	+0.0002
150	-0.0101	200	+0.0014
200	-0.0179	1000	+0.0041

Table 1.4: m_t and M_H contributions to the radiative corrections of $\sin^2 \theta_W^{eff}$.

Thus, to be sensitive to m_t and M_H , $\sin^2 \theta_W^{eff}$ must be measured to a precision of $\sim 0.1\%$. As previously stated, this measurement alone is not enough to “measure” m_t and M_H , it is only one piece of the puzzle and must be aided by other measurements. Ideally, if the top quark were discovered, a precision measurement of $\sin^2 \theta_W^{eff}$ would then place constraints on possible values of M_H . Any inconsistencies with other measurements would signal new physics beyond the MSM.

Chapter 2

Experimental Apparatus

2.1 SLAC Linear Collider

During the 1980's, SLAC's (Stanford Linear Accelerator Center) two-mile-long linear accelerator (linac) was modified to simultaneously accelerate bunches of longitudinally polarized electrons and unpolarized positrons to an energy of approximately 50 GeV and then collide them head-on. The modified linear collider (SLC) [10, 11] produces Z^0 's at rest, which promptly decay. The decay properties of the Z^0 are measured by the detector surrounding the interaction point (IP). Average values for some basic SLC parameters, measured at the IP during the 1992 run, are listed in Table 2.1.

E_{cm}	91.55 GeV
Number of e^- 's/bunch	3×10^{10}
Number of e^+ 's/bunch	3×10^{10}
Bunch area (e^- and e^+)	$2\mu\text{m} \times 2\mu\text{m}$
Bunch length (e^- and e^+)	1.2 mm
Luminosity	$0.9 \times 10^{29}/\text{cm}^2\text{s}$ 10 Z^0 's/hr
e^- polarization	22.4%

Table 2.1: The SLC beam parameters measured during the 1992 run.

2.1.1 Polarized Electron Source

Longitudinally polarized electron bunches are created by directing a photon beam, of a given helicity state, at a Gallium-Arsenide (GaAs) photocathode. The photocathode emits polarized bunches of electrons that are fed into the accelerator.

2.1.1.1 Polarized Light Source

The polarized light source (PLS) [12] component of the polarized electron source, is shown in Fig. 2.1. The laser is a flashlamp-pumped dye laser which produces a 5 mJ pulse for 750 ns at a rate of 120 Hz and a wavelength of 715 nm.

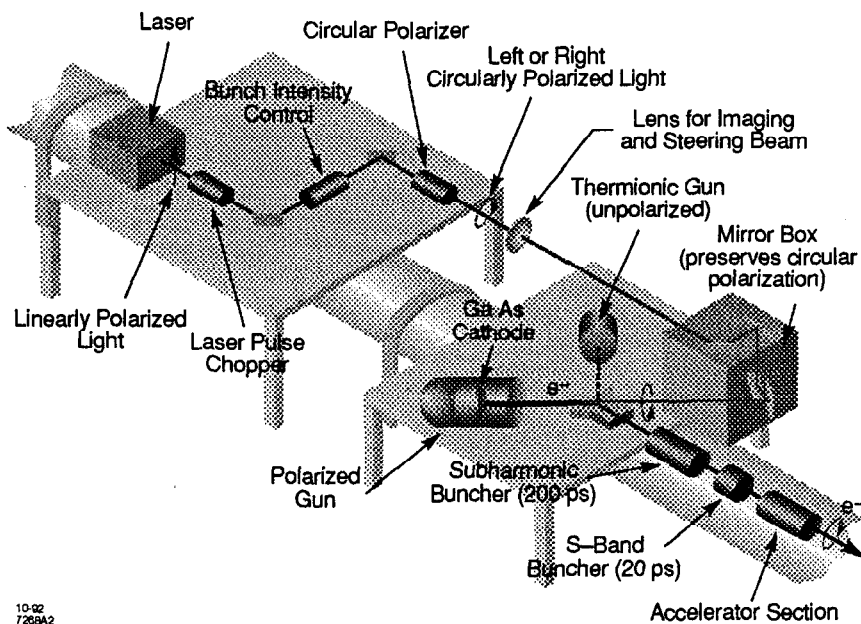


Figure 2.1: Polarized electron source [12].

As will be described in section 2.1.2, for each electron bunch that reaches the IP, another electron bunch is needed to create a positron bunch. In order to create two electron bunches from one laser pulse, each pulse is divided into two pulses by the laser pulse chopper (LPC). The LPC consists of two orthogonal polarizers separated by a Pockels cell.¹ When turned on, the Pockels cell turns the linearly polarized

¹A Pockels cell is an electro-optical device that varies the birefringence of a crystal linear to the

light into circularly polarized light, which then has a component along the axis of the second polarizer. When the Pockels cell is off, no light passes through the LPC because the light remains linearly polarized, perpendicular to the second polarizer. By toggling the voltage applied to the Pockels cell, the original laser pulse has been divided into two 2 ns pulses, separated by 60 ns.

The intensity of light striking the photocathode is regulated by the bunch intensity control (BIC). The BIC is composed of the same components as the LPC, except that the polarizers are aligned. By varying the voltage of the Pockels cell, one can add a component to the polarized light that will be removed when the light passes through the second polarizer. The laser beam energies are typically reduced to 5 μ J.

To produce circularly polarized light, the linearly polarized light passes through another Pockels cell. In order to reduce systematic effects, the voltage applied to the cell is randomly toggled between positive and negative voltages, giving positive- and negative-helicity states (respectively). The applied voltage is recorded and used in the later stages of the analysis.

The circularly polarized light enters a 20 m long transport line where it is focused by a 6 m focal length lens and redirected to the photocathode by 4 polarization compensating mirrors (the photons remain in the same helicity state).

The laser light striking the photocathode is 99% circularly polarized. By monitoring the emitted electron beam, it is determined that the helicity intensity has an asymmetry of less than 5×10^{-4} .

2.1.1.2 Polarized Electron Cathode

The photocathode is a 5 mm thick piece of GaAs, 18 mm in diameter, cut from a 3 in wafer. Absorption of the PLS photons raises the electrons in the valence band to the conduction band (Fig. 2.2) where a 120 kV voltage applied to the cathode removes the electrons from the cathode and begins to accelerate them [13, 14].

The left diagram in Fig. 2.2 shows the energy band structure versus the crystal momentum.² At the bottom of the diagram are the valence bands. The conduction

voltage applied to it. Typical response times are less than 10 ns.

²A force applied to an electron will produce a change, with respect to time, in the electron's

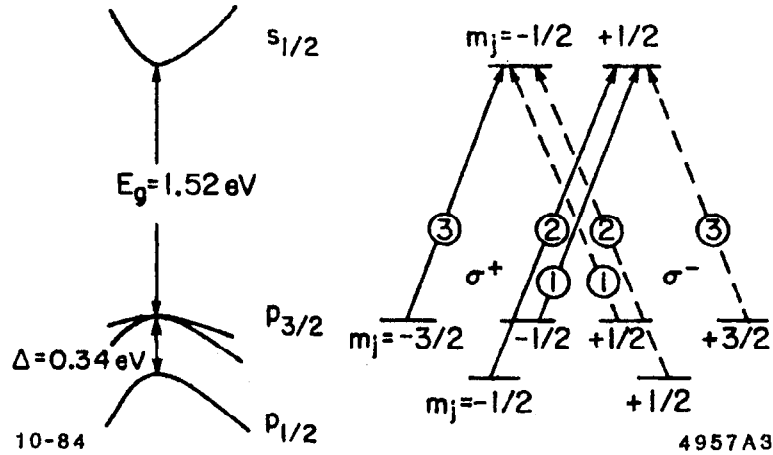


Figure 2.2: GaAs conduction bands [14].

band is separated from the valence band by a 1.52 eV band gap. The right diagram shows the allowed energy transitions for the absorption of a spin one photon with the relative transition rates in circles. The solid (dashed) arrows correspond to the absorption of a RH (LH) photon. The different transition rates between the angular momentum states are calculated using Clebsch-Gordan coefficients.

Absorption of a RH photon with $j_z = +1$ and energy between 1.52 eV and 1.86 eV (PLS photons have an energy of 1.73 eV) will lead to the transition of an electron from the $P_{3/2}(m_j = -3/2)$ state to $S_{1/2}(m_j = -1/2)$ state three times more often than the transition $P_{3/2}(m_j = -1/2)$ to $S_{1/2}(m_j = 1/2)$. This produces a net polarization of the electrons in the conduction band of 50% $\left(\frac{3-1}{3+1}\right)$. The direction of the emitted electron is opposite that of the incident photon. Thus, an emitted electron with spin $m_j = -1/2(+1/2)$ corresponds to a RH (LH) electron.

Once the electrons have been raised to the conduction band, they need to be extracted from the crystal. To accomplish this, the work function must be overcome (Fig. 2.3(a)). Because GaAs is a poor emitter, increasing the electric field does not

momentum. The electron's *crystal momentum* is defined to account only for the time derivative of momentum due to external fields and not the periodic fields of the lattice [15].

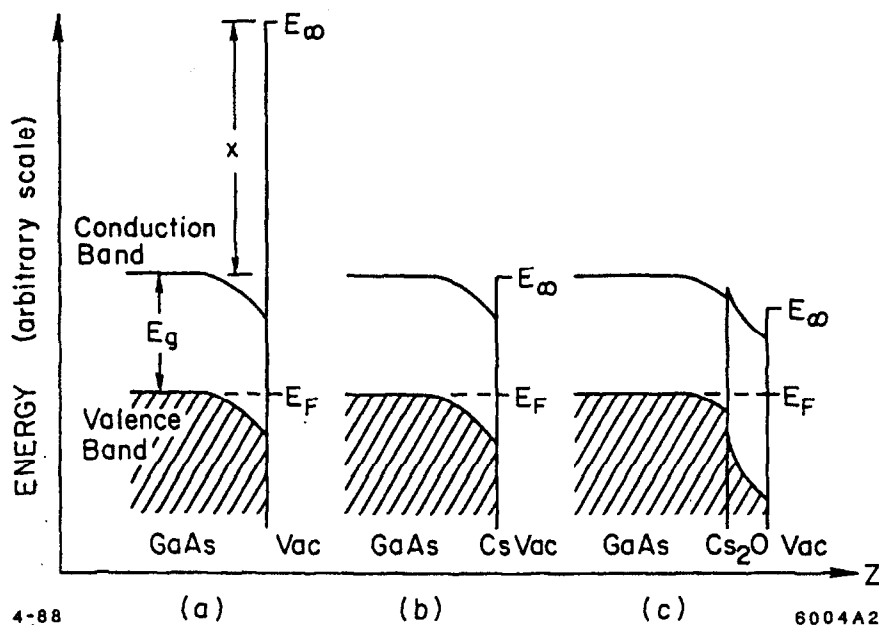


Figure 2.3: Effect of cesium on the electron work function [14].

help very much. Coating the cathode with cesium lowers the free electron state (E_{∞}) to the conduction band (Fig. 2.3(b)). Coating the cathode with a thin layer of Cs_2O causes E_{∞} to become lower than the conduction band, allowing the electrons to be easily removed (Fig. 2.3(c)). In practice, cesium and NF_3 were deposited in alternate layers on the GaAs to lower the gap below the conduction band.

Fig. 2.4 is a plot of the polarization of several photocathodes versus the laser wavelength. For the 1992 run, it was decided to be conservative and use the bulk GaAs cathode which had given consistent results in test setups (the other cathodes were still under development and were not deemed reliable enough to be used for the actual run). The photoelectrons, created within the crystal, interact with the atoms of the crystal as they make their way to the surface. These interactions lead to a depolarization of the electrons. The maximum polarization attained with the bulk GaAs cathode was 28%.

The other photocathodes shown in the plot achieve higher polarization by using a thinner cathode and/or straining the cathode, in order to break the degeneracy of the $P_{3/2}$ state. In the 1993 SLD run, the strained GaAs source was used in conjunction

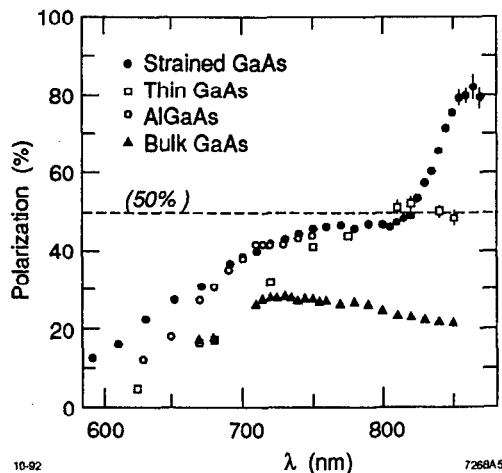


Figure 2.4: Polarization of photoelectrons emitted from photocathodes.

with a higher wavelength laser producing an average polarization of $\sim 62\%$ at the IP.

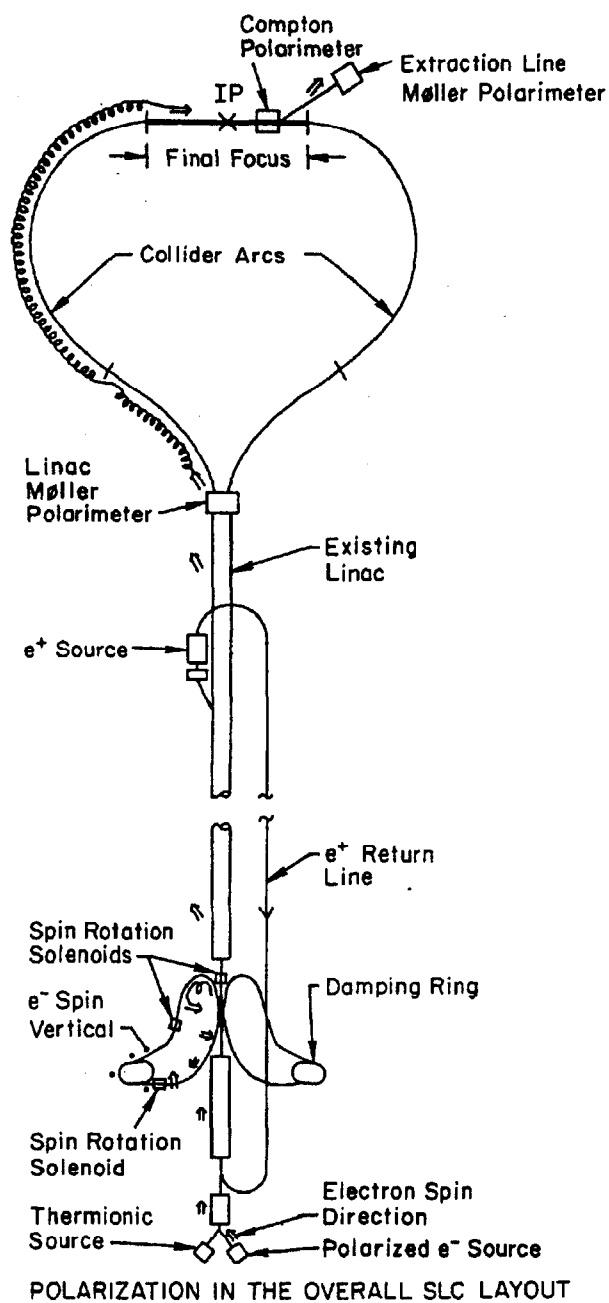
Aside from polarization, another unit of merit used to judge a photocathode is its quantum efficiency (QE). The quantum efficiency is defined as

$$QE \equiv \frac{\text{number of photoemitted electrons}}{\text{number of incident photons}}. \quad (2.1)$$

The quantum efficiency of the bulk GaAs photocathode varied between (8-10)%, directly after cesiation, and 3%, before the cathode was recesiated. The process is repeated every 5 to 7 days. The cathode produced 4×10^{10} electrons per pulse [11].

2.1.2 Linear Accelerator

At any given moment there are several electron and positron bunches in the accelerator. In order to understand the full cycle of operation at the SLC (see Fig. 2.5), begin with one positron bunch followed by two electron bunches as they are extracted from their respective damping rings and fed into the linac. The first two bunches (one of positrons and the leading electron bunch) continue down the linac and are accelerated to 47 GeV. At the end of the linac, they are separated, the positrons go into the right arc, while electrons are steered into the left arc. In the left arc, the electron spin precesses a net 26 times, arriving longitudinally polarized at the IP. The final



10-86

5571A4

Figure 2.5: Schematic of the SLC. Arrows indicate the electron spin orientation, while the loops represent the electron spin precession in the arc.

focus magnets reduce the beam spot sizes from $250 \mu\text{m} \times 30 \mu\text{m}$, to $2 \mu\text{m} \times 2 \mu\text{m}$ before colliding the bunches at the IP. The particles that do not interact are transported to a beam dump where their energy is measured (see section 2.1.3). Before the electrons reach the beam dump, their polarization is measured by the Compton polarimeter (see section 2.2.1).

The third bunch (of electrons) is accelerated to 30 GeV and then diverted from the linac to a tungsten-rhenium target. The interaction of the bunch with the target creates a shower of electrons, positrons and photons. Low energy positrons (~ 1 MeV) are selected and brought back to the beginning of the linac. Then, along with the two electron bunches from the polarized source, they are accelerated to 1.16 GeV and sent into their respective damping rings.

The 35 m circumference damping rings are designed to reduce the emittance of the electron (positron) bunches by a factor of 10 (30). One (two) machine cycle, 8 (16) msec, passes before the electrons (positrons) are fed back into the linac and the process is repeated.

For electrons, an additional beam parameter that needs to be dealt with in the damping ring is the longitudinal polarization. In eq. 1.14, it was shown that the electron spin does not rotate the same amount as the momentum vector when passing through a bend magnet. For an electron bunch of a single energy, this is not catastrophic. One needs to count the number of times the bunch goes around the ring in order to calculate the direction of the electron spin upon exiting the ring. However, in reality, the electrons arrive at the damping ring with an energy spread, which would cause the bunch to become depolarized. To remedy this problem, the electron spin is rotated from the horizontal plane to the vertical plane, where it maintains its polarization, in spite of the rotations in the damping ring (see eq. 1.12).

To rotate the electron spin, the electrons are sent through a series of five dipole magnets in the linac-to-ring (LTR) transfer line (see Fig. 2.6). Each rotates the momentum vector by 32.8° , thereby rotating the electron spin by 90° . After passing through the five magnets, the electron spin has precessed 450° in the horizontal plane and is perpendicular to the direction of motion. The electrons then pass through a

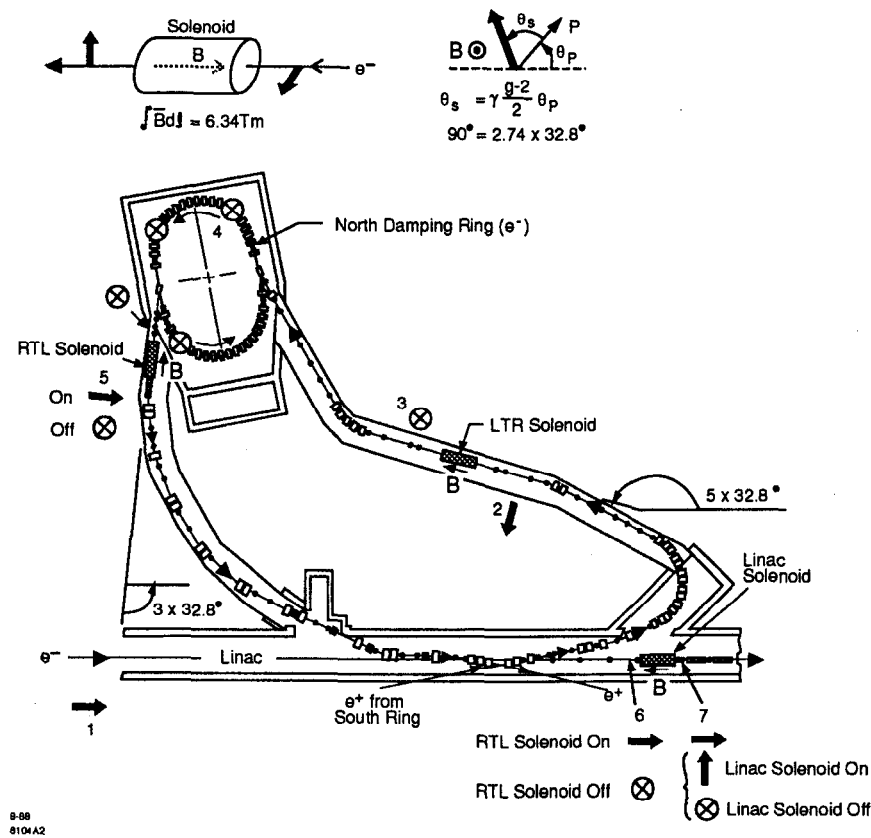


Figure 2.6: The SLC damping ring.

superconducting magnet with a solenoidal field, which rotates the spin into the vertical direction. Upon exiting the damping ring, the electrons pass through two more solenoids in the ring-to-linac (RTL) transfer line. Between the two RTL solenoids, virtually any spin orientation is achievable. This large degree of freedom is necessary because the arcs are aplanar and the spin precesses in both the horizontal and vertical planes. The RTL solenoids are tuned to match the arc rotations so that the spin will be longitudinally polarized at the IP.

It is worthwhile to note that electrons and positrons, when held in storage rings, can become transversely polarized through the emission of synchrotron radiation [14]. The asymptotic limit (in time) for transverse polarization is 92.38%. It would take on the order of an hour for the transverse polarization to reach the 90% level in the SLC

damping rings. At the SLC, the electrons (positrons) spend only one (two) machine cycles, 8 (16) msec, in the damping ring. This results in a negligible increase in the transverse polarization of less than $(2 \times 10^{-3})\%$ for either the electrons or positrons. Thus, the electron's polarization will not increase by a noticeable amount and the positrons will effectively remain unpolarized.

Depolarizing Effects There are three sources for spin depolarization at the SLC. The first is a result of running the damping rings below their design energy of 1.21 GeV. Because the magnets saturate at the design energy, the damping rings were run at 1.16 GeV. This caused the electron spin to rotate only 431.7° (instead of 450°) in the LTR. The component of the spin left parallel to the direction of motion was lost in the damping ring. The transmission factor of $\cos(18.3^\circ) = 0.95$ leads to a relative decrease in the polarization of 5%. The second source of depolarization comes from the arcs. The mean bunch energy has a ~ 0.25 GeV spread [16], while the energy spread within a bunch is ~ 0.14 GeV [17]. After precessing a net $26 \times 2\pi$ radians, the transmission factor for the arc is ~ 0.85 . The third and least significant depolarization effect arises from beam-beam interactions at the IP. The beams deflect each other by ~ 1 mrad [18]. From eq. 1.14, the transmission factor is found to be ~ 0.995 .

The overall transmission factor is the product of the three, ~ 0.80 . Thus, for an electron bunch with 28% polarization at the photocathode, the polarization after the IP is $\sim 22\%$.

2.1.3 Energy Spectrometer

The electron and positron beam energies are measured by a pair of energy spectrometers (one for each beam) [19]. Each spectrometer is located 150 m past the IP, just before the beam dumps. The energy of the beam is measured by bending the beams through an analyzing magnet and measuring the angle by which the beams are deflected (see Fig. 2.7). The beam energy is related to the deflection angle θ by the

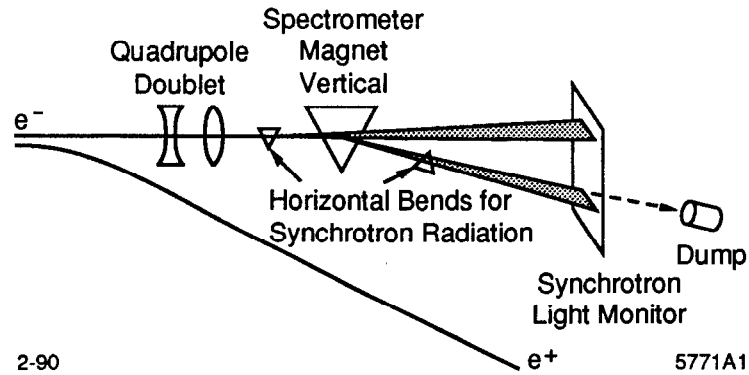


Figure 2.7: Schematic of the SLC beam-energy spectrometer.

expression:

$$E_{beam} = \frac{e}{\theta} \int |d\mathbf{l} \times \mathbf{B}|, \quad (2.2)$$

where \mathbf{B} is the magnetic field of the analyzing magnet and \mathbf{l} lies along the path length.

To measure the angle of deflection, the beam is sent through a series of three dipole magnets. The first and third magnets bend the beam in the same plane, causing the beam to radiate parallel stripes of synchrotron radiation, while the second (analyzing) magnet bends the beam in the perpendicular plane by 18.286 mrad. The synchrotron stripes hit the wire imaging synchrotron radiation detector (WISRD) 15 m away. By measuring the distance between the two synchrotron stripes, one measures the scattering angle and thus, the energy.

Each WISRD detector is made up of two screens. Each screen contains 96 copper wires that are 75 μm wide and are spaced 100 μm apart (center to center). The wires are strung parallel to the synchrotron stripes. The synchrotron radiation Compton scatters electrons in the wires. The residual charge on the wires is sampled by a charge sensitive preamplifier, then amplified, shaped, digitized and read out. Typically, the synchrotron stripes will be spread out over 10 to 30 wires.

The quadrupole magnets located before the dipole magnets focus the beams to a point on the second screen in order to minimize the effect of the beams going through the screen.

A simulation of the beam transport system, predicts that 47.8 MeV is lost due to synchrotron radiation when 45.7 GeV beams are transported from the IP to the energy spectrometer. It is estimated that the absolute systematic uncertainty in measuring E_{cm} is 40 MeV.

2.2 Polarimetry at SLAC

The two techniques used at the SLC to measure the electron polarization are e^-e^- (Møller) and $e^-\gamma$ (Compton) scattering. Because of the poorer resolution of the Møller polarimeter ($\Delta P_-/P_- = 5\%$), it was only used as a diagnostic check of the Compton polarimeter ($\Delta P_-/P_- = 2.7\%$) and will not be described here (see ref. [14] for a thorough presentation of the technique). In addition, the location of the Compton polarimeter, relative to the IP, makes it a more desirable choice. The Møller polarimeter, located at the end of the linac,³ does not measure spin depolarization in arcs (see Fig. 2.5).

2.2.1 Compton Polarimeter

The Compton polarimeter measures the polarization of the electron beam by measuring the asymmetry in scattering RH and LH circularly polarized photons off polarized electrons.

2.2.1.1 Theoretical Background

Compton scattering is the scattering of photons off electrons. To lowest order, the process can be described by two Feynman diagrams, the s -channel (Fig. 2.8(a)) and the u -channel (Fig. 2.8(b)).

Electron polarization is measured by studying electrons that are back-scattered (at an angle of 180° relative to the angle of incidence) in the cm frame. Before discussing the specific measurement, some of the expected physical properties are calculated [14, 20].

³The extraction line Møller polarimeter was not fully implemented for this run.

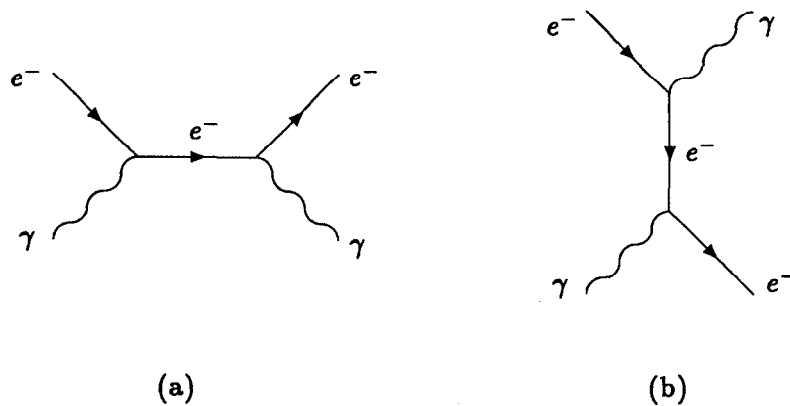


Figure 2.8: Compton scattering Feynman diagrams for (a) s -channel and (b) u -channel processes.

First, because of some existing incorrect and ambiguous derivations in the literature for polarized Compton scattering, a short derivation, as described in ref. [20] is presented. It will be shown that the differential cross section for back-scattered electrons is larger for parallel incident helicity states ($j_z = \pm 3/2$) than for anti-parallel helicity states ($j_z = \pm 1/2$).

The derivation consists of three steps. The first step is to show that for the special case of back-scattered electrons in the center of mass (cm) frame, the amplitude for the u -channel is larger. The Feynman propagator in the u -channel is proportional to $1/(u - m_e^2)$ while the s -channel propagator is proportional to $1/(s - m_e^2)$. In the cm frame, the four-vectors describing the interaction are

$$\begin{aligned}
 p_\mu^{cm} &= (E_{cm}, 0, 0, p_{cm}), \\
 k_\mu^{cm} &= (k_{cm}, 0, 0, k_{cm}), \\
 (p_\mu^{cm})' &= (E_{cm}, 0, 0, -p_{cm}), \\
 (k_\mu^{cm})' &= (k_{cm}, 0, 0, -k_{cm}).
 \end{aligned} \tag{2.3}$$

A schematic representation of this information is shown in Fig. 2.9. By definition, in the cm frame p_{cm} equals $-k_{cm}$. The denominator of the u -channel propagator is given by

$$u - m_e^2 = [p_\mu^{cm} - (k_\mu^{cm})']^2 - m_e^2 = m_e^2 - 2p_{cm}(E_{cm} - p_{cm}) - m_e^2$$



Figure 2.9: Back-scattered Compton interaction in the (a) initial state and (b) final state.

$$\begin{aligned}
 &\approx -m_e^2 \\
 &= -2.6 \times 10^{-7} \text{ GeV}^2.
 \end{aligned} \tag{2.4}$$

The invariant s is the total energy squared in any frame. In the lab frame, for a 45.7 GeV electron (E) and 2.33 eV photon (k), the four-vectors used to calculate s are

$$\begin{aligned}
 p_\mu &= (E, 0, 0, p), \\
 k_\mu &= (k, 0, 0, k), \\
 p'_\mu &= (E', 0, 0, -p'), \\
 k'_\mu &= (k', 0, 0, -k').
 \end{aligned} \tag{2.5}$$

The denominator of the s -channel propagator is

$$\begin{aligned}
 s - m_e^2 &= (p_\mu + k_\mu)^2 - m_e^2 = (E + k)^2 - (\vec{p} + \vec{k})^2 - m_e^2 \\
 &\approx 4Ek \\
 &= 4.3 \times 10^{-7} \text{ GeV}^2.
 \end{aligned} \tag{2.6}$$

Therefore, the u -channel amplitude is larger than that of the s -channel.

Next, the coupling of the electron and photon helicity states to each channel is analyzed. Since the electron-photon system does not have orbital angular momentum, the spin angular momentum must be conserved ($\Delta j_z = j_z^{\text{initial}} - j_z^{\text{final}} = 0$). The photon has a spin of one and the electron has a spin of 1/2. If angular momentum is to be conserved when the electron is back-scattered, both particles must flip their helicity. This can be seen by considering j_z of the incident photon. If the helicity does not flip, then $\Delta j_z^\gamma = \pm 2$. To conserve angular momentum, the electron would

need 2 units of spin to compensate, which it does not have ($\Delta j_z^e = \pm 1$ or 0). A similar argument shows that if the electron were to remain in the same helicity state ($\Delta j_z^e = \pm 1$), then the photon would be unable to compensate for it. The only angular momentum conserving process occurs when $\Delta j_z^\gamma = \Delta j_z^e = 0$, that is, they both flip their helicity.⁴

The last step of the derivation associates each channel with an angular momentum state. There are four angular momentum states that the electron and photon can be in. They are the $j_z = \pm 3/2$ states, where the spins are parallel (Fig. 2.10(a)), and the $j_z = \pm 1/2$ states, where the spins are anti-parallel (Fig. 2.10(b)). In Fig. 2.11,



Figure 2.10: Compton scattering angular momentum diagrams for (a) $j_z = 3/2$ (parallel spins) and (b) $j_z = 1/2$ (anti-parallel spins) states.

this information is overlaid on the Feynman diagrams of Fig. 2.8. The numbers in parenthesis are the values of j_z in each leg in the diagram. In s -channel processes, j_z for the intermediate electron is the sum of $j_z^e(\text{initial})$ and $j_z^\gamma(\text{initial})$, while in the u -channel process, it is the difference between $j_z^e(\text{initial})$ and $j_z^\gamma(\text{final})$.

Both the s -channel, $j_z = 3/2$ configuration (Fig. 2.11(a)), and the u -channel, $j_z = 1/2$ configuration (Fig. 2.11(d)), proceed through the exchange of a spin 3/2 electron and are not allowed. Combining this result with that of the comparison between the u and s propagators, shows that the cross section for back-scattered electrons in the u -channel, with $j_z = 3/2$ (Fig. 2.11(b)), will be larger than that of electrons in the s -channel, with $j_z = 1/2$ (Fig. 2.11(c)).

⁴One should not be worried about this process not conserving helicity. Helicity is only conserved at high energies. That is, when the energy involved is much larger than the particle mass so that the mass can safely be neglected. In eqs. 2.4 and 2.6, it is shown that the total cm energy squared, s , is not much larger than the square of the electron mass.

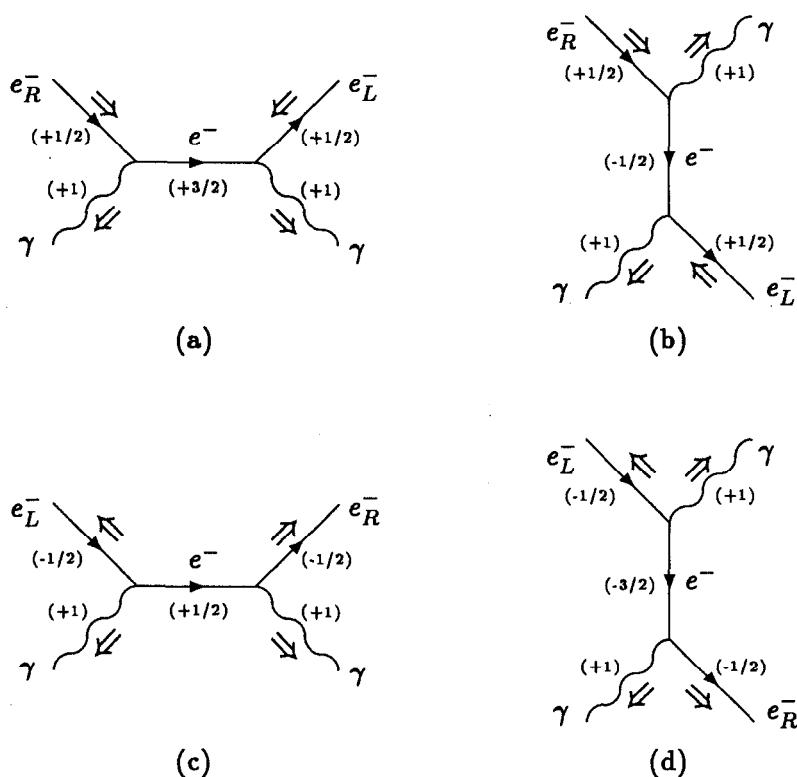


Figure 2.11: Angular momentum conservation in Compton back-scattering for the (a) s -channel, $j_z = 3/2$, (b) u -channel, $j_z = 3/2$, (c) s -channel, $j_z = 1/2$ and (d) u -channel, $j_z = 1/2$.

2.2.1.2 Kinematics of Compton Scattering

In the specific case of the Compton polarimeter, 2.33 eV photons collide with the 45.7 GeV electron beam at an angle of incidence of 10 mrad. Because of the large mismatch in energy, the velocity of the cm, β_{cm} , is larger than the velocity of the electrons in the cm, $\beta_e = p_{cm}/E_{cm}$. Therefore, *all* the scattered electrons will continue to propagate along the direction of the incident electrons. The relevant kinematic variables of the interaction, in the lab frame, are shown in Fig. 2.12. The largest angle they can scatter in the lab is given by

$$(\tan \theta_e)_{max} = \frac{p_{cm}}{\gamma_{cm} E_{cm}} \frac{1}{\sqrt{(\beta_{cm})^2 - \frac{(p_{cm})^2}{(E_{cm})^2}}}, \quad (2.7)$$

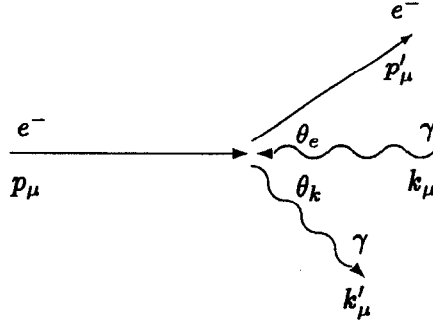


Figure 2.12: Compton interaction in the lab frame.

where β_{cm} is the velocity of the cm, while E_{cm} and p_{cm} refer to the electron in the cm, as defined in eq. 2.3. In the limit of $E \gg m_e \gg k$, substitution of the beam parameters into this equation gives $(\theta_e)_{max} = 9.3 \mu\text{rad}$. Therefore, all the scattered electrons will remain parallel to the beam direction and $\cos(\theta_e + \theta_k) \approx \cos \theta_k$.

Using the variables defined in Fig. 2.12, the final state variables can be calculated as a function of the initial state variables. In terms of the initial variables, s was found in eq. 2.6 to be

$$s = (E + k)^2 - (\vec{p} + \vec{k})^2 \approx m_e^2 + 4Ek. \quad (2.8)$$

After the interaction, s is given by

$$s = (E' + k')^2 - (\vec{p}' + \vec{k}')^2 = m_e^2 + 4E'k' - 2p'k' \cos \theta_k. \quad (2.9)$$

First, consider the special case of back-scattered electrons in the cm frame. This corresponds to $\theta_k = 0$. Both the photon and electron are collinear and propagate along the direction of the initial electron. The electron has the smallest energy allowed kinematically (E'_{min}) and the photon is scattered with its largest energy (k'_{max}). Eqs. 2.8 and 2.9 can be solved for the ratio:

$$\alpha \equiv \frac{k'_{max}}{E'_{min}} = \frac{4kE}{m_e^2}. \quad (2.10)$$

From the conservation of energy, $E \approx E' + k'$, E'_{min} and k'_{max} are found to be

$$E'_{min} = E \frac{1}{1 + \alpha} = Ey, \quad (2.11)$$

$$k'_{max} = E \frac{\alpha}{1 + \alpha} = E(1 - y), \quad (2.12)$$

where y is defined as

$$y \equiv \frac{1}{1 + \alpha} = \frac{1}{1 + \frac{4kE}{m_e^2}}. \quad (2.13)$$

The variable y represents the largest kinematically allowed fractional energy loss the electron can undergo.

In the general case when the two final particles are not colinear, eqs. 2.8 and 2.9 can be set equal to each other and written as

$$m_e^2 + 4kE = m_e^2 + 2k'E' - 2k'p' \cos \theta_k. \quad (2.14)$$

For small θ_k , as will be the case when the electron is back-scattered,

$$k' = Ey \frac{1}{1 + y \left(\frac{E\theta_k}{m_e}\right)^2} \quad (2.15)$$

$$= Eyx \quad (2.16)$$

$$= k'_{max} x \quad (2.17)$$

and

$$E' = E - k' \quad (2.18)$$

$$= E(1 - xy), \quad (2.19)$$

where x is defined as

$$x \equiv \frac{1}{1 + y \left(\frac{E\theta_k}{m_e}\right)^2}. \quad (2.20)$$

The angular dependence of the photon's fractional energy loss is contained in x .

To develop sensitivity to these variables, substitute the relevant beam parameters at the SLC. For a 45.7 GeV electron and 2.33 eV photon, $y = 0.38$ which gives $E'_{min} = 17.4$ GeV and $k'_{max} = 28.4$ GeV. Photons can scatter at all angles, although, as θ_k increases, their energy drastically decreases relative to their maximum. Photons scattered at 95 μ rad are down to 1 GeV, while at 3 mrad, they have an energy of only 1 MeV.

The longitudinal electron polarization P_- and the photon polarization P_γ are related to the polarized Compton differential cross section, $d\sigma_p/dx$, through the expression [21]:

$$\frac{d\sigma_p}{dx} = \frac{d\sigma_u}{dx} [1 - P_\gamma P_- A(x)], \quad (2.21)$$

where the unpolarized differential cross section $d\sigma_u/dx$ is given by

$$\frac{d\sigma_u}{dx} = 2\pi r_e^2 y \left\{ 1 + \frac{x^2(1-y)^2}{1-x(1-y)} + \left[\frac{1-x(1+y)}{1-x(1-y)} \right]^2 \right\}, \quad (2.22)$$

the asymmetry function $A(x)$ is given by

$$A(x) = 2\pi r_e^2 y [1 - x(1+y)] \left\{ 1 - \frac{1}{[1-x(1-y)]^2} \right\} \left(\frac{d\sigma_u}{dx} \right)^{-1} \quad (2.23)$$

and r_e is the classical electron radius. Note, for back-scattered electrons, $A(x=1)$ is greater than zero and eq. 2.21 displays the correct helicity dependence discussed in section 2.2.1.1, that is, parallel spin states have a larger differential cross section than anti-parallel spin states.

2.2.1.3 Measuring the Electron Longitudinal Polarization (Overview)

The Compton polarimeter has two major components: a polarized light source and an electron spectrometer. The polarimeter measures the electron beam polarization continuously throughout the SLD run in intervals of 20,000 SLC cycles (approximately three minutes). For each polarimeter run, the value of P_- is determined.

Fig. 2.13 gives an overview of how the Compton polarimeter fits into the SLC/SLD configuration, while Fig. 2.14 is a simple schematic of the detector, highlighting its essential components. The electrons that did not interact at the SLC e^+e^- IP are transported 33 m along a straight path, in order to preserve their polarization, to the $e^-\gamma$ (Compton) IP, CIP. There, they collide with a circularly polarized laser beam (see section 2.2.1.4) [22]. The crossing angle between the incident electrons and photons is 10 mrad (this has a negligible affect on the kinematic expressions derived in section 2.2.1.2). The scattered electrons range in energy from 17.4 GeV to

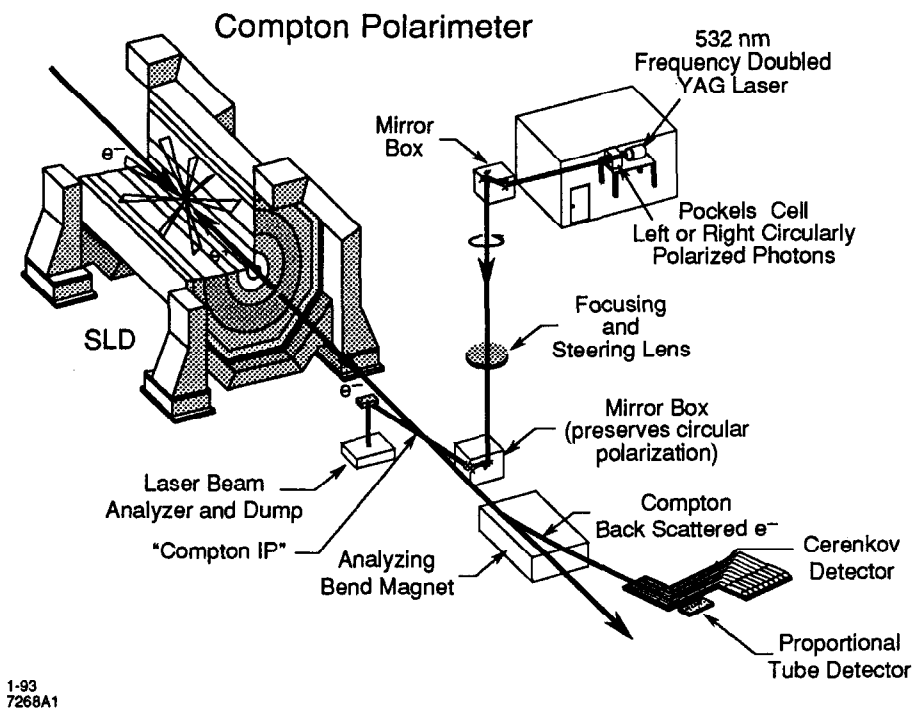


Figure 2.13: Overview of the SLD and the Compton polarimeter.

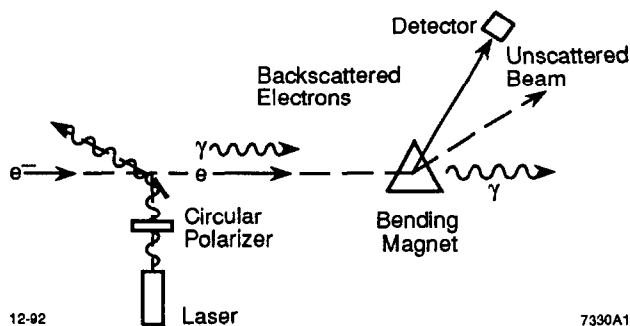


Figure 2.14: Schematic of the Compton polarimeter.

45.7 GeV. Because they are scattered at angles on the order of the angular dispersion of the beam (which is approximately $11 \mu\text{rad}$), they remain colinear to the incident electron beam. The electron bunch then passes through two bend magnets that give the electrons a combined transverse momentum kick of $833 \text{ MeV}/c$, dispersing them in the horizontal plane. The deflected electrons pass through a thin stainless steel

window, leaving the SLC vacuum. They are detected by a pair of multichannel detectors, a 9-channel Cherenkov detector and a 16-channel proportional tube detector.⁵ The detectors are located 3.57 m and 3.87 m past the bend center of the magnets, respectively (see Fig. 2.15). The angle of deflection and thus the distance from the undeflected beamline, t , are related to the energy through eq. 2.2. By a transformation of variables, eq. 2.21 can be expressed as

$$\frac{d\sigma_p}{dt} = \frac{d\sigma_u}{dt} [1 - P_\gamma P_- A(t)]. \quad (2.24)$$

The measurement of P_- is simplified by measuring the Compton asymmetry $A^c(t)$, rather than the differential cross section. $A^c(t)$ is defined as

$$\begin{aligned} A^c(t) &\equiv \\ &\frac{\sigma(P_\gamma \text{ parallel to } P_-, j_z = \pm 3/2; t) - \sigma(P_\gamma \text{ anti-parallel to } P_-, j_z = \mp 1/2; t)}{\sigma(P_\gamma \text{ parallel to } P_-, j_z = \pm 3/2; t) + \sigma(P_\gamma \text{ anti-parallel to } P_-, j_z = \mp 1/2; t)} \\ &= P_\gamma P_- A(t), \end{aligned} \quad (2.25)$$

where σ is a short-hand notation referring to the differential cross section evaluated at t . $A^c(t)$ is measured twice, once for each electron spin state. For a given distance t , by measuring $A^c(t)$ and P_γ and calculating $A(t)$, the electron polarization can be deduced from eq. 2.25. The sign of the polarization is determined by measuring the absolute sign of $A^c(t)$. For electrons that are back-scattered in the cm frame, $A^c(t)$ is positive.

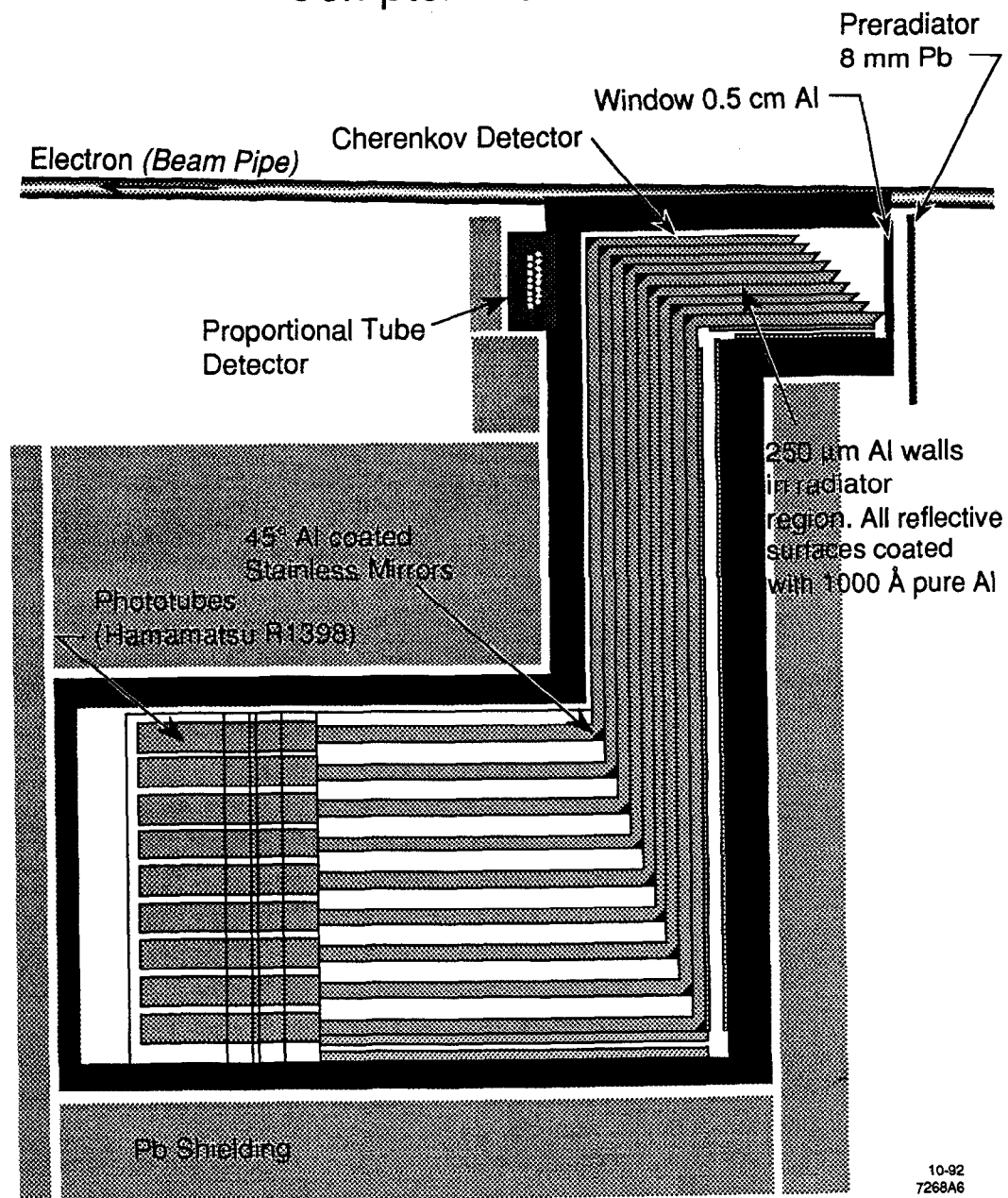
For a set P_- , the number of scattered electrons seen in the i^{th} channel of the multichannel detector is given by

$$N_i^\pm = N_i^0 + \mathcal{L}_c^\pm \int \frac{d\sigma_u}{dt} [1 \pm |P_\gamma P_-| A(t)] r_i(t) dt, \quad (2.26)$$

where: $+/-$ refers to the photon helicities that are parallel/anti-parallel to those of the electron; N_i^0 is the background reading of the channel; \mathcal{L}_c^\pm is the luminosity at the CIP; $r_i(t)$ is the response function of the channel; and the integral is over all t . Ideally, $r_i(t)$ is a step function, equal to 1 across the width of the channel and

⁵Because of large amounts of background noise detected by the proportional tubes, that detector was not used in measuring P_- .

Compton Detectors



10-92
7268A6

Figure 2.15: Compton electron detectors.

zero elsewhere. In practice, material in front of the detector and in between the channels causes $r_i(t)$ to deviate from being a perfect step function. The experimental asymmetry A_i^c measured in the i^{th} channel is

$$A_i^c \equiv \frac{N_i^+ - N_i^-}{N_i^+ + N_i^- - 2N_i^0}. \quad (2.27)$$

Assuming $\mathcal{L}_c^+ = \mathcal{L}_c^-$, eq. 2.27 reduces to

$$\begin{aligned} A_i^c &= P_\gamma P_- \frac{\int \frac{d\sigma_u}{dt} A(t) r_i(t) dt}{\int \frac{d\sigma_u}{dt} r_i(t) dt} \\ &= P_\gamma P_- a_i. \end{aligned} \quad (2.28)$$

The value of the asymmetry function $A(t)$ averaged over the i^{th} channel, weighted by the unpolarized cross section and the channel response function, is called the analyzing power of the i^{th} channel, a_i , which is defined as

$$a_i \equiv \frac{\int \frac{d\sigma_u}{dt} A(t) r_i(t) dt}{\int \frac{d\sigma_u}{dt} r_i(t) dt}. \quad (2.29)$$

Solving eq. 2.28 for the electron polarization gives a measurement of P_- for each detector channel:

$$P_- = \frac{A_i^c}{P_\gamma a_i}. \quad (2.30)$$

In the more general case, \mathcal{L}_c^+ and \mathcal{L}_c^- are unequal. Defining the Compton luminosity asymmetry $A_{\mathcal{L}}^c$ as

$$A_{\mathcal{L}}^c \equiv \frac{\mathcal{L}_c^+ - \mathcal{L}_c^-}{\mathcal{L}_c^+ + \mathcal{L}_c^-}, \quad (2.31)$$

leads to a generalization of eq. 2.28:

$$A_i^c = \frac{A_{\mathcal{L}}^c + P_\gamma P_- a_i}{1 + A_{\mathcal{L}}^c P_\gamma P_- a_i}. \quad (2.32)$$

Solving eq. 2.32 for the electron polarization gives

$$P_- = \frac{A_{\mathcal{L}}^c - A_i^c}{P_\gamma a_i (A_i^c A_{\mathcal{L}}^c - 1)}. \quad (2.33)$$

No detectable luminosity asymmetry was observed, so eq. 2.30 will be used. This point will be addressed in section 2.2.1.6.

2.2.1.4 Compton Polarized Light Source (CLS)

The photons that scatter off the electrons are generated by a frequency doubled Nd:YAG laser. The laser produces a 7 ns, 50 mJ pulse at 532 nm. The laser is pulsed once every 11 beam crossings. The ten intermediate crossings are used to measure the beam background. The light passes through a linear polarizer followed by a $\lambda/4$ Pockels cell, whose voltage is randomly switched between positive and negative voltages, producing RH- and LH-circularly polarized light. Directly after the Pockels cell, the polarization of the laser light is measured. The RH polarization is measured to be $(99.7 \pm 0.1)\%$, while the LH polarization is measured to be $(99.2 \pm 0.1)\%$.

The photons are transported down to the SLC beampipe, 40 m away, through an evacuated transport line. The transport line contains a series of four phase-compensating pairs of mirrors, a focusing lens and four vacuum windows.

The RMS width of the photon beam is $750 \mu\text{m}$ (which is larger than the $350 \mu\text{m}$ of the electron beam). The timing of the laser and its direction, relative to the electron beam, can be varied. They are continuously monitored and optimized so that the signal in the electron detector is maximized.

The photon polarization is measured directly at the CIP [23] by removing the section of the SLC beampipe surrounding the CIP. It is replaced by a rotating linear polarizer followed by either a joule-meter or a photodiode to measure the intensity of the transmitted light. Because of phase shifts caused by elements in the transport line, the light at the CIP is elliptically polarized. The polarizer is rotated in order to find the minimum and maximum intensities reaching the joule-meter. The minimum (maximum) intensity is a measure of the semi-minor (semi-major) axis of the ellipse.

The net circular polarization is given as⁶:

$$P_\gamma = 2 \frac{\sqrt{I_{max} I_{min}}}{I_{max} + I_{min}}, \quad (2.37)$$

where I_{min} (I_{max}) is the intensity measured by the joule-meter when the polarizer is aligned with the semi-minor (semi-major) axis of the ellipse. By rotating the polarizer 180° relative to the initial measurement, two measurements are made for both I_{max} and I_{min} . The complete set of measurements was carried out twice, once at the beginning of the run and then at the end. The first time, the intensity was measured with a joule-meter and the second time, it was measured with a photodiode.

The photon polarization is measured for both RH- and LH- photon helicities. P_γ is the average of the two measurements. The systematic error on P_γ is taken to be the difference between P_γ and the separate helicity measurements ($\Delta P_\gamma / P_\gamma = 1\%$). The values of P_γ measured before and after the run were the same.

There are additional uncertainties that result from fluctuations in the system that arise from the degradation and misalignment of the many optical components over time. The laser polarization is monitored continuously throughout the run both on the laser bench (directly after the Pockels cell) and at the analysis box (located after the CIP). On the laser bench, the light passing through the Pockels cell is partially reflected towards a prism. The prism splits the elliptically polarized light along its semi-major and semi-minor axes. The prism is aligned with the elliptical axes of the light in order to maximize I_{max} and minimize I_{min} . Two joule-meters simultaneously measure I_{max} and I_{min} for each pulse. The photons arriving at the analysis box

⁶Elliptically polarized light can be expressed as a superposition of RH and LH polarized light. The electromagnetic waves describing RH and LH light propagating along the z axis can be written as

$$\vec{E}_R = E_R^0 [\hat{i} \cos(kz - \omega t) + \hat{j} \sin(kz - \omega t)], \quad (2.34)$$

$$\vec{E}_L = E_L^0 [\hat{i} \cos(kz - \omega t) - \hat{j} \sin(kz - \omega t)], \quad (2.35)$$

with $\vec{E}_{elliptic} = \vec{E}_R + \vec{E}_L$. The intensity of a beam is $I = 1/2 |\vec{E}|^2$. Thus, the polarization is simply

$$P_\gamma = \frac{I_R - I_L}{I_R + I_L} = \frac{E_R^2 - E_L^2}{E_R^2 + E_L^2} = 2 \frac{\sqrt{I_{max} I_{min}}}{I_{max} + I_{min}}, \quad (2.36)$$

where $I_{min} = 1/2(E_R - E_L)^2$ and $I_{max} = 1/2(E_R + E_L)^2$.

undergo an additional uncompensated phase shift relative to their state at the CIP. In addition, the prism in the analysis box is not optimally aligned with the elliptical axes of the photon polarization. Therefore, only the laser bench polarization measurements are used to track the time dependent shifts of the CLS. These fluctuations add an additional 1% to the relative systematic error.

The overall absolute systematic error is conservatively estimated to be 2% and the photon polarization is measured to be $(93 \pm 2)\%$.

2.2.1.5 Cherenkov Detector

The nine-channel threshold Cherenkov detector [22, 24] is located 355.8 cm downstream from the bendpoint of the analyzing magnets. Each of the channels projects back to the bendpoint and covers a constant opening angle. The dimensions of the fifth channel are 1 cm \times 1.5 cm \times 20 cm. Mirrored aluminum walls, 250 μ m wide, separate the channels. The channels are filled with a non-scintillating gas, β -butylene, held at a pressure of 1.0 atm. The threshold for producing Cherenkov photons in the gas is approximately 10 MeV. It is estimated that the photon collection efficiency for 253.7 nm photons is over 50%. The photons are detected at the end of the channel by a Hamamatsu R1398 photomultiplier tube.

A retractable 8 mm piece of lead (1.4 radiation lengths) is placed between the detector and the incident electrons. The lead preradiator serves two purposes: first, it reduces the noise caused by beam-related photons and second, it increases the signal from the incident electron's shower by a factor of approximately four. One side effect of the lead is that the shower can spread to neighboring channels.

In eq. 2.30, it was shown that the measured asymmetry, A_i^c , was divided, in part, by the analyzing power, a_i , in order to deduce P_- . Each channel makes a separate measurement of P_- . However, it was not possible to extract the channel-to-channel correlations since only polarimeter run *time averaged* values (and not the *pulse-by-pulse* values) of N_i^\pm and N_i^0 are written to tape. Since A_7^c has the largest asymmetry, it was used to calculate P_- , while the other channels served as a consistency check. In the beginning of the run, channel 7 was not active, so channel 6 was used.⁷

⁷There were 742 Z^0 events that were detected using channel 6, while 9482 events relied on

The analyzing powers are completely determined by the theoretical functions, $d\sigma_u/dt$ and $A(t)$, the simulated detector response function and knowledge of the distance of the channel, t , from the undeflected beamline. The measured asymmetries are sensitive to detector linearity and the effects of electronic noise.

Spectrometer Calibration The first step in calculating the analyzing powers is to develop a simulation of the detector and the interacting particles. An EGS Monte Carlo was used to simulate the electromagnetic interactions and model the response function for each detector channel. The simulation took into account the beam parameters and detector components.

In addition to the response function, knowledge of the magnet bend strength and the location of the detector are needed. The bend strength provides information on the deflection of the electrons from the beamline, according to their energy. The detector location, together with the bend strength give the expected value of $A(t)$ in each channel.

The location of the detector is determined by measuring two "landmarks" of the asymmetry function $A(t)$. The landmarks correspond to two final state electron energies. The first is the kinematic endpoint to which the electrons with the lowest final state energy (17.36 GeV) are scattered. Beyond that point, only beam backgrounds are measured. The second point is located where $A(t)$ is zero, corresponding to scattered electrons with a final state energy of 25.16 GeV. Here, the measured asymmetry is insensitive to electron beam polarization fluctuations. Of the nine detector channels, the first six are completely contained within the kinematically allowed region of $A(t)$, while the seventh channel straddles the kinematic endpoint. The eighth and ninth only measure beam related backgrounds.

To calibrate the position of the detector relative to the beamline, a scan of the kinematic endpoint is carried out using the sixth channel. The detector is moved away from its nominal position and the response of channel 6 is measured. As it passes through the endpoint, the response begins to drop off. This point can be measured to a precision of 0.03 cm.

channel 7.

Between channels 2 and 3, $A(t)$ is approximately linear. The location of the zero-asymmetry point, is calculated using the expression:

$$A_0 = \left| \frac{A_2}{A_3 - A_2} \right|, \quad (2.38)$$

where A_2 (A_3) is the measured asymmetry in the second (third) channel and A_0 is the location of the zero-asymmetry point expressed as the fractional channel width deviation from the center of channel 2. A_0 was measured to be 0.22 ± 0.1 . An additional 0.01 is added to this to account for the nonlinearity of $A(t)$ and $d\sigma_u/dx$, and the effects of showering, as indicated by the EGS simulation. Thus, the zero-asymmetry point has been measured to be 0.23 cm away from the center of channel 2.

As a consistency check, the momentum kick supplied by the bend magnet can be measured and compared to its nominal value (measured independently by the SLC). Given the dimensions of the detector, the distance between these two points is 5.26 ± 0.03 cm. Therefore, the transverse momentum kick the electrons receive at the bend magnet is measured by the Cherenkov detector to be: (827.9 ± 5.3) MeV/c. The nominal value of the bend magnet is 833 MeV/c, giving a difference of 0.6%.

The ± 0.03 cm uncertainty in the determination of the endpoint corresponds to a relative error of $\pm 0.49\%$ ($\pm 0.18\%$) in the analyzing power of channel 6(7). The weighted relative uncertainty in the analyzing powers is 0.2%.

In Fig. 2.16, the calculated analyzing powers for each channel are overlaid on the asymmetry function, $A(t)$.

Stability of the kinematic endpoint is monitored by comparing the ratio of the background subtracted signals in channel 7 to those of channel 2. Channel 2 is one of the inner channels and is less sensitive to movement of the endpoint. The deviation in the ratio of signals measured over the course of the run constrains the endpoint to be within 0.025 cm of the position defined in the endpoint scan. This uncertainty is approximately the same size as the uncertainty of the endpoint scan.

Combining these uncertainties in determining the position of the detector corresponds to relative uncertainty in the analyzing powers of 0.4%.

The average relative uncertainty in the measured asymmetries due to the nonlinearity in the response of the photomultiplier tube is 1.5%.

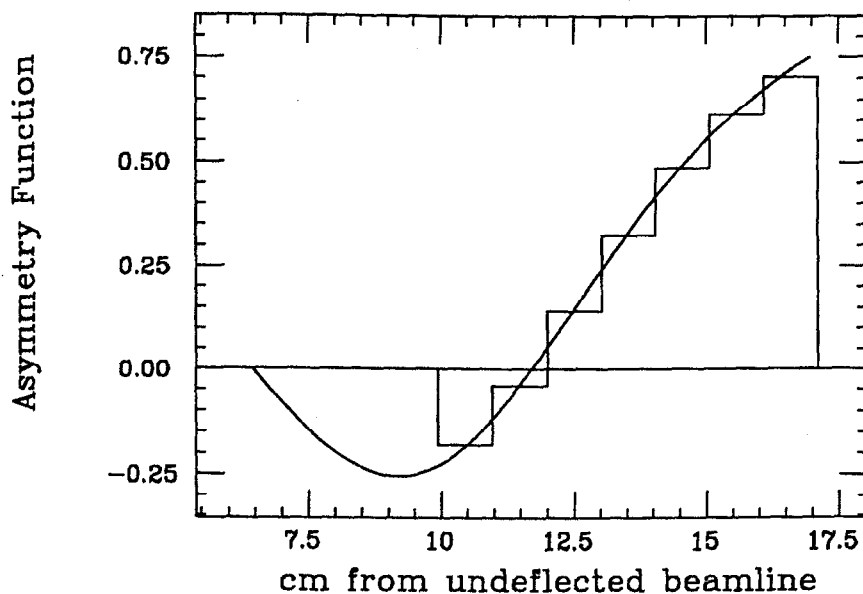


Figure 2.16: Compton analyzing powers [24].

Two types of electronic cross-talk are observed in the channel readouts. The first is a result of pickup of the laser switch. The second is due to cross-talk between the channels themselves. They contribute 0.3% and 0.1%, respectively, to the relative error of the measured asymmetries.

The discrepancy between the run averaged polarization measured for channels 6 and 7, leads to a relative error of 0.9% in the polarization. The reason for this discrepancy has not been determined and it will be treated as part of the overall systematic error.

2.2.1.6 Compton Polarimeter Results

Quality cuts were placed on the results of each polarimeter run. Runs were discarded for the following reasons: the total signal and background subtracted signal were too low, the number of events per laser-electron orientation in a run was less than 5 and the absolute error on the measured electron polarization was greater than 5%. Table 2.2 lists the average systematic errors on the quantities measured by the

Compton polarimeter per polarimeter run. In Fig. 2.17, the 1992 SLD run averaged values of the measured asymmetries, $\langle A_i^c \rangle$, are overlaid on the theoretically expected asymmetry function, $A(t)$, multiplied by the measured laser polarization of 93% and electron polarization of 22.4%. The errors on $\langle A_i^c \rangle$ are negligible. If \mathcal{L}_c^+ did not equal \mathcal{L}_c^- , as was assumed, then the measured values of $\langle A_i^c \rangle$ would be displaced relative to the theoretically derived quantity $P_- P_\gamma A(t)$ (see eq. 2.33). This effect is not observed.

Source of Error	$\delta P_- / P_- (\%)$
Laser polarization	2.0
Position calibration	0.4
Linearity	1.5
Electronic cross-talk	0.4
Channel consistency	0.9
Total	2.7

Table 2.2: Relative systematic errors of the Compton polarimeter [23, 24].

2.3 SLAC Large Detector

The decay products of the Z^0 are measured in the SLAC Large Detector (SLD), a 4π detector optimized for precision measurements of these particles [25]. The SLD is composed of several subsystems (see Fig. 2.18), each designed to measure a specific part of the decay. A vertex detector (VXD) and drift chamber placed in a 0.6 T axial magnetic field provide high precision charged particle tracking and momentum measurements. Charged particle identification is made with the Cherenkov ring imaging detector (CRID). Three different sampling calorimeters⁸ measure the energy of the particles. They are the silicon-tungsten calorimeter (LUM), the lead-liquid argon calorimeter (LAC) and the iron-streamer tube calorimeter (also called the warm iron

⁸Calorimeters are devices that measure a particle's energy. "Sampling" calorimeters are devices that have "passive" layers specifically designed to absorb incident particles and their resulting showers, alternated with "active" layers designed to periodically measure the development of those showers.

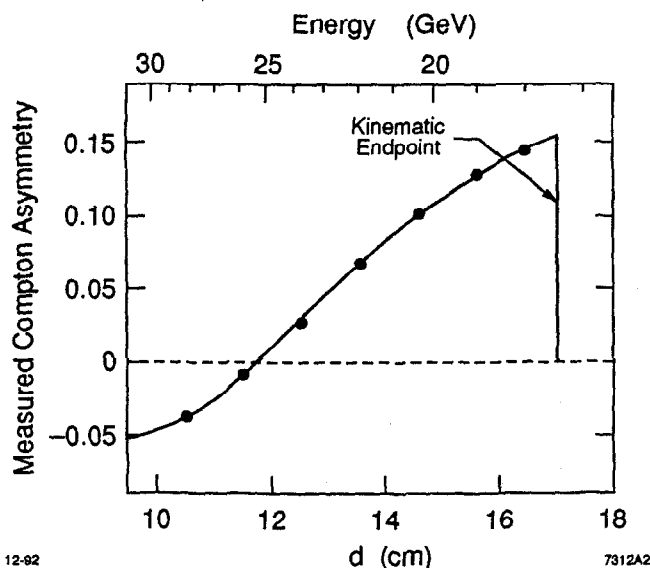


Figure 2.17: Measured Compton asymmetry in the Cherenkov detector [24]. The lower horizontal axis is the distance from the undeflected beamline (what was defined as the variable t in section 2.2.1.3). The upper horizontal axis is the energy of the scattered electrons.

calorimeter or WIC). The LUM measures the luminosity of the accelerator. The LAC is sensitive to electromagnetic and hadronic showers. The WIC is used for additional hadronic calorimetry, muon tracking and flux return of the magnetic field.

Even though the detector is cylindrically symmetric, because the experimental observables are readily expressed in spherical coordinates, the detector is segmented in spherical coordinates. The polar angle θ is measured relative to the beam axis. The azimuthal angle ϕ describes rotations around the beam axis. The longitudinal or radial direction describes distances from the IP. In the usual right-handed cartesian coordinate system, z is defined to be along the beam axis, $\theta = 0$, x coincides with $\phi = 0$ and y is perpendicular to x and z .

The drift chamber, CRID, LAC and WIC are made up of barrel and endcap components which cover the central ($|\cos \theta| \lesssim 0.82$) and forward/backward ($|\cos \theta| \gtrsim 0.82$) regions of the volume around the IP.

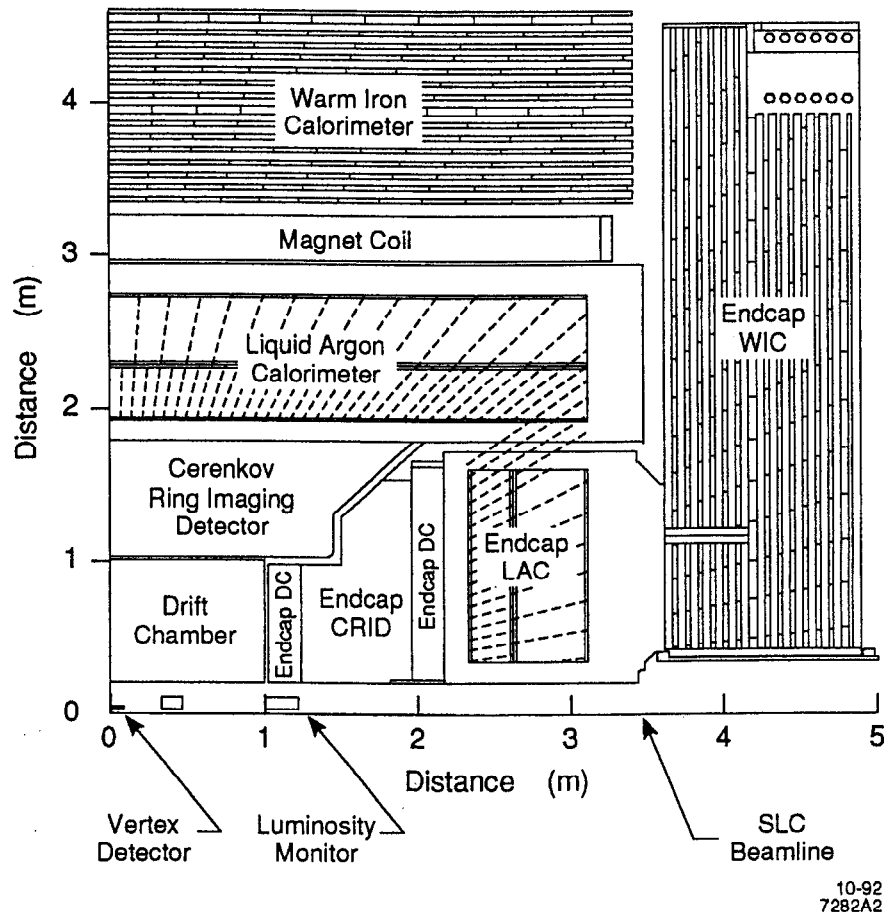


Figure 2.18: Quadrant view of the SLD. Dashed lines indicate the boundaries of the projective tower geometry.

2.3.1 Vertex Detector

Immediately surrounding the IP is the VXD [25, 26]. The VXD uses silicon pixels to increase the tracking resolution of the drift chamber by making high precision measurements of particle tracks around the IP. This added precision enables one to distinguish between secondary and primary vertices in the decays of heavy quarks and taus. Typically, the vertices are separated by 2 to 4 mm.

Making use of charge-coupled devices (CCD), the VXD is able to measure 3D information on the tracks. A CCD is semiconductor device consisting of a matrix of pixels, where each pixel has a surface area of a few μm^2 [27]. Each pixel is a potential

well, storing the ionization information of the particle which traversed it. Charge coupling refers to the ability to transfer that information to the neighboring pixel by manipulating the voltage of the potential well. To read out a CCD, all the rows are shifted by one so that row i becomes row $i - 1$. The first row is transferred to a shift register which then reads out each column. The process is repeated until all the rows have been processed. This takes approximately 50 msec per CCD.

The VXD contains 480 CCDs arranged in groups of eight on ladders (see Table 2.3). The ladders are arranged in four concentric cylinders of radii 29.5, 33.5, 37.5 and 41.5 mm around the beampipe. The cylinders are aligned such that any particle emitted at an angle $|\cos \theta| \leq 0.77$ will pass through at least two cylinders.

CCD Parameters	
Pixel cell size	$22 \mu\text{m} \times 22 \mu\text{m}$
Area of CCD	385 pixels \times 578 pixels ($8.5 \times 12.7 \text{ mm}^2$)
Number of pixels/CCD	222,530
Track cluster size	80% of charge deposited in 1 to 2 pixels

VXD Parameters	
Active area of ladder	$8.5 \times 100 \text{ mm}^2$
Number of ladders	60
Total number of pixels	107 Mpixels
Readout time	152 ms (19 beam crossings)
Spatial resolution (xy)	$10 \mu\text{m}$
Spatial resolution (rz)	$8 \mu\text{m}$

Table 2.3: Vertex detector parameters [25].

During event reconstruction, drift chamber tracks are extrapolated back through the VXD and are linked to hits in the vertex detector. The efficiency for linking tracks is approximately 96%.

2.3.2 Drift Chamber

Most of the charged particle tracking is carried out by the drift chambers. There is a central drift chamber (CDC) covering the barrel region [25, 28] and four endcap

drift chambers (ECDC) covering the forward/backward regions. The large amount of beam backgrounds made it hard to extract useful data from the ECDCs.

The CDC is a cylindrical annulus, centered around the beampipe. It is 2 m long with an inner radius of 0.2 m and an outer radius of 1.0 m. The volume is filled with a CO₂-Ar-Isobutane gas.

The building blocks of the detector are cells that create electric fields (see Fig. 2.19). As the particles pass through the gas, they ionize the molecules. Applying voltages to the guard and field-shaping wires will cause the liberated electrons to drift towards a series of high resistance anode sense wires at a constant velocity of $9 \mu\text{m}/\text{ns}$. As they near the guard wire, they are accelerated by the field around it towards the sense wire. This increase in energy leads to secondary ionization of the gas, which in turn leads to an avalanche of $\sim 10^5$ electrons that are detected by the sense wire. There are

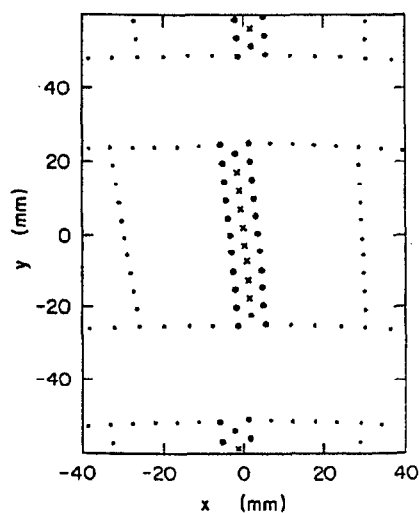


Figure 2.19: Central drift chamber cell [25]. Sense wires are shown as \times , guard wires as \bullet and field wires as \cdot .

eight sense wires per cell. The CDC is made up of 640 cells arranged in 10 concentric superlayers. The layers alternate between giving axial and stereo information. The stereo layers are angled at ± 41 mrad with respect to the beam axis:

The cells provide xy information by measuring the drift time to the wire ($\leq 3.3 \mu\text{sec}$). For a constant drift velocity, the drift distance is then calculated.

The spatial resolution (in xy) for each wire is approximately $100\mu\text{m}$. Each wire is read out at both ends. Therefore, by measuring the charge division on the wire, the z position is determined. The error in determining the z position is ± 4 cm.

Charge Division The charge division technique enables one to determine the location of the avalanche along the sense wire. The method requires a high resistance wire with amplifiers attached at each end. When an avalanche occurs at some point along the wire, it produces a current in the wire. Each amplifier integrates the current passing through it, thus measuring the charge. The measured charge in each amplifier is inversely proportional to the resistance along its path. For an avalanche occurring a distance x left of the center of a wire of length L , the relative charge measured by each amplifier is

$$\frac{Q_{Right}}{Q_{Left}} = \frac{\frac{1}{2}L - x}{\frac{1}{2}L + x}, \quad (2.39)$$

which can be solved for x to give

$$x = \frac{L}{2} \left(\frac{Q_{Left} - Q_{Right}}{Q_{Left} + Q_{Right}} \right). \quad (2.40)$$

2.3.3 Cherenkov Ring Imaging Detector

Charged particle identification is obtained from the Cherenkov ring imaging detector (CRID) [25, 29]. It is based on the principle that particles traveling faster than the speed of light in a medium will emit light at a constant angle, relative to the direction of motion. The angle of emission is related directly to the particle's velocity. Thus, measurement of the particle's momentum in the drift chamber, combined with a measurement of its velocity in the CRID, enables the identification of the mass of the particle.

As a particle passes through a dielectric medium, at velocities above the speed of light in that medium, c/n , where n is the index of refraction of the medium, it polarizes nearby atoms, which coherently emit photons at an angle, θ , relative to its path. The emission angle is determined by the particle velocity, βc , and the index of refraction of the medium. They are related through the equation:

$$\cos \theta = \frac{1}{\beta n}. \quad (2.41)$$

The effect only takes place when $\beta > 1/n$.

For a given medium, there is a velocity threshold, $\beta_t = 1/n$, below which no photons will be radiated coherently. When the particle's velocity passes that threshold ($\beta > \beta_t$), the opening angle increases. It saturates at $\theta_{max} = \cos^{-1}(1/n)$, when β equals 1. The opening angle at the saturation point, for a given gas, will be the same for all particle types. Particle identification takes place only in the region where the velocity is above threshold and below saturation. Since the saturation point is defined by n , use of media with different n varies the range of velocities that one is sensitive to.

The barrel CRID uses two media (see Table 2.4). Particles pass through both liquid and gas radiators. The liquid radiator is able to differentiate between low energy particles, while the gas radiator was chosen to be sensitive to the higher energy particles.

	Liquid	Gas
Radiator material	C_6F_{14}	70% C_5F_{12} and 30% N_2
Index of refraction (for $\lambda = 190.7$ nm)	1.277	1.001725
Thickness of radiator	1 cm	~ 45 cm
Cherenkov Angle (for $\beta = 1$)	672 mrad	59 mrad
Radius of Cherenkov ring (for $\beta = 1$)	17 cm	2.9 cm
Local angle resolution	~ 12 mrad	~ 4 mrad
Cumulative misalignment resolution	~ 10 mrad	~ 10 mrad
Number of photoelectrons (for $\beta = 1$)	$\sim (13 - 16)$	$\sim (7 - 9)$
Momentum threshold:		
e	~ 1 MeV/c	~ 9.5 MeV/c
π	0.23 GeV/c	2.6 GeV/c
K	0.80 GeV/c	9.1 GeV/c
p	1.5 GeV/c	17.3 GeV/c
Particle separation at 90° (@ 3σ level)	Both radiators	
e/π	0.2 – 6.2 GeV/c	
μ/π	$\left\{ \begin{array}{l} 0.2 - 1.1 \text{ GeV/c liquid} \\ 2.1 - 3.8 \text{ GeV/c gas} \end{array} \right.$	
π/K	0.23 – 23 GeV/c	
K/p	0.80 – 37 GeV/c	

Table 2.4: Barrel CRID parameters [25, 29].

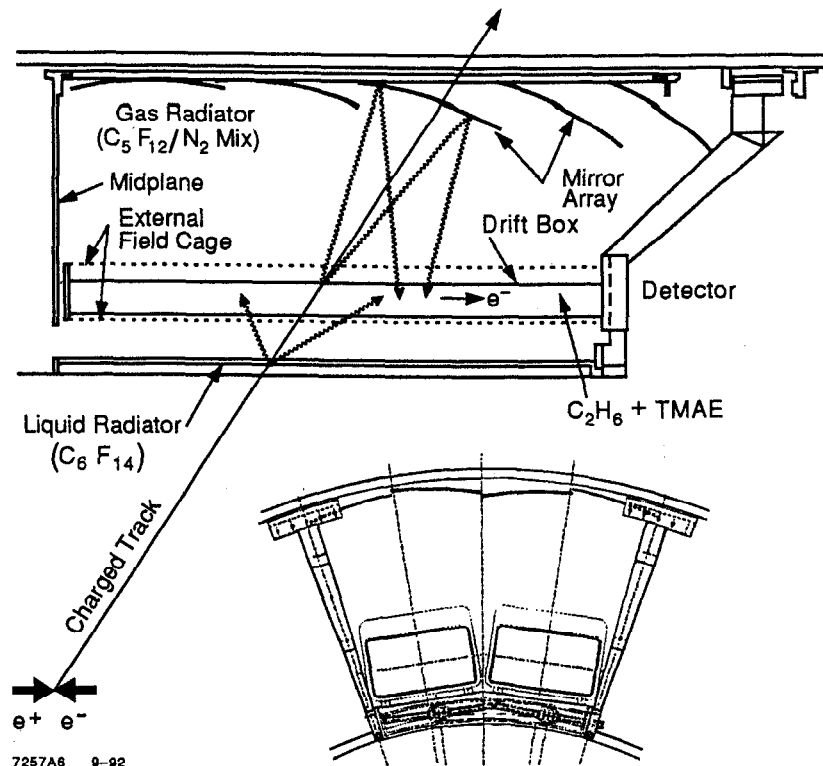


Figure 2.20: Schematic of the barrel CRID [29].

Photons created in both media are detected in a drift box (see Fig. 2.20). Photons produced in the liquid radiator simply propagate into the drift box, while the photons produced in the gas radiator are focused back to the drift box by a series of spherical mirrors (of focal length ~ 50 cm). The drift box (active area $126.8 \text{ cm} \times 30.7 \text{ cm} \times 5.6 \text{ cm}$) is filled with a gaseous mixture of C_2H_6 and 0.1% TMAE (Tetrakis Dimethyl Amino Ethylene). The photons pass through the quartz faces of the drift box and photoionize the TMAE. TMAE has a high quantum efficiency ($\sim 40\%$) in the range of 170 to 220 nm. An electric field (400 V/cm) enclosing the drift box causes the liberated electrons to drift at a constant velocity ($\sim 4.385 \text{ cm}/\mu\text{s}$) towards a series of anode sense wires. As in the case of the drift chamber, when the electrons near the sense wires, they are accelerated, causing an avalanche of electrons ($\sim 10^5$) to reach the anode. The coordinates (see Fig. 2.21) of the point of absorption of the photon are measured by the electron drift time (z),

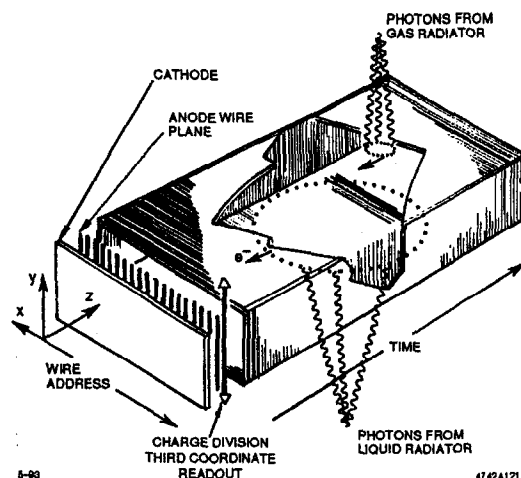


Figure 2.21: Schematic of the barrel CRID drift box [29].

wire address (x) and charge division along the high resistance anode wire (y) to a precision of approximately $1 \text{ mm} \times 1 \text{ mm} \times 2 \text{ mm}$, respectively. Each drift box contains 93 carbon anode wires, of diameter $7 \mu\text{m}$, spaced 3.175 mm apart.

Fig. 2.22 is a preliminary result of particle identification using liquid rings measured in hadronic Z^0 decays. Similar plots using gas rings have been made.

In the forward/backward regions, particle identification is made using the endcap CRIDs. They operate on the same principle as the barrel. In the endcaps, only the gas radiator was implemented. The gas used is C_4F_{10} . During the 1992 run, they were not operational.

2.3.4 Lead-Liquid Argon Calorimeter

The LAC is a parallel plate-liquid argon sampling calorimeter [25, 30]. It is used to measure the energy of the particles in a Z^0 decay. The detector is segmented into four radial layers to provide information on the shower development. The two innermost layers (called EM1 and EM2) are finely segmented and measure the energy of electromagnetic showers to high precision. The outer two layers (called HAD1 and HAD2) are more coarsely segmented and are designed to absorb hadronic showers. Together, EM1 and EM2 form the EM section while HAD1 and HAD2 form the HAD

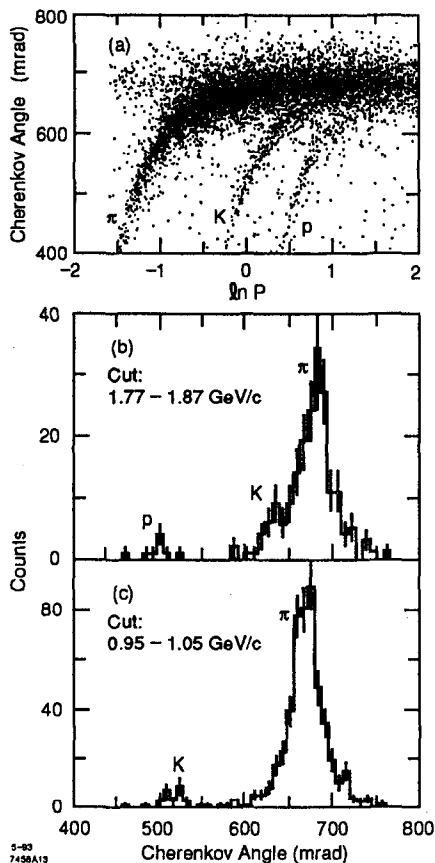


Figure 2.22: (a) Spectrum of measured Cherenkov angles (from liquid rings) in hadronic Z^0 decays. (b) and (c) show vertical slices of (a), demonstrating the ability to identify different particles [29].

section of the LAC.

The LAC is divided into three separate systems, one cylindrical barrel (covering $|\cos \theta| < 0.83$) and two endcap plugs (covering $0.82 < |\cos \theta| < 0.99$), which fit inside the barrel.

In each system, all four radial layers are immersed in a single volume of liquid argon. The cryogenics for each of the three components (barrel and endcaps) are controlled separately. Each calorimetry system is completely contained in a dewar and cooled by liquid nitrogen flowing through tubes mounted inside the dewar. The temperature is controlled by regulating the pressure in the nitrogen tubes.

Fundamentally, the LAC detects the amount of charge resulting from ionization

of the liquid argon by particles traversing it. That charge is directly proportional to the energy loss of the incident particle. The building blocks of the LAC are lead-liquid argon cells. Each cell is composed of a liquid argon ionization chamber, located between parallel lead electrodes, held apart by plastic spacers (Fig. 2.23). Lead has

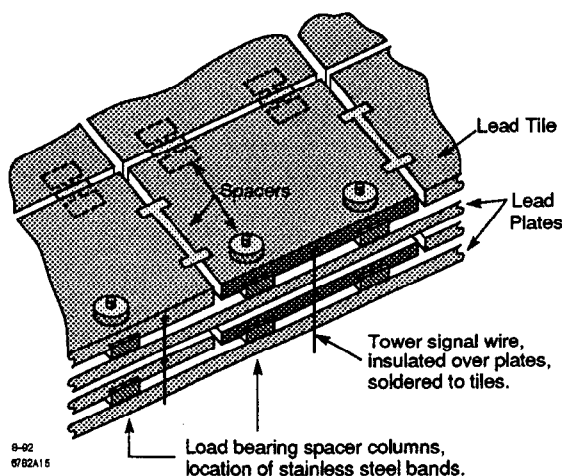


Figure 2.23: The structure of a LAC cell [30].

a two-fold use. It absorbs the high energy particles, creating showers of lower energy particles that in turn ionize the liquid argon. In addition, it is used as electrodes to detect the electrons liberated through the ionization process. One lead layer is a continuous plate held at ground. The other layer is composed of segmented tiles held at high voltage (2 kV). The lateral size of the tiles defines the area of the cell. The thickness of the lead and liquid argon defines how much energy will be deposited in each cell. Table 2.5 lists the thickness (in units of mm, radiation length⁹ X_0 and absorption length¹⁰ λ) of each layer in the EM and HAD sections. The sampling fraction¹¹ for the EM (HAD) section is 18.5% (7%).

⁹ X_0 is called the radiation length. The radiation length is defined as the average thickness of a medium over which a high energy electron will lose all but e^{-1} of its initial energy through radiation.

¹⁰The nuclear interaction length λ (also called the absorption length) sets the scale for the spatial development of a hadronic shower. It is defined as the mean free path between inelastic nuclear collisions.

¹¹The sampling fraction is the amount of energy a muon deposits in the sampled layers divided by the total energy deposited in all the layers, i.e. $dE(\text{sampled layer})/[dE(\text{sampled layer}) + dE(\text{absorber layer})]$.

Material	EM cell			HAD cell		
	mm	X_0	λ	mm	X_0	λ
Lead	2.00	0.357	0.0117	6.00	1.071	0.0351
Liquid argon	2.75	0.020	0.0033	2.75	0.020	0.0033
Lead	2.00	0.357	0.0117	6.00	1.071	0.0351
Liquid argon	2.75	0.020	0.0033	2.75	0.020	0.0033
Total per cell	9.50	0.754	0.0300	17.50	2.182	0.0768

Table 2.5: Thickness of the LAC unit cells [25].

Layer	Cells	mm	X_0	λ
EM1	8	76.0	6.03	0.24
EM2	20	190.0	15.08	0.60
EM (total)	28	266.0	21.11	0.84
HAD1	13	227.5	28.37	1.00
HAD2	13	227.5	28.37	1.00
HAD (total)	26	455.0	56.74	2.00
LAC (total)		721.0	77.85	2.84

Table 2.6: Readout structure of LAC layers [25].

Cells are connected together radially to create projective towers (see Table 2.6). The charge accumulated in all the cells of a tower is combined to produce a single readout. The amount of accumulated charge is digitized by an analog-to-digital converter (ADC), transforming the charge into ADC counts. To maintain a constant projective area for the incident particles, the area of the tiles varies as a function of the distance from the IP. Keeping a constant projective area throughout the detector results in towers having the same response, independent of their location. The area covered by the EM towers completely contains the lateral spread of an electromagnetic shower. The EM towers are segmented into 192 azimuthal bins of $\delta\phi = 33$ mrad. The polar angle segmentation varies from $\delta\theta = 36$ mrad, at $z = 0$ m, to $\delta\theta = 21$ mrad, at $z = 3.1$ m. The HAD towers are twice as large in θ and ϕ (see Table 2.7).

The endcaps are segmented similarly to the barrel, except at small polar angles, where the ϕ segmentation is decreased to maintain a constant area perpendicular to

Layer		Tile size (in mm)			
		at $z = 0$ m		at $z = 3.1$ m	
		$\delta\phi$	δz	$\delta\phi$	δz
EM1	Entrance tiles	60	68	60	123
	Exit tiles	62	70	62	125
EM2	Entrance tiles	63	70	63	125
	Exit tiles	69	77	69	143
HAD1	Entrance tiles	144	160	144	257
	Exit tiles	158	176	158	266
HAD2	Entrance tiles	159	177	159	268
	Exit tiles	172	192	172	276

Table 2.7: Geometry of LAC barrel tiles [25].

the shower.

There are 32,448 towers in the barrel and 8,640 towers in each of the endcaps. All 41,088 towers in the LAC are read out every beam crossing.

The EM section's $21 X_0$ contains 99% of the energy of a 45 GeV electron. The LAC's total thickness of 2.84λ contains approximately 85% of the energy in hadronic Z^0 decays. The WIC absorbs the remaining 15% of the energy.

Studying 45 GeV electrons, the resolution of the EM section is estimated to be $\sigma(E)/E = 15\%/\sqrt{E}$ (E is in GeV). The resolution of the HAD section is determined by comparing the momentum measurement in the drift chamber of isolated tracks with the LAC's energy response. Preliminary results show the resolution to be $\sigma(E)/E = 55\%/\sqrt{E}$ (E is in GeV).

Energy Scale The conversion of ADC counts to GeV involves several steps [31]. A muon deposits energy in the LAC through ionization. The liberated electrons in the liquid argon are accumulated and transformed into ADC counts.

Given the energy required to ionize an argon atom, 23.6 eV, the energy loss of a muon, when traversing liquid argon, is 2.11 MeV/cm. The number of liberated electrons per MeV deposited in the liquid argon is 42,373. The response of the ADC is such that 1 ADC count equals 8011 electrons. There are some inefficiencies in the method with which the electrons are counted. Accounting for those inefficiencies, it is found that an energy loss of 1 MeV in the liquid argon equals

2.64 ADC counts. The last step in calculating the total energy deposited in a LAC tower is to divide the energy loss in the liquid argon by the sampling fraction. For muons, the energy scale is defined by

$$\text{EM section: } 1 \text{ GeV} = 488 \text{ ADC counts,} \quad (2.42)$$

$$\text{HAD section: } 1 \text{ GeV} = 185 \text{ ADC counts.} \quad (2.43)$$

To account for the inefficiency of a capacitor used in reading out the accumulated charge, there is an additional factor of ~ 0.8 (it varies from tower to tower) that one needs to divide the ADC counts by.

Electromagnetic showers deposit more energy than muons in the lead, that is, they have a smaller sampling fraction. Therefore, the energy of electromagnetic showers measured in the muon energy scale is divided by a factor called the e/μ ratio that corrects the detector response to electromagnetic showers. Hadronic showers are even less efficient at depositing energy in the liquid argon. The appropriate correction factor there is called the π/μ ratio, which the energy of hadronic showers, measured in the muon energy scale, is divided by. Initial results have shown e/μ to be 0.69, while π/μ is 0.49. Because that analysis had not been completed when this analysis was done, the LAC measurements presented here will *all* be in the muon energy scale. On average, the LAC response to a Z^0 decaying hadronically (which is only $\sim 85\%$ of the *total* hadronic shower) is 35 GeV in the muon energy scale, while the response to e^+e^- final states is ~ 63 GeV.

2.3.5 Warm Iron Calorimeter

The outermost layer of the SLD is the WIC [25, 32]. The WIC is made up of alternating layers of streamer-tube sampling chambers and iron plates. Its use is three-fold. The first use is to absorb the remaining 15% of the hadronic showers in its four absorption lengths of material. In addition, it tracks muons that traverse the entire detector. Finally, the iron serves as a flux return for the 0.6 T solenoidal magnetic field.

The streamer tubes are made of 100 μm diameter beryllium-copper wires strung in high resistivity, graphite coated, extruded plastic channels (9 mm \times 9 mm). There are eight channels in a module. The length of the modules varies, the longest being 8.6 m. The tubes are filled with a nonflammable gas mixture of 88% carbon dioxide, 9.5% isobutane and 2.5% argon. The wires are held at a voltage of 4.75 kV, while the channel walls are grounded. Ionizing particles create streamer discharges in the tubes, which in turn induce signals on two external readout electrode sheets sandwiching the module. The combination of a module and electrode sheets is called a chamber.

The readout electrodes are copper-clad fiberglass sheets. One sheet is made up of copper strips that run parallel to the tubes. The other sheet is divided into quadrilateral pads. The strips are used to track muons. The pads dimensions are designed so that when pads on neighboring layers are connected together, they will continue the projective geometry of the LAC.

There are 14 layers of 5 cm thick iron alternating with streamer tube chambers. The WIC is divided into two radial layers, each 2.1 λ thick. Following the seventh and fourteenth iron layers are double layer chambers. There, in addition to the regular layout, is a second tube module, with two layers of strips laid transverse to the tubes. These give two-dimensional information for improved muon tracking. The barrel WIC is segmented into 8 azimuthally symmetric units.

In all, there are approximately 80,000 strip and 8,000 tower channels that are read out. It takes 0.8 ms to read out the entire WIC.

The expected energy resolution of the WIC is $\sigma(E)/E = 80\%/\sqrt{E}$ (E is in GeV), which will give a combined (LAC and WIC) hadronic energy resolution of $\sigma(E)/E = 60\%/\sqrt{E}$ (E is in GeV).

2.3.6 Luminosity Monitor

The integrated luminosity of the SLC is determined by dividing the measured number of Bhabha ($e^+e^- \rightarrow e^+e^-$) events accepted at small polar angles (relative to the beampipe) by the calculated cross section [25, 33, 34]. At small angles, the cross section is dominated by the photon t -channel process (see Fig. 2.24). This cross section has been calculated to high precision. For every hadronic Z^0 decay, there are

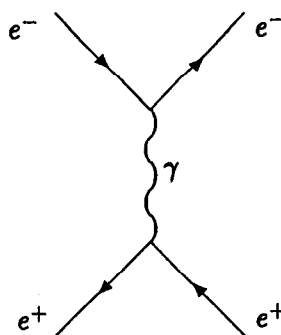


Figure 2.24: Feynman diagram for the t -channel photon process.

approximately 2.5 small-angle Bhabha events.

Two identical luminosity monitors are located on opposite sides of the IP. Each luminosity monitor is made up of 23 tungsten alloy radiator layers alternated with layers of silicon diodes mounted on G10 circuit boards. The tungsten alloy (90% tungsten and 10% Cu-Ni) plates are 3.5 mm thick ($0.92 X_0$) and spaced 8 mm apart. The silicon layers are $300 \mu\text{m}$ thick ($0.003 X_0$) corresponding to a sampling fraction of 1.44% for muons. Each silicon layer is segmented into 160 cells, approximately 1 cm^2 in size, to give angular information (Fig. 2.25). The G10 is $800 \mu\text{m}$ thick ($0.004 X_0$).

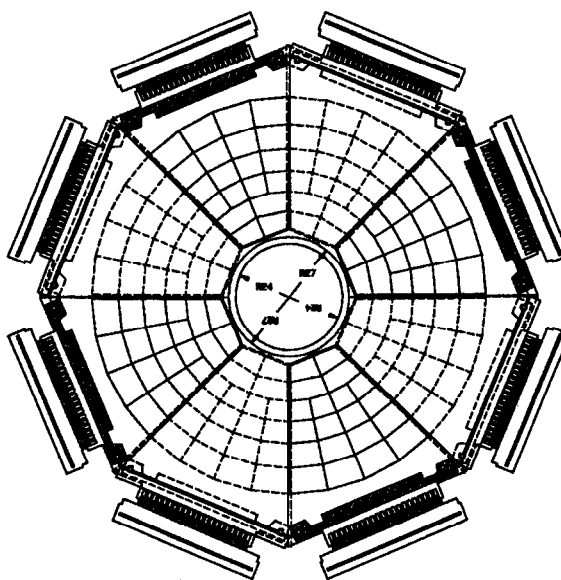


Figure 2.25: Cell layout in the first LUM layer.

Each cell is a reverse biased diode. Therefore, without any incident particles, the current flowing through the diode is only due to thermally excited electrons. When a shower propagates through the diode, the particles ionize atoms in the silicon increasing the current flowing in the diode. The increase in the current is a direct measurement of the energy loss due to ionization.

The first layer of tungsten is 101 cm from the IP. The LUM covers the polar angular region of 28 mrad to 65 mrad. The electronic readout from the cells of the first six layers and those from the remaining 17 layers are grouped together to form two projective towers called LUM-EM1 and LUM-EM2, respectively. The first tower is $5.5 X_0$ and the second is $15.6 X_0$. Together, they contain more than 99.5% of a 45 GeV electromagnetic shower. The resolution of the detector for measuring the energy of electrons is $\sigma(E)/E = 20\%/\sqrt{E}$ (E is in GeV).

Chapter 3

Event Selection

Event selection at the SLD is comprised of two parts. The first is an online event trigger, designed to be as efficient¹ and fast as possible in detecting Z^0 decays, while rejecting background events. An event passing the trigger is written to tape and then analyzed by the second part, an offline filter. This is a higher level process that examines the event characteristics in an attempt to create a data sample of high purity.²

For reasons to be explained in section 3.2, the offline filter was designed to identify events where the Z^0 decayed into either quark or tau pairs. The combined online trigger and offline filter yielded 10,224 such events. The combined online trigger and offline filter efficiency for detecting quark pair events was estimated to be $(90 \pm 2)\%$, based on the measured luminosity [35], and the efficiency for detecting tau events was estimated to be approximately 30%, based on Monte Carlo studies.

Note, as discussed in the paragraph of section 2.3.4 describing the energy scale of the LAC, *all* LAC energies in this chapter are in the muon energy scale. In that scale, Z^0 's decaying into quark pairs deposit ~ 35 GeV in the LAC, while e^+e^- final states deposit ~ 63 GeV.

¹Efficiency refers to one's ability to detect desired events: $\frac{Z^0_{s(\text{detected})}}{Z^0_{s(\text{present})}}$.

²The purity of a sample measures the number of "good" detected events relative to the total number of accepted events, inclusive of backgrounds: $\frac{Z^0_{s(\text{detected})}}{Z^0_{s(\text{detected})+\text{backgrounds}}$.

3.1 Trigger

The components of the SLD used to trigger on an event rely on either tracking (CDC and WIC strips) or calorimetry (LUM and LAC) information. These components process the data quickly (~ 4 msec) in order to accept or veto an event [36]. The SLD data acquisition is described in detail in ref. [37] and will not be discussed here.

The trigger attempts to separate two types of beam backgrounds from the Z^0 decays. One type of background event results from low energy electrons and photons that scatter off various beamline elements and apertures. The trigger vetoes those events by requiring tracks in the CDC to have a large opening angle and the energy deposited in the LAC to be above a threshold. The other background events result from the tails of the electron and positron bunches interacting with collimators, upstream from the IP, creating muons ($Ze^\pm \rightarrow Ze^\pm\gamma \rightarrow Ze^\pm\mu^+\mu^-$)³ that traverse the SLD parallel to the beam pipe. In the LAC, these so-called ‘‘SLC muons’’ deposit small amounts of energy in many towers. The average response of each tower due to ionization by the SLC muons is approximately $\sim 80(200)$ MeV/tower in the EM(HAD) layers [38]. A single SLC muon will typically deposit a total of 3 to 6 GeV in the LAC through ionization. Setting high trigger tower thresholds will reduce their effect. A large number of SLC muons passing through the CDC will produce a large amount of ionization. This can either erroneously set the Tracking trigger (which will be defined momentarily), causing the detector to be read out frequently, leading to a large percentage of time that the detector cannot take data or it can trip the CDC’s high voltage, rendering it inoperable for several minutes until its voltage can be ramped back up. To reduce the effects of periods of noisy beam conditions, the rate that the Tracking trigger can be set is limited. The remaining background sources are dealt with in the offline filter.

There are seven different triggers that cause either all or part of the detector to be read out. They are listed in Table 3.1.

‘‘WAB’’ refers to wide-angle Bhabhas, which are e^+e^- final states ($e^+e^- \rightarrow e^+e^-(\gamma)$) detected in the LAC.

³For this equation, do not confuse the atomic number Z with the Z^0 gauge boson.

Trigger name	Systems read out		Typical rate (Hz)	Description
	Cal. only	ALL		
Energy	✓		0.25	LAC energy is greater than 4 GeV. Towers included in sum are above threshold of 154/154/811/811 MeV for EM1/EM2/HAD1/HAD2.
WAB		✓	< 0.01	EM LAC energy is greater than 15 GeV and the CDC must be ready to take data. Only EM towers above threshold of 154/154 MeV for EM1/EM2 are included in sum.
LUM	✓		0.25	Energy sum for each LUM monitor is greater than 12.5 GeV (electron energy scale). Towers included in sum are LUM-EM2 towers above a 1.25 GeV threshold.
Tracking		✓	0.05	At least 2 CDC tracks, separated by an opening angle ($\delta\phi$) of at least 30° . Rate limited to 0.1 Hz.
Hadronic		✓	0.01	At least 1 CDC track and satisfies Energy trigger.
Muon		✓	0.05	Requires WIC strip tracks in opposite barrel WIC octants. Rate limited to 0.05 Hz.
Random		✓	0.05	Reads out all detector every 2,400 beam crossings. Used for background studies.

Table 3.1: The SLD trigger conditions [34, 39].

As previously stated, the LAC tower trigger thresholds are set higher than the average energy deposited by most SLC muons [38]. The actual readout thresholds, used only to eliminate electronics noise, are much lower (5/8/41/41 MeV for EM1/EM2/HAD1/HAD2).

To be considered a CDC track, the particle must have hit at least nine (out of ten) layers and at least 6 (out of 8) sense wires per cell. The Tracking trigger is rate limited to maximum of 10 triggers every 100 seconds, so that when the background rate is high, the trigger will not continuously fire.

A WIC muon track consists of hits in at least 4 (out of seven) layers in both longitudinal units. Because of the excessive number of SLC muons hitting the WIC, the Muon trigger is rate limited to 0.05 Hz.

Typical readout time [36] for the calorimeters is 90 msec (11 beam crossings), while for the entire detector it's 200 msec (25 beam crossings). For the 1992 run, there were $\sim 10^6$ Energy triggers and 2.6×10^6 total triggers.

3.2 Offline Filter

In principle, all Z^0 decays ($Z^0 \rightarrow f\bar{f}$) can be used to measure A_{LR} . However, the e^+e^- final state contains a significant contribution from the parity conserving t -channel photon exchange, in addition to the s -channel Z^0 decay. Since this contribution dilutes the asymmetry, all e^+e^- events are removed from the data sample. Because of the relatively small branching ratio of $Z^0 \rightarrow \mu^+\mu^-$ (3.3%), combined with the inefficiency of detecting them amidst the SLC muon backgrounds, they are not included in this analysis.

The filter presented here is completely calorimetry based. Under normal conditions, because of the ease and precision available in detecting charged particles in the drift chamber, one would prefer to use it instead of, or at least, in conjunction with the calorimeter. However, only $\sim 80\%$ of all events were recorded with drift chamber data. The reasons for this were alluded to earlier. Under noisy conditions, the CDC would be reading out the previously triggered event, while the LAC was ready for a new one. When the beam conditions were very noisy, the drift chamber high voltage would trip, causing the drift chamber to be off until the high voltage could be brought back up. Furthermore, because the endcap drift chambers were not functional, events that were forward peaked did not have tracking information.

A potential option might have been to use those events where there was drift chamber data, as a cross check on the calorimetry based filter, to identify possible background events. However, the background events that passed the calorimetry based filter were strongly correlated to the very reasons there was no drift chamber data in the first place.

Because the calorimeter is very sensitive to electrons and hadrons, this analysis focuses only on Z^0 's decaying to $q\bar{q}$ and $\tau^+\tau^-$. The tau pairs are included because they decay into leptons and hadrons. The $q\bar{q}$ events are collectively referred to as hadronic Z^0 decays.

The offline filter is a four stage process [40]. The first stage is a pass over all events that set either the Energy or Hadron triggers, in an attempt to identify possible hadronic, $\tau^+\tau^-$ and e^+e^- final states. Figs. 3.1-3.3 are event displays of these

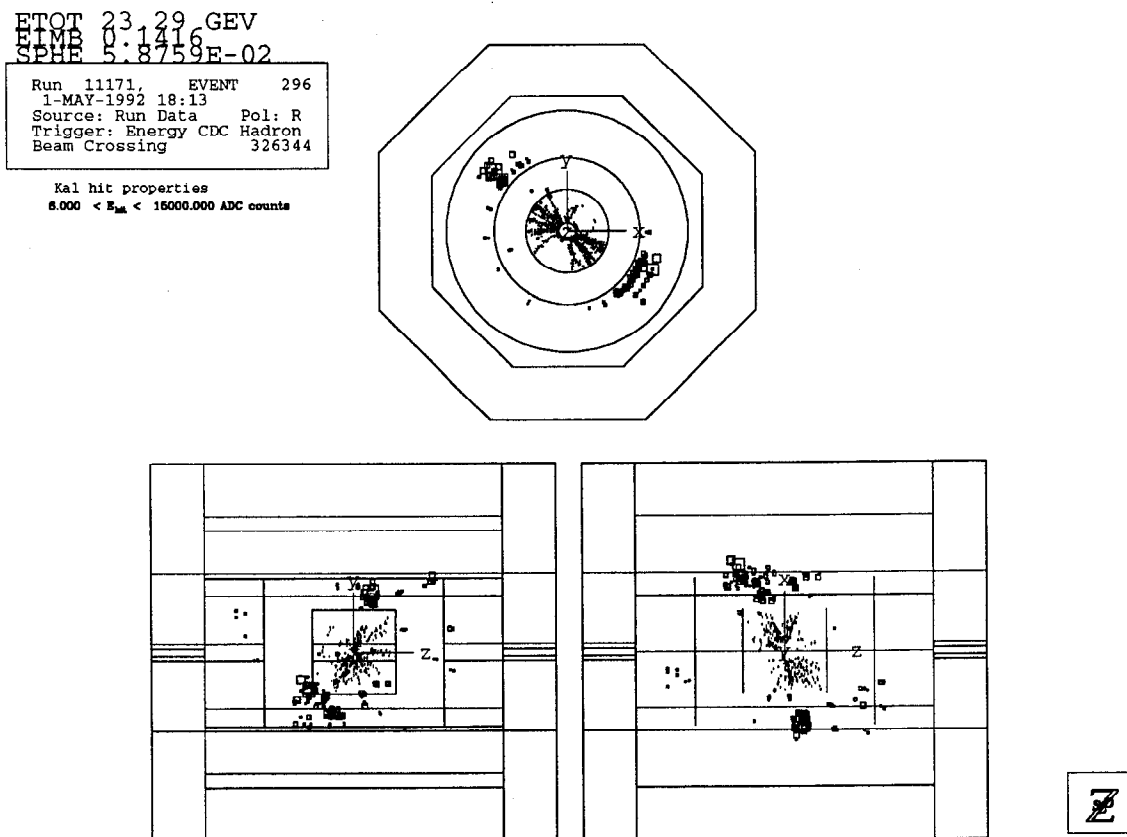


Figure 3.1: Example of hadronic Z^0 decay.

three types of events, showing three views of the detector. The squares in the LAC correspond to tower hits. Their size is proportional to the energy deposited in each tower. Included are cell hits in the central drift chamber. The second stage removes

```

ETOT 11.07 GEV
TIME 0.8873
SPHE 1.0469E-03
Run 11605, EVENT 5906
22-MAY-1992 08:24
Source: Run Data Pol: R
Trigger: Energy CDC Hadron
Beam Crossing 5086486

```

Kal hit properties
 $8.000 < E_{tot} < 16000.000$ ADC counts

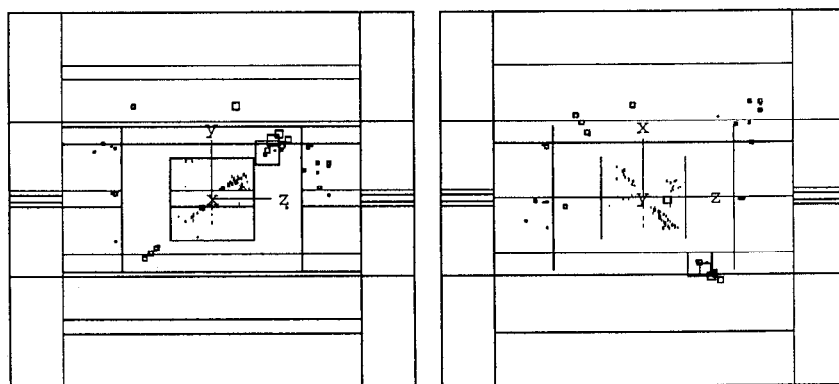
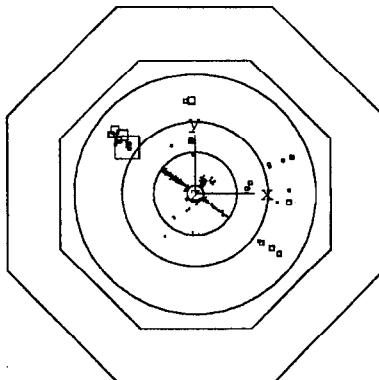


Figure 3.2: Example of a $\tau^+\tau^-$ final state.

the e^+e^- final states. The third stage removes any remaining beam-related background events. The fourth stage is a final quality cut that required a polarization measurement within an hour of the detected Z^0 decay.

3.2.1 First Stage

The first stage makes use of the LAC and endcap WIC pad information. SLC muons tend to produce LAC clusters parallel to the beampipe rather than clusters projecting back to the IP. It is useful to define an energy sum, called E_{tot} , that will exclude those non-projective background hits. Recall (see section 2.3.4) that the HAD towers are segmented transversely into towers which are twice as large as the EM towers in both

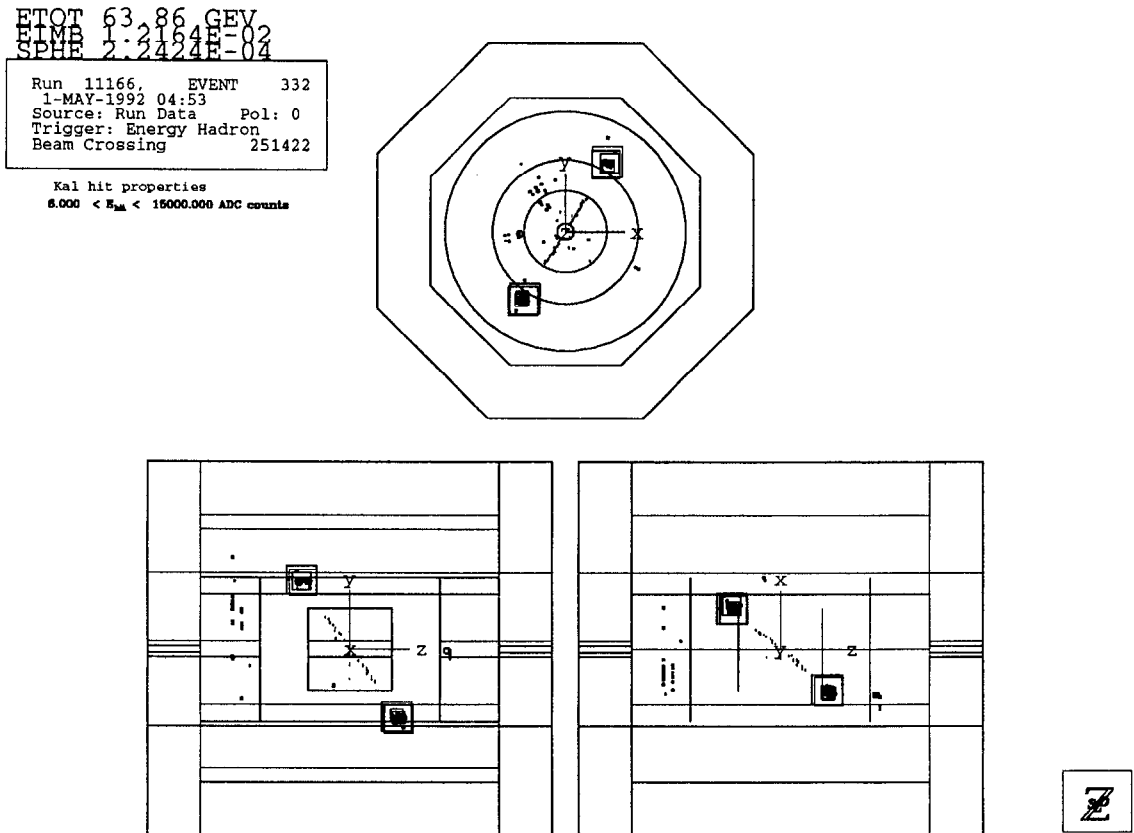


Figure 3.3: Example of a e^+e^- final state.

θ and ϕ . Hence, each HAD tower covers eight corresponding EM towers (four in each of the EM layers). LAC EM towers are included in E_{tot} only if both EM1 and EM2 are hit (for the same θ and ϕ), while the HAD towers are included in E_{tot} only if at least one of the eight corresponding EM towers has been hit.

The calorimeter towers are labelled by bins in polar angle. $\Theta_{bin} = 0$ represents the towers at $\theta = 90^\circ$ (relative to the beampipe). The LAC towers run from $\Theta_{bin} = 0$, in the barrel, to $\Theta_{bin} = \pm 48$, in the endcap regions. Because of the large amount of noise close to the beampipe, $\Theta_{bin} = \pm 48$ were not included in the analysis.

In calculating the quantities E_{tot} , E_{LAC} , E_{imb} , and $SPHE$, tower thresholds of

0/151/811/811 MeV for EM1/EM2/HAD1/HAD2 were used.⁴ These thresholds eliminated most hits due to electronic noise and muon backgrounds.

The selection criteria were as follows:

1. $0 < N_{LAC} < 3000$,

where N_{LAC} is the number of LAC towers above the readout threshold set at 5/8/41/41/ MeV for EM1/EM2/HAD1/HAD2.

2. $E_{LAC} > 14$ GeV,

where E_{LAC} is the sum of all LAC towers above threshold.

3. $E_{WIC}^{endcap} < 11$ GeV and $(E_{tot} - 0.69E_{WIC}^{endcap}) > 6$ GeV,

where E_{WIC}^{endcap} is the sum of the endcap WIC towers with less than 8.7 GeV/tower.

4. $E_{imb} < 0.9$,

where E_{imb} is the energy imbalance in the LAC, defined as

$$E_{imb} \equiv \frac{1}{E_{tot}} \sqrt{\left(\sum_{i=1}^n E_{x,i}\right)^2 + \left(\sum_{i=1}^n E_{y,i}\right)^2 + \left(\sum_{i=1}^n E_{z,i}\right)^2}, \quad (3.1)$$

$E_{x,i}$, $E_{y,i}$ and $E_{z,i}$ are the x , y and z components of the i^{th} tower included in E_{tot} .

5. $(E_{imb} + SPHE) < 1.0$,

where $SPHE$ is the sphericity of the event, defined as

$$SPHE = \frac{3 \sum_{i=1}^n (p_{t,i})^2}{2 \sum_{i=1}^n (p_i)^2}, \quad (3.2)$$

where p_i and $p_{t,i}$ are the i^{th} particle's momentum and transverse momentum relative to the event's jet axis. The jet axis of an event is found by minimizing the sum over $(p_{t,i})^2$.

⁴The threshold for EM1 was inadvertently set at 0, instead of 151 MeV. This was noticed only after much of the data had been filtered, however, since it produced a negligible effect no attempt was made to rectify the error.

Cuts (3), (4) and (5) were specifically designed to remove SLC muons from the data sample. After applying all five cuts to the triggered events, 13,478 events remained. Fig. 3.4 shows the distribution of the variables for events passing the selection criteria.

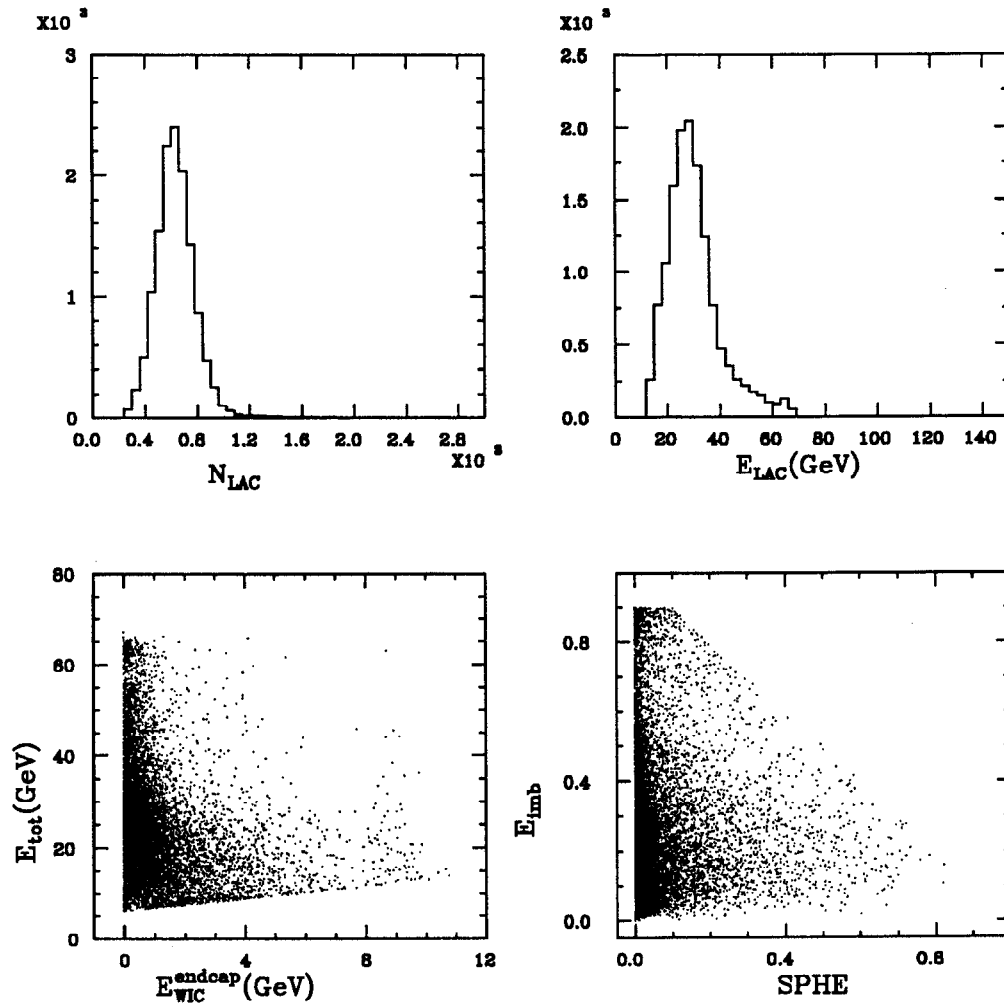


Figure 3.4: Distributions of variables used in the first filter stage.

Fig. 3.5 shows the distribution of E_{tot} versus E_{imb} . Beam-related background events due to SLC muons populate the large E_{imb} region, e^+e^- final state events can be seen around $E_{tot} \approx 60$ GeV and hadronic decays have $E_{tot} \approx 25$ GeV.

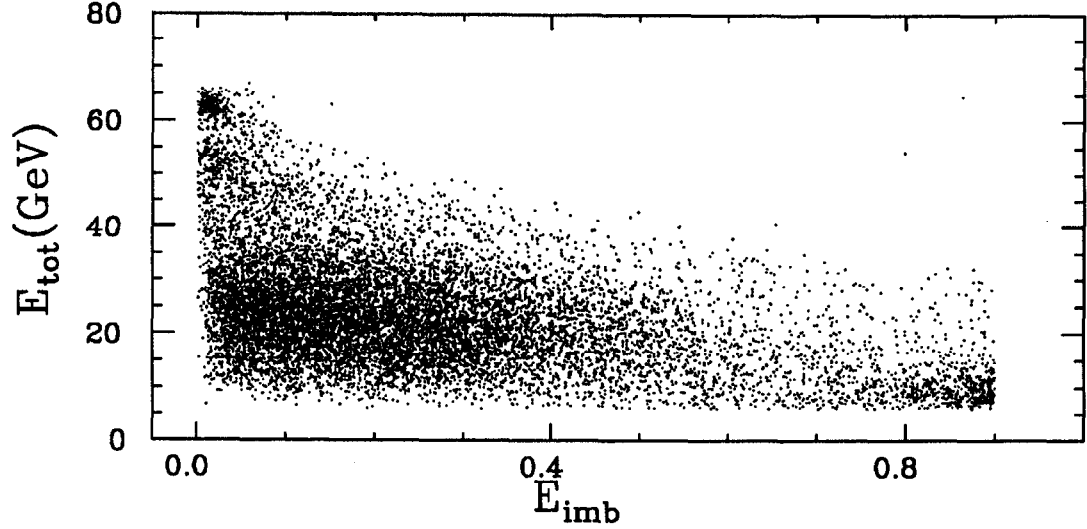


Figure 3.5: Scatter plot of E_{tot} versus E_{imb} .

3.2.2 Second Stage

At this stage, the e^+e^- final states are removed from the sample. Detector simulations have shown that approximately 95% of the total energy of a e^+ or e^- from a e^+e^- final state is contained in a volume the size of a single LAC EM section tower. In practice, the lateral width of the showers is slightly larger than that of a single LAC EM tower. A quantity S_4 is defined as the sum of the energy of the two towers with the maximum energy in EM1 and the two towers with the maximum energy in EM2, all above a 1 GeV threshold. Thus, if the e^+ and e^- each strike the middle of a tower, for an event with an E_{tot} of 60 GeV, S_4 equals approximately 57 GeV. An additional quantity, Θ_{max} , is defined as the $|\Theta_{bin}|$ of the tower having the largest EM1 energy. Events were identified as e^+e^- final states if

$$S_4 > \begin{cases} 18.8 \text{ GeV}, & \Theta_{max} \leq 44, \\ 7.7 \text{ GeV}, & \Theta_{max} > 44. \end{cases} \quad (3.3)$$

The angular dependence of S_4 is clearly demonstrated in Fig. 3.6, a scatter plot of S_4 versus Θ_{max} for all events that passed the first filter. There are several reasons for the low S_4 thresholds used in eq. 3.3. In both the barrel and endcaps, if the e^+ or e^- showers do not originate in the middle of the tower, the energy is shared by two

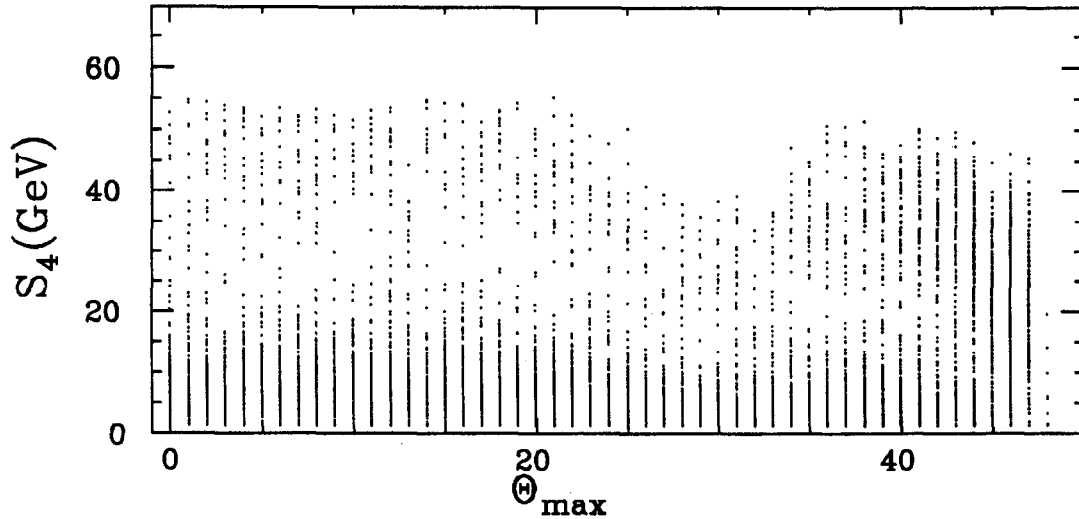


Figure 3.6: Scatter plot of S_4 versus Θ_{max} for all events passing the first stage.

or more adjacent towers, thereby lowering the measured value of S_4 . In the overlap region of the barrel and endcap ($\Theta_{max} \approx 30$), the energy is spread over many towers resulting in a dip in S_4 . The energy response of the endcap LACs is lower than that of the barrel. It is believed that the low response is the result of excess material in front of the endcaps which leads to preshowering of the incident electron and positron. The events are separated into two regions of Θ_{max} in response to further degradation of the energy response in the very forward regions. 1865 events satisfied these criteria and were removed from the overall data sample.

3.2.3 Third Stage

Beam-related background events are removed at this stage. SLC muons typically deposit small amounts of energy in each LAC tower. Therefore, by requiring an event to have two EM towers above a 0.31 GeV threshold and that those towers be in opposite hemispheres of the detector successfully removes most backgrounds.

$M_1(M_2)$ is the maximum tower energy in the EM layers of the forward (backward) hemisphere. A cut is made on the smallest acceptable value for the minimum of M_1 and M_2 . In addition, tighter cuts on E_{tot} and E_{imb} will help remove backgrounds.

Good hadronic and tau pair events are required to pass the following criteria:

1. $10 < E_{tot} < 70$,
2. $E_{imb} < 0.8$,
3. $\text{Min}(M_1, M_2) > 0.31 \text{ GeV}$.

Fig. 3.7 shows a scatter plot of $\text{Min}(M_1, M_2)$ versus E_{imb} , before the selection was made, for events not removed by the second stage. This stage removed 1,176 events, leaving 10,437 events.

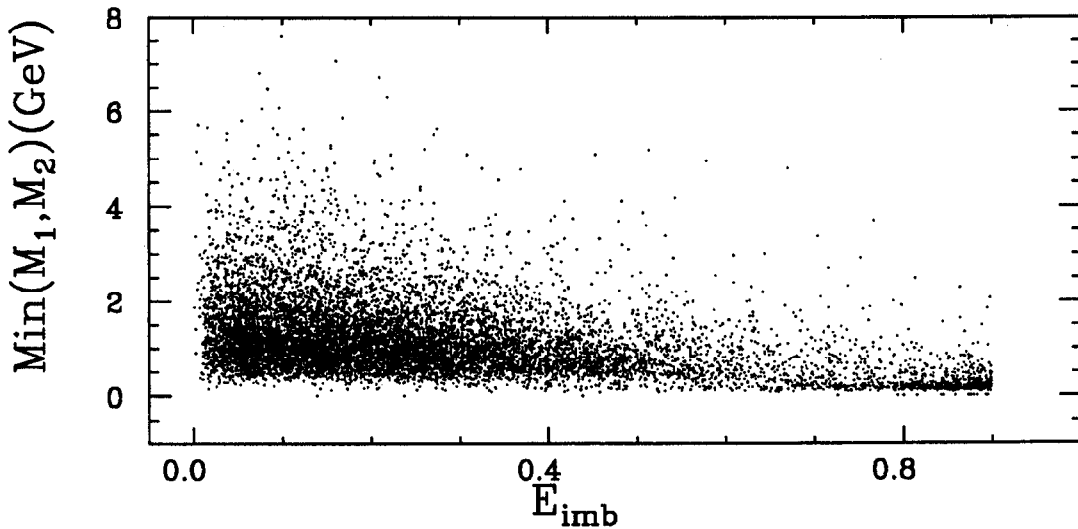


Figure 3.7: Scatter plot of $\text{Min}(M_1, M_2)$ versus E_{imb} .

3.2.4 Fourth Stage

Polarization measurements were made approximately every 3 minutes during the SLD run. Each detected Z^0 was aligned with the nearest polarization measurement to determine the beam polarization. However, occasionally, the Compton polarimeter was shut down for periodic maintenance. In order to ensure that the electron polarization measured with the Compton polarimeter reflected the beam conditions when the Z^0 was detected, it was required that the polarization measurement take place within

an hour of the detected event. This removed 213 events, leaving 10,224 events in the final event sample. Fig. 3.8 shows the distribution of E_{tot} for the final sample. Recall that the LAC response to hadronic events is typically ~ 35 GeV in the muon energy scale. Because E_{tot} includes the effects of high tower thresholds and a clustering routine designed to remove towers hit by SLC muons, the mean value of E_{tot} is only ~ 21 GeV.

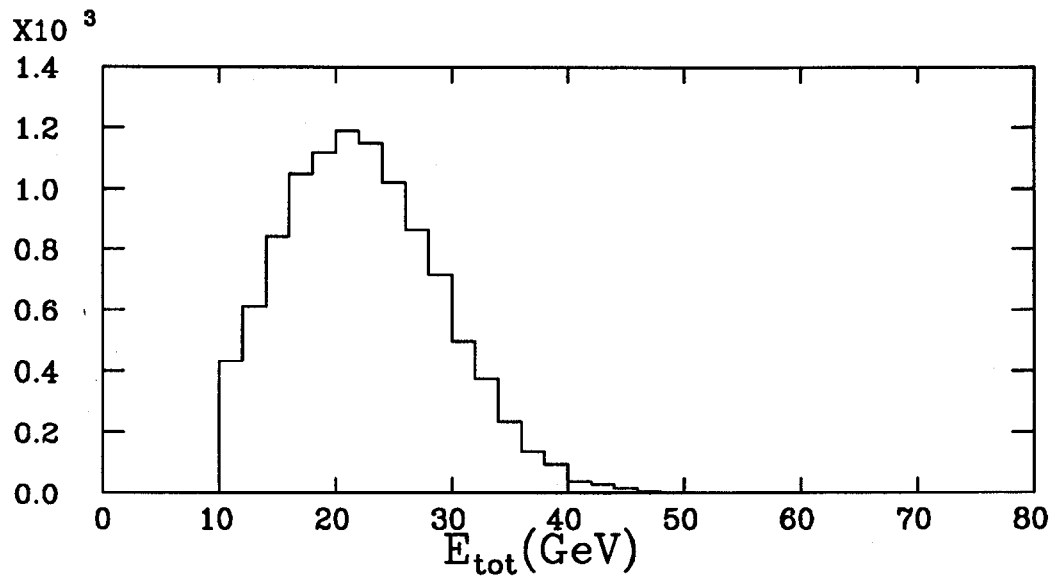


Figure 3.8: E_{tot} for the final event sample.

3.3 Backgrounds

The background events fall into two major categories [41]. The first is a direct result of e^+e^- interactions. These include e^+e^- final state, 2γ , and $\gamma\gamma$ processes. The second category consists of the beam-related and cosmic-ray background events.

3.3.1 e^+e^- Interactions

3.3.1.1 e^+e^- Final State (WAB)

The major source of backgrounds are the e^+e^- final states ($e^+e^- \rightarrow e^+e^-(\gamma)$). The second stage filter relies on the fact that the electrons and positrons deposit 95% of their energy in a small number of LAC EM towers. There are a number of cases that do not satisfy this criterion. If either the electron or positron radiates a hard photon, the energy will be distributed over more towers and the event might not be identified as a WAB (see Fig. 3.9).

```

ETOT 23.57 GEV
ELMB 0:3247
SPHE 0:1837
Run 12929    EVENT 1668
20-JUL-1992 04:53
Source: Run Data    Pol: R
Trigger: Energy Hadron WAB
Beam Crossing 2086518379

```

Kal hit properties
 $6.000 < E_{\text{hit}} < 16000.000$ ADC counts

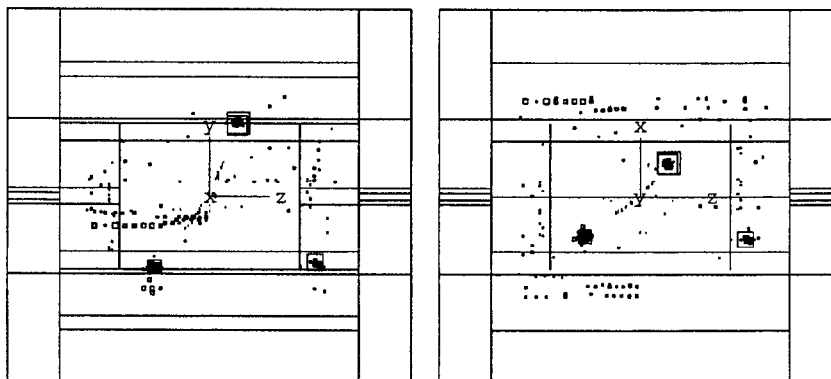
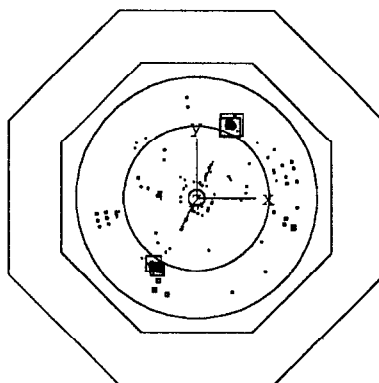
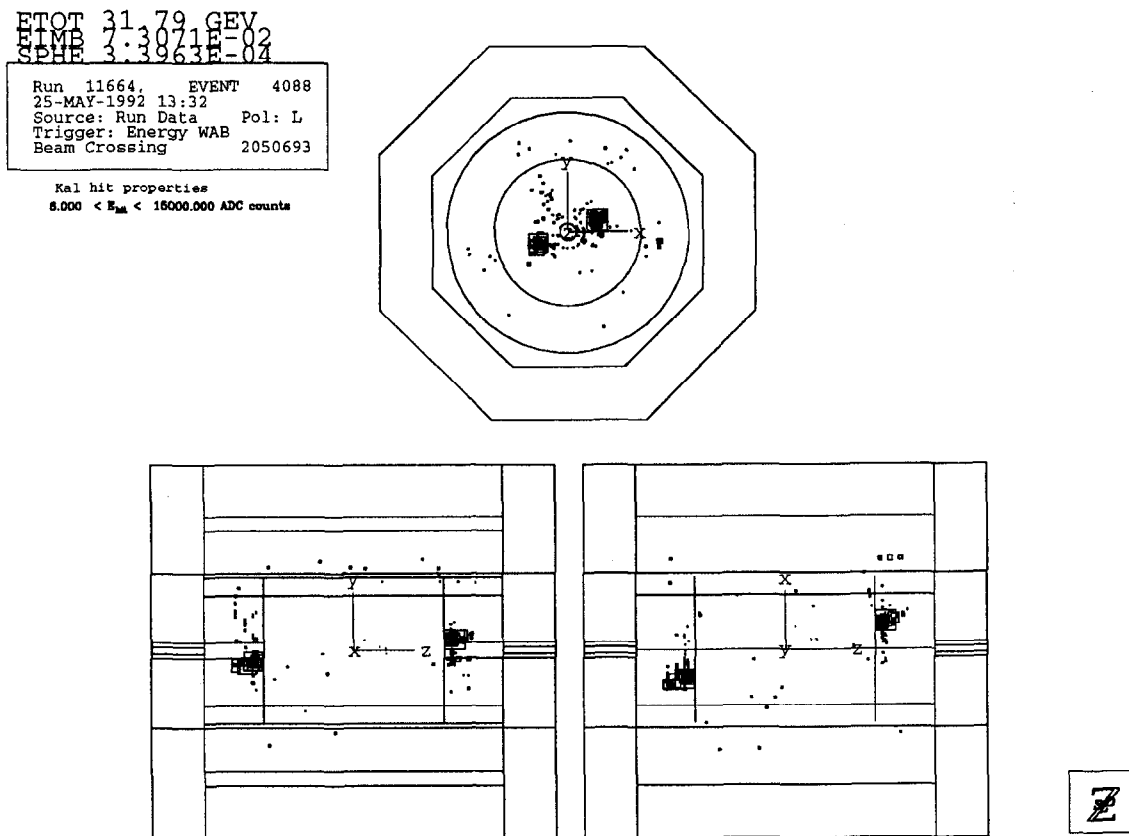


Figure 3.9: $e^+e^- \rightarrow e^+e^-\gamma$

The endcap fiducial region is particularly problematic. WABs detected in the endcap LAC typically have broader clusters and lower energy than those in the barrel LAC (see Fig. 3.10).



An additional region of the detector that is problematic for the filter is the overlap region between the barrel and the endcap. In that region, clusters tend to get broken up between the two sections of the LAC (the barrel and endcap) causing the energy to be spread out over many towers (see Fig. 3.11).

```

ETOT 32.57 GEV
ETIMB 9.6815E-02
SPHE 1.8366E-04

Run 12393,   EVENT 1616
25-JUN-1992 19:25
Source: Run Data   Pol: L
Trigger: Energy WAB
Beam Crossing 1833594194

Kal hit properties
6.000 < Ehit < 15000.000 ADC counts

```

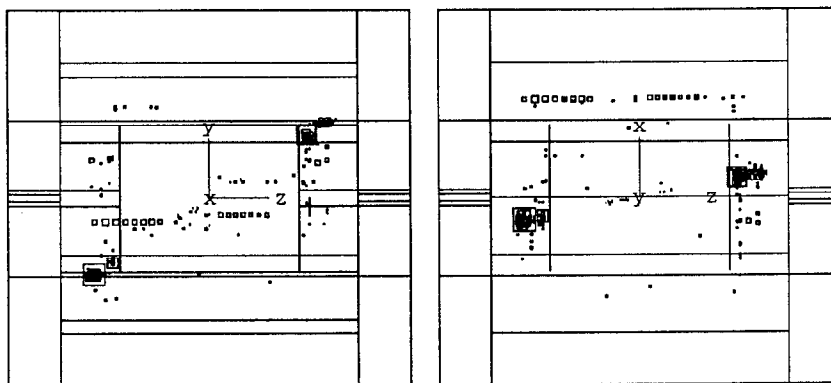
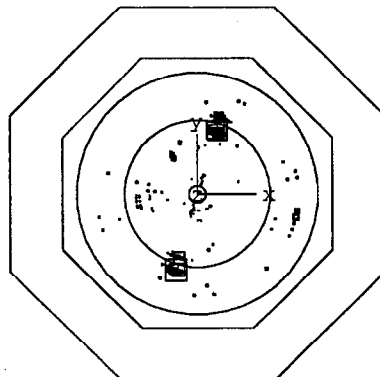


Figure 3.11: WAB event in the barrel-endcap overlap region.

3.3.1.2 Two-Photon Process (2γ)

The 2γ process ($e^+e^- \rightarrow e^+e^-\gamma^*\gamma^* \rightarrow e^+e^-X$) should not be confused with the $\gamma\gamma$ process, which will be explained in the next section (see Fig. 3.12). The SLD 2γ Monte Carlo generator predicts that for $\sqrt{s} = M_Z$, the total 2γ cross section (with the invariant mass of the two photon system, W , greater than 5 GeV) to be 6.5 nb. LEP's measured hadronic cross section of Z^0 decays of 30 nb [42] makes the 2γ process a significant source for backgrounds. It turns out that most of the 2γ events are very forward peaked and do not deposit a significant amount of energy in the fiducial region of the SLD ($|\Theta_{bin}| < 48$ or equivalently $|\cos\theta| < 0.985$). Based on the Monte Carlo, an upper limit of 3 events, at the 95% confidence level, are expected

to pass the selection process. The only events that passed the selection process were $e^+e^- \rightarrow e^+e^-e^+e^-$, where only one electron and one positron were detected in the endcap LAC. This has the same signature as that of a WAB event.

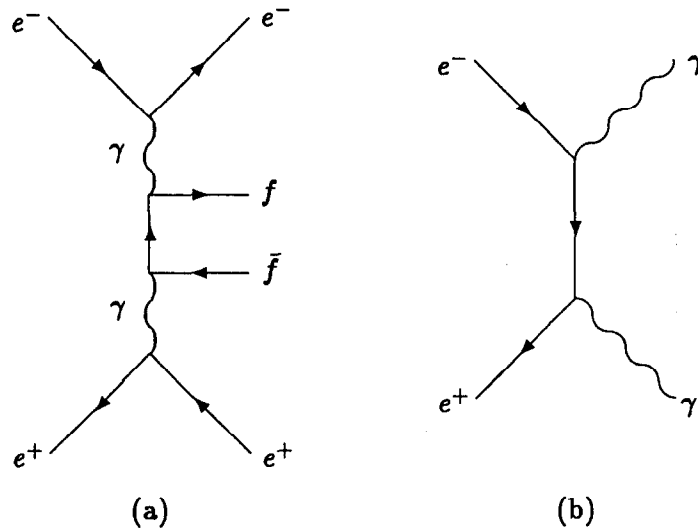


Figure 3.12: Feynman diagrams for (a) 2γ process and (b) $\gamma\gamma$ process.

3.3.1.3 Gamma-Gamma Process ($\gamma\gamma$)

The $\gamma\gamma$ process ($e^+e^- \rightarrow \gamma\gamma$) is a pure QED process (see Fig. 3.12(b)). The reaction takes place through the exchange of a virtual electron in the t -channel. The differential cross section is given by

$$\frac{d\sigma}{d\Omega} = \frac{\alpha^2}{s} \frac{1 + \cos^2\theta}{1 - \cos^2\theta} \left(1 \pm \frac{s^2}{2\Lambda_{\pm}^4} (1 - \cos^2\theta) \right), \quad (3.4)$$

where the first term is the lowest order QED term and the second term parameterizes any deviations from QED [43]. θ is the average polar angle, relative to the beampipe, of the two photons. Several experiments at LEP have measured the process [44] and set lower limits on Λ_{\pm} . Fig. 3.13 shows the dependence of the cross section on $\cos\theta$. The solid line is the lowest order QED term, while the dotted lines show the limits of deviations from it. Included are the smallest values for Λ_{\pm} , measured by DELPHI [44], giving the largest deviations for the differential cross section. Integration of eq. (3.4)

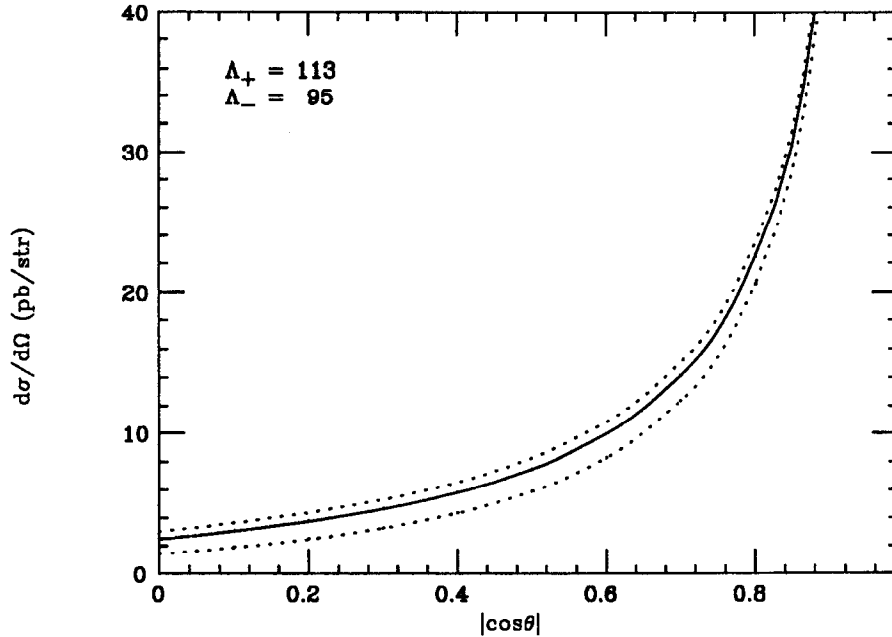


Figure 3.13: Differential cross section for $e^+e^- \rightarrow \gamma\gamma$.

for $|\cos\theta| < 0.985$ yields

$$\sigma(e^+e^- \rightarrow \gamma\gamma) = 61_{-9}^{+4} \text{ pb.} \quad (3.5)$$

The signature for the $\gamma\gamma$ process is two back-to-back 45 GeV photons, the same as for WABs.

3.3.2 Beam-Related and Cosmic-Ray Backgrounds

There are three different types of non- e^+e^- interactions seen at the SLD. Each will be described separately, however, in the final analysis, one must take into account the possible superposition of all three types creating a single background event.

3.3.2.1 SLC Muons

The predominant mechanism for SLC muons to interact with the LAC is through ionization of the liquid argon. The muons deposit small amounts of energy in long,

narrow clusters that are almost parallel to the beam pipe. Their effect is relatively insignificant and the filters are able to remove them. Occasionally, the muons interact with the material in the LAC through radiative processes (e.g. bremsstrahlung, pair production and photonuclear interactions). These interactions tend to deposit a considerable amount of energy (~ 10 GeV) in 2 to 10 towers. The resulting showers are broader than those caused solely by ionization. These events can slip through the filters (see Fig. 3.14).

```

ETOT 20.00 GEV
ETIMB 0.4086
SPHE 2.0492E-02

Run 11341, EVENT 4845
9-MAY-1992 07:28
Source: Run Data Pol: R
Trigger: Energy WAB
Beam Crossing 231771

```

Kal hit properties
 $8.000 < E_{\text{cal}} < 16000.000$ ADC counts

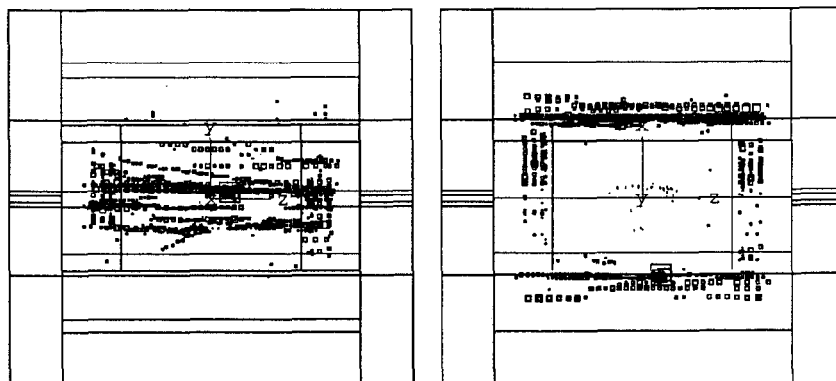
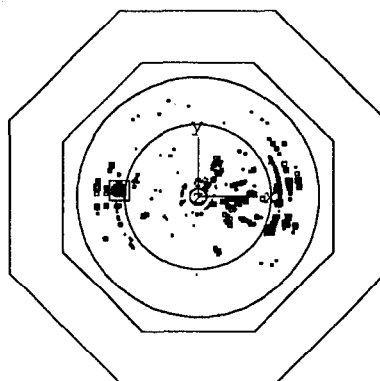


Figure 3.14: High multiplicity SLC muon event.

3.3.2.2 Beam-Gas and Beam-Wall Interactions

At issue here is the interaction of the beam with any particles inside the beampipe or with the beampipe itself. Due to the high vacuum and low average beam current in the SLC, it is expected that the number of beam-gas events is negligible. Beam-wall events tend to be imbalanced and deposit a small amount of energy in the LAC (see Fig. 3.15).

3.3.2.3 Cosmic Rays

Muon cosmic rays can deposit a large amount of energy in the LAC through the different radiative processes previously listed. Fig. 3.16 is an example of a cosmic event. Non-muon cosmic events are easily identifiable by their large energy imbalance.

3.3.3 Background Estimation

Due to the fact that the present detector simulation does not accurately describe the data, an alternative method for measuring the number of background events is needed. With $\sim 10,000$ events, it is possible to solve this problem by hand scanning all the events [41].

The background events can be classified into two categories:

- background events that are detectable (by the scanners) using well defined scan criteria,
- background events that are indistinguishable (by the scanners) from Z^0 decays.

The first category involves establishing a well defined set of criteria for what is to be considered a background event. Based on the results of the scan, two separate, yet correlated, analysis methods are used to estimate the total number of background events. The scanning efficiency method is described in [45]. The maximum-likelihood technique is presented in [46]. Fundamentally, both methods use the results from one scanner to measure the efficiency of the other scanner at detecting background events, thereby making an estimation of the overall scanning efficiency.

```

ETOT 13.98 GEV
TIME 0:27:04
SPHE 1.9607E-02
Run 13686, EVENT 3427
17-AUG-1992 00:46
Source: Run Data Pol: R
Trigger: Energy Hadron
Beam Crossing -1919918447

```

Kal hit properties
 $8.000 < N_{\text{hit}} < 16000.000$ ADC counts

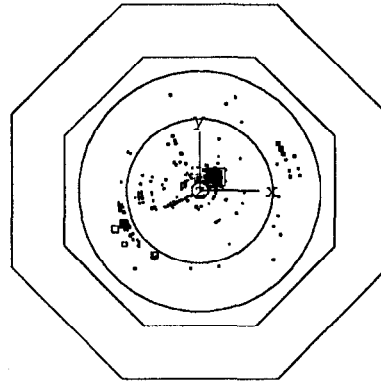


Figure 3.15: Beam-gas/beam-wall event.

The background estimation is carried out for all 10,437 events passing the third stage filter. Because there is no correlation between the background events and the polarization measurement, these results can then be scaled down to the smaller (10,224) event sample remaining after the fourth stage.

The scanners identified 191 events as backgrounds. The backgrounds were separated into two groups, e^+e^- interactions and beam-related (which included cosmic rays). The number of events seen by each scanner is listed in Table 3.2. There is a slight difference between the number of overlap events for each background type versus that for all backgrounds. The discrepancy is a result of scanner #1 identifying

ETOT 14.56 GEV
 TIME 0.5791
 SPHE 0.2653

Run 13506, EVENT 4497
 10-AUG-1992 00:37
 Source: Run Data Pol: R
 Trigger: Energy
 Beam Crossing -1992559856

Kal hit properties
 $8.000 < E_{\text{hit}} < 16000.000$ ADC counts

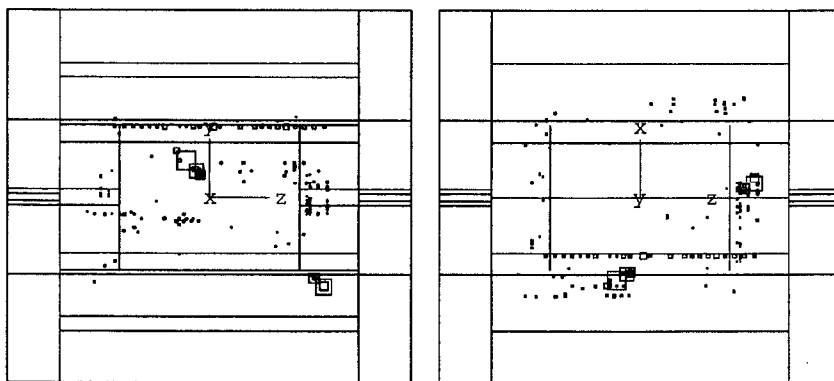
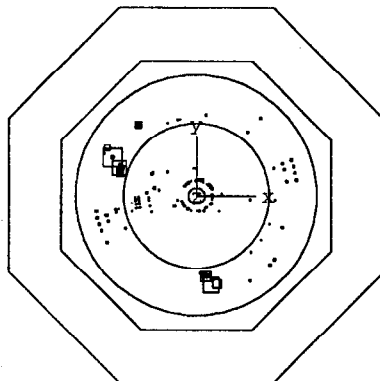


Figure 3.16: Cosmic-ray event.

Background type	Scanner #1	Scanner #2	Overlap between #1 and #2
e^+e^- interactions	75	88	49
Beam-related	71	72	64
All backgrounds	146	160	115

Table 3.2: Results of the background scan.

two events as beam-related events, while scanner #2 identified the same events as e^+e^- interaction events.

The results of both analysis methods can be found in Table 3.3. The errors using the maximum-likelihood method are given at the 95% confidence level.

Analysis technique	Background type	Number of Background Events	% of Event Sample
Scanning Efficiency	e^+e^- interactions	135 ± 29	1.3
	Beam-related	80 ± 17	0.8
	All backgrounds	203 ± 30	1.9
Maximum-likelihood	e^+e^- interactions	133^{+19}_{-12}	1.3
	Beam-related	80^{+3}_{-0}	0.8
	All backgrounds	202^{+12}_{-7}	1.9

Table 3.3: Results of the background analysis.

The scanning criteria used were looser than those needed to satisfy all the assumptions made by the analysis techniques. Specifically, both techniques assume the probability of identifying a background event out of all events is constant for all events. The point is that with well defined scanning criteria the process is completely objective. The only reason for a scanner to miss a background event is due to their inefficiency. It should not be the result of one scanner systematically identifying one class of events as backgrounds while the other scanner believes they are valid Z^0 events. A conservative estimate of the error on the number of background events is taken to be the sum of events seen exclusively by each scanner. This overestimation of the error will account for any systematic scanning discrepancies.

Two classes of background events fall into the second category of those events that are indistinguishable from Z^0 decays. The first are those events that result from two independent clusters that happen to be back-to-back (e.g. two overlapping beam-wall events). By looking at random-trigger events, it is estimated that only 0.8 ± 0.7 background events will satisfy this condition. The second class is made up of events where the two clusters are a direct result of a *single* interaction. The only example of the latter class is a cosmic ray that pierces the detector *and* passes (or at least its shower passes) through the interaction point⁵ *and* deposits enough energy

⁵The hand scan would have identified any cosmic shower that did not pass through the interaction point.

in the LAC, on both sides of the interaction point, in order to pass both the energy threshold and energy imbalance cuts. Based on the rate of cosmic-ray particles and their interaction with the material in the detector, less than 1.4 cosmic-ray events are expected to satisfy these conditions.

The final tally of background events is given in Table 3.4. Because the “Two correlated clusters” result is an upper limit, no error is given. The remaining errors are added in quadrature.

Estimation technique	Number of background events	% of event sample
Hand scan	203 ± 76	1.9 ± 0.7
Two independent clusters	0.8 ± 0.7	0.008 ± 0.007
Two correlated clusters	< 1.4	< 0.013
Total	205.2 ± 76	2.0 ± 0.7

Table 3.4: Summary of all types of background events.

Of the 191 events identified as background events, only 11 events were later removed by the fourth filtering stage. The remaining 180 events were made up of 97 LH and 83 RH polarized events. They have a negligible effect on A_{LR} .

Chapter 4

Analysis

Extracting the final answer from the data involves understanding the contributions of the experimental and theoretical systematic uncertainties to the measurement. For the present data sample (the 1992 run), the dominant uncertainty in the measurement of A_{LR} is the statistical uncertainty (see section 4.3). However, because the technologies needed to reduce the statistical uncertainty, higher polarization and higher luminosity, are currently available (see section 5.5), this chapter will spend more time analyzing the other uncertainties, which will eventually limit the precision of the measurement.

4.1 Experimental Systematic Uncertainties

The expression in eq. 1.63,

$$A_{LR} = \frac{A_{LR}^{exp}}{P_-} = \frac{1}{P_-} \left[\frac{N_L - N_R}{N_L + N_R} \right], \quad (4.1)$$

gives the relationship between the theoretical quantity A_{LR} and the experimental observables A_{LR}^{exp} and P_- . The precision to which these observables are measured limits the precision at which theoretical predictions can be verified.

4.1.1 Luminosity-weighted Average Polarization

Of the 10,224 events (N) identified as Z^0 decays, 5226 were produced with LH electron polarization (N_L) and 4998 were produced with RH electron polarization (N_R). This leads to

$$A_{LR}^{exp} = 0.0223. \quad (4.2)$$

Fig. 4.1(a) is a plot of the electron beam polarization associated with each Z^0 versus the event number. Fig. 4.1(b) is the average polarization for all Z^0 's. The luminosity-

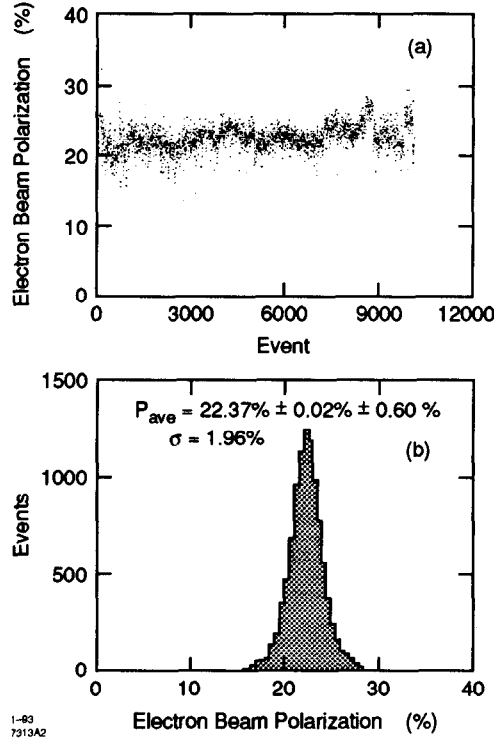


Figure 4.1: Electron beam polarization for the final event sample. (a) time history of the polarization (b) average polarization for all Z^0 's.

weighted average polarization P_e is estimated from the polarization measurement associated with each Z^0 , P_-^i , to be

$$P_e \equiv \frac{1}{N} \sum_{i=1}^N P_-^i = [22.37 \pm 0.02(\text{stat}) \pm 0.60(\text{syst})] \% \approx [22.4 \pm 0.6] \%. \quad (4.3)$$

The contribution of the polarization to the uncertainty in A_{LR} is

$$\frac{\delta A_{LR}}{A_{LR}} = \frac{\delta P_e}{P_e} = \pm 2.7\%. \quad (4.4)$$

4.1.2 Helicity Dependent Systematic Effects

Eq. 4.1 is an oversimplification of the relationship between the theoretical quantity A_{LR} and the experimentally measured quantities. Taking into account polarization-correlated effects, the expression becomes

$$A_{LR} = \frac{\frac{N_L - N_L^b}{\epsilon_L \mathcal{L}_L} - \frac{N_R - N_R^b}{\epsilon_R \mathcal{L}_R}}{P_R \frac{N_L - N_L^b}{\epsilon_L \mathcal{L}_L} + P_L \frac{N_R - N_R^b}{\epsilon_R \mathcal{L}_R}}, \quad (4.5)$$

where: $N_L^b(N_R^b)$ is the number of LH (RH) background events; $\mathcal{L}_L(\mathcal{L}_R)$ is the luminosity for LH (RH) electron beam orientation; the detector's response function $\epsilon_L(\epsilon_R)$ is the product of the acceptance and the efficiency ($\epsilon = acc \times eff$) for detecting LH (RH) polarized Z^0 decays; and $P_L(P_R)$ is the luminosity weighted average LH (RH) beam polarization.

When all these effects are small, eq. 4.5 can be expanded to first order in the relative contributions of each effect:

$$A_{LR} \approx \frac{A_{LR}^{exp}}{P_e} + \frac{1}{P_e} \left[A_{LR}^{exp} f_b + (A_{LR}^{exp})^2 A_P - A_{\mathcal{L}} - A_{\epsilon} - E_{cm} \frac{\sigma'_u(E_{cm})}{\sigma_u(E_{cm})} A_E \right], \quad (4.6)$$

where: the electron polarization P_- in eq. 4.1 has been replaced by the luminosity-weighted average polarization P_e ; f_b is the fraction of background events (see Table 3.4); $\sigma_u(E_{cm})$ is the unpolarized Z^0 cross section at $E = E_{cm}$; $\sigma'_u(E_{cm})$ is the derivative of the cross section at $E = E_{cm}$; $A_P, A_{\mathcal{L}}, A_{\epsilon}$ and A_E are the left-right asymmetries of the polarization, luminosity, response and energy, respectively. The energy asymmetry term does not come from eq. 4.5. Rather, for completeness, it is included now as an additional term and will be justified in section 4.1.2.5.

Each term in the square brackets is a correction to the simple expression in eq. 4.1. The uncertainty of each term translates into a systematic uncertainty in A_{LR} . In what follows, each term will be isolated and the estimation of the correction factor and systematic uncertainty in A_{LR} will be written down.

4.1.2.1 Background Fraction

The background fraction was estimated in section 3.3.3 to be $f_b = (2.0 \pm 0.7)\%$. This leads to a correction factor of

$$\frac{\delta A_{LR}}{A_{LR}} = (2.0 \pm 0.7)\%, \quad (4.7)$$

where the first term is the correction to A_{LR} and the second is the contribution to the systematic uncertainty in A_{LR} resulting from the estimation of f_b

4.1.2.2 Polarization Asymmetry

The polarization asymmetry is determined by measuring the average polarization of each helicity state for all polarimeter runs. A_P was measured to be $-(2.9 \pm 0.1) \times 10^{-3}$, which gives

$$\frac{\delta A_{LR}}{A_{LR}} = -[(6.5 \pm 0.2) \times 10^{-3}] \%. \quad (4.8)$$

4.1.2.3 Luminosity Asymmetry

A luminosity asymmetry might exist if, for example, the Polarized Light Source, used to create the electron beams, produces photon beams of different intensities for different photon polarization states (see section 2.1.1.1). $A_{\mathcal{L}}$ can be measured using two techniques. The first is to use the luminosity monitor [34] to measure \mathcal{L}_L and \mathcal{L}_R . This gives $A_{\mathcal{L}} = (1.9 \pm 6.2) \times 10^{-3}$. The error is dominated by limited statistics (only $\sim 25 \times 10^3$ luminosity events were measured). The theoretical prediction for $A_{\mathcal{L}}$ is $\sim (3 \times 10^{-4})P_e$. This is a result of small contributions from the Z^0 s -channel and the Z^0 s -channel/ γ t -channel interference term to the dominant γ t -channel.

A more precise technique is to use the SLC beam parameters to estimate $A_{\mathcal{L}}$. The luminosity is given by

$$\mathcal{L} = f \frac{N^- N^+}{4\pi\sigma^2} e^{-\frac{\Delta^2}{2\sigma^2}}, \quad (4.9)$$

where: f is the frequency of collisions; $N^-(N^+)$ is the number of electrons (positrons) in a bunch; Δ is the electron-positron beam offset; and $4\pi\sigma^2 = 1/2 [4\pi(\sigma_-^2 + \sigma_+^2)]$ is

the average area of the electron and positron beam spots. σ_- and σ_+ are the widths of the electron and positron bunches (it is assumed that the bunches are round). N^- and Δ are measured directly by measuring the electron beam current and the position of the beam's centroid. The spot size is not directly measured, but is inferred from the measurement of the beamstrahlung monitor (BSM).¹ The beamstrahlung signal is a function of both N^- and σ_- . Measuring the asymmetries of N^- , Δ , and the BSM leads to a luminosity asymmetry of $A_C = (1.8 \pm 4.2) \times 10^{-4}$ which gives

$$\frac{\delta A_{LR}}{A_{LR}} = -(0.8 \pm 1.9)\%. \quad (4.10)$$

4.1.2.4 Response Asymmetry

For any given decay mode of the Z^0 , A_ϵ measures the difference in the detector's response to LH and RH polarized Z^0 decays (see Fig. 4.2). As stated in section 1.4.1,

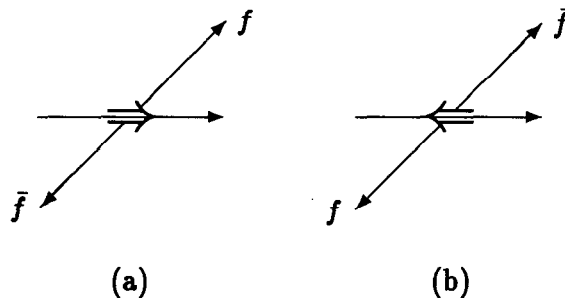


Figure 4.2: Polarized Z^0 decays for (a) a RH polarized Z^0 and (b) a LH polarized Z^0 . The thin horizontal arrow indicates the direction of motion of the incident electron, while the wide horizontal arrow indicates the polarization state of the Z^0 .

the SLD has an azimuthally symmetric solenoidal field and a calorimeter that is symmetric in both azimuth and polar angle. This leads to the detector's response function to fermions being even under parity transformations (detection of a fermion in both the forward and backward directions is equally probable) and equal to the detector's response function to antifermions. Therefore, regardless of the polar angle acceptance of the detector, for any given decay mode, ϵ_L and ϵ_R are equal. The two decays depicted in Fig. 4.2 have an equal probability of being detected so that $A_\epsilon = 0$.

¹Particles bent in the beam-beam interaction radiate synchrotron radiation called "beamstrahlung" [10].

4.1.2.5 Energy Asymmetry

If the cm energy for LH (E_{cm}^L) and RH (E_{cm}^R) polarized electrons is different, then the cross sections σ_L and σ_R cannot be directly substituted into eq. 1.59 (which assumes both cross sections are measured at the same cm energy). For small helicity dependent systematic deviations from E_{cm} , the cross sections can be modified as follows:

$$\sigma_L(E_{cm}^L) \approx \sigma_L(E_{cm}^0) + \left. \frac{d\sigma_L}{dE} \right|_{E_{cm}^0} dE, \quad (4.11)$$

$$\sigma_R(E_{cm}^R) \approx \sigma_R(E_{cm}^0) + \left. \frac{d\sigma_R}{dE} \right|_{E_{cm}^0} dE, \quad (4.12)$$

where

$$E_{cm}^0 = \frac{1}{2} (E_{cm}^L + E_{cm}^R). \quad (4.13)$$

From eq. 1.59, A_{LR} is given by

$$A_{LR} = \frac{\sigma_L(E_{cm}^0) - \sigma_R(E_{cm}^0)}{\sigma_L(E_{cm}^0) + \sigma_R(E_{cm}^0)}. \quad (4.14)$$

Substitution of eqs. 4.11 and 4.12 into eq. 4.14 and expanding it to lowest order in the derivative of σ gives the correction term in eq. 4.6.

The source of this asymmetry lies in the fact that the accelerator can supply a maximum amount of energy to each bunch. This energy is in turn divided amongst all the particles in the bunch. If, for example, the LH electron bunches are systematically larger, then the average energy of the LH electrons will be smaller than that of the RH electrons, leading to an energy asymmetry.

Optimally, this asymmetry could be measured directly with the energy spectrometer. However, in the 1992 run, the energy spectrometer was not synchronized with the 120 Hz left/right beam information and could not be used (this problem has since been remedied). For the 1992 run, the beam current asymmetry was used to infer A_E . The entire correction factor $-E_{cm}(\sigma'_u/\sigma_u)A_E$ is equal to $(1.7 \pm 0.6) \times 10^{-5}$ which gives

$$\frac{\delta A_{LR}}{A_{LR}} = -(0.08 \pm 0.03)\%. \quad (4.15)$$

4.1.2.6 Summary of Helicity Dependent Effects

Table 4.1 is a summary of the helicity dependent corrections to A_{LR} and their systematic uncertainties.

Correction to A_{LR}	$\delta A_{LR}/A_{LR}(\%)$
Background fraction	2.0 ± 0.7
Polarization asymmetry	$-(6.5 \pm 0.2) \times 10^{-3}$
Luminosity asymmetry	$-(0.8 \pm 1.9)$
Response asymmetry	0
Energy asymmetry	$-(0.08 \pm 0.03)$
Total	2.0 ± 2.0

Table 4.1: Helicity dependent corrections to A_{LR} .

Because all but the f_b correction terms are either negligible or consistent with zero, a correction of $\delta A_{LR} = +0.002$ will be made for the background fraction, while the remaining terms will be included in the systematic uncertainty.

The analysis presented here is slightly different from that presented in [47]. There, f_b had been estimated to be $(1.4 \pm 1.4)\%$. No correction to A_{LR} was made and f_b was absorbed into the systematic error. The two calculations have a negligible deviation in the determination of A_{LR} . The contribution to the systematic error from f_b in the analysis presented here is smaller by a factor of 2.

4.1.3 Dependence on E_{cm} and Final States

To see the effect of the uncertainty in measuring E_{cm} on A_{LR} , the energy dependence of A_{LR} is described.

The assumption that $\frac{d\sigma_Z^Z}{d\Omega} \gg \frac{d\sigma_\gamma^Z}{d\Omega}$ (see section 1.3) leads to the cancelation of A_{LR} 's dependence on the final state fermions. Fig. 4.3 is a plot of A_{LR} versus E_{cm} for charged leptons, u -type and d -type quarks. The energy dependence results from the inclusion of the γ and $\gamma - Z^0$ interference terms. Without the photon channel, A_{LR} would be constant for all energies and final state particles. At $E_{cm} = M_Z$, where the $\gamma - Z^0$ interference term drops out, the values are not equal because the contribution

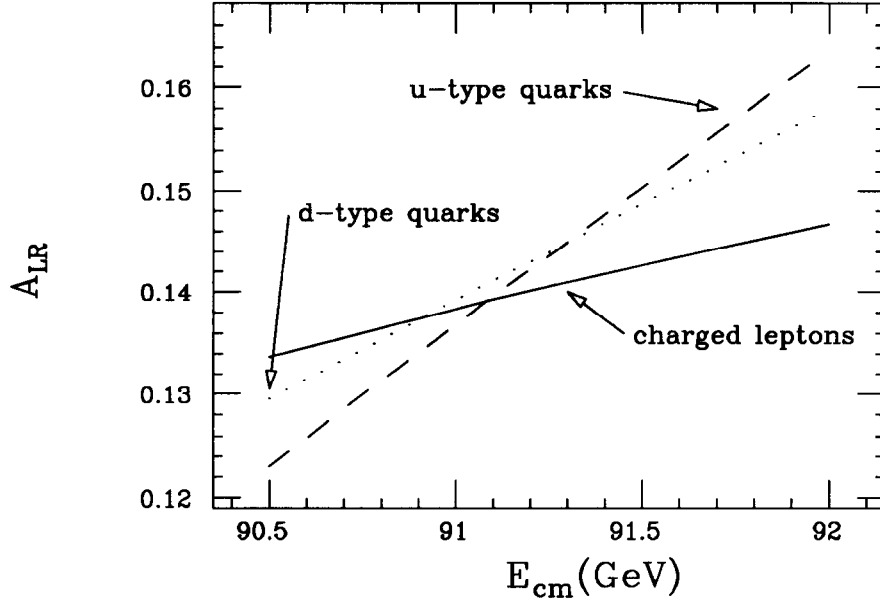


Figure 4.3: Energy dependence of A_{LR} for leptons and quarks [48]. Plot assumes $m_t = 150 \text{ GeV}/c^2$ and $M_H = 300 \text{ GeV}/c^2$.

of $\frac{d\sigma_\gamma}{d\Omega}$, to the denominator of eq. 1.59, is flavor dependent. The different slopes of A_{LR} for the different final states are a result of the contribution from the $\gamma - Z^0$ interference term.

Because the measured value of A_{LR} is a superposition of quark and tau decays of the Z^0 , theoretical quantities must be weighted by their partial decay width and the detector response function before being compared with experimental quantities. For any quantity X , the weighted average is calculated using the expression:

$$X = \frac{0.9 [3\Gamma_d X_d + 2\Gamma_u X_u] + 0.3\Gamma_\tau X_\tau}{0.9 [3\Gamma_d + 2\Gamma_u] + 0.3\Gamma_\tau}, \quad (4.16)$$

where each flavor dependent quantity, X_f , is weighted by the partial decay width Γ_f ($\Gamma_d = 0.383 \text{ GeV}$, $\Gamma_u = 0.298 \text{ GeV}$, and $\Gamma_\tau = 0.0835 \text{ GeV}$) [6], the number of fermion channels available for the decay (3 for d -type quarks, 2 for u -type quarks and 1 for taus) and the ϵ for each channel (0.9 for quarks and 0.3 for taus, see chapter 3).

Inclusion of the γ term in eq. 1.60 leads to a weighted average shift in A_{LR} (from

its pure Z^0 value) of

$$A_{LR}(\gamma \text{ and } Z^0) = A_{LR}(Z^0)(1 - 0.001). \quad (4.17)$$

At the level of precision presently attainable, this has a negligible effect and will be ignored. The weighted relative RMS deviation for the different flavors is

$$\frac{\delta A_{LR}(\gamma \text{ and } Z^0)}{A_{LR}(\gamma \text{ and } Z^0)} = 0.0035. \quad (4.18)$$

Thus, the dependence of A_{LR} on the final state is very weak.

In Fig. 4.4, the weighted A_{LR} for hadrons and taus is plotted versus E_{cm} . Also

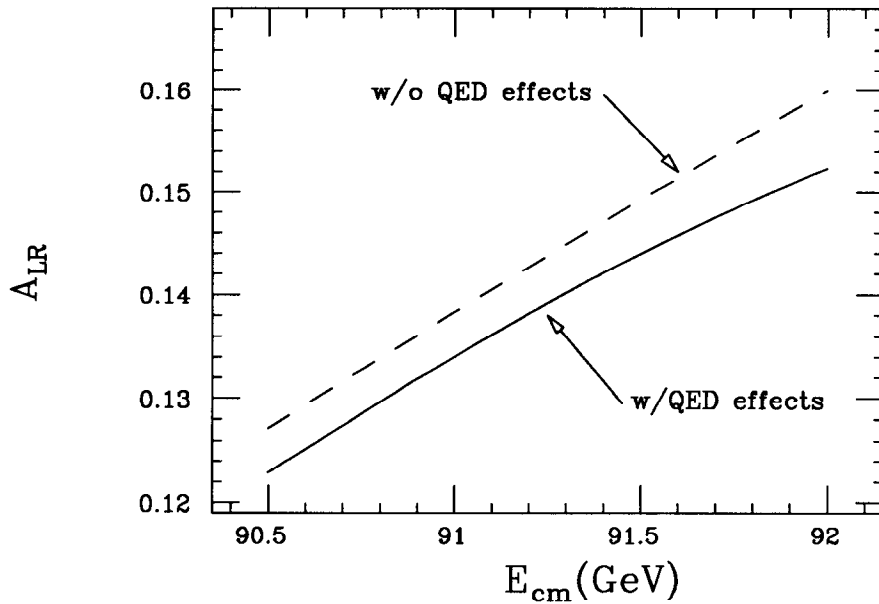


Figure 4.4: Energy dependence of A_{LR} for hadrons and taus [48]. The solid line includes initial and final state radiation, the dashed line does not. Plot assumes $m_t = 150 \text{ GeV}/c^2$ and $M_H = 300 \text{ GeV}/c^2$.

shown is the effect of the initial and final state radiation by the electron, positron and outgoing fermions on A_{LR} . The initial and final state radiation is described by the class of diagrams that add a photon to diagrams in Fig. 1.7. These photons can be either real bremsstrahlung or virtual loops. Because A_{LR} is nearly independent of

the final state, final state radiation has a negligible effect on A_{LR} . The initial state radiation effectively lowers the cm energy.

The average E_{cm} was measured to be (91.55 ± 0.04) GeV. The uncertainty in the energy measurement leads to an uncertainty in determining A_{LR} of

$$\delta A_{LR} = \pm 0.0007. \quad (4.19)$$

4.2 Theoretical Uncertainties

The experimentally measured value of A_{LR} includes the effects of many higher order radiative processes that must be “unfolded” from the experimental value before one can extract the value of $\sin^2 \theta_W^{eff}$ from eq. 1.73. Even though no theoretical corrections are made in determining the measured value of A_{LR} , a brief discussion of their effects and uncertainties is presented. The precision to which theoretical calculations can be made serves as the benchmark by which all experimental measurements are judged.

4.2.1 Initial and Final State Radiative Corrections

At $E_{cm} = 91.55$ GeV, the correction to A_{LR} from the initial and final state radiation is $+0.006$ (see Fig. 4.4). Even though the correction is relatively large, the theoretical uncertainty in calculating the effects of the radiation on the total Z^0 cross-section is estimated to be $\frac{\delta\sigma}{\sigma} \sim 4 \times 10^{-4}$ [49]. This translates into an uncertainty in A_{LR} of

$$\delta A_{LR} = \pm 0.0003. \quad (4.20)$$

4.2.2 QCD Contributions

As stated in section 4.1.3, the theoretical expression for A_{LR} (eq. 1.73) has a small dependence on the final state quarks due the γ -channel. An upper limit on the QCD contribution to A_{LR} has been estimated to be 0.0005 [50]. The uncertainty of the estimation is conservatively estimated to be the size of the contribution

$$\delta A_{LR} = \pm 0.0005. \quad (4.21)$$

4.2.3 Photon Vacuum Polarization Effects

The theoretical expression for A_{LR} is dependent on s_0^2 through eqs. 1.73 and 1.78. The dominant theoretical uncertainty in s_0^2 comes from the uncertainty in the calculation of the photon vacuum polarization which is absorbed in $\Delta\alpha$. The expression for $\Delta\alpha$ is [9]

$$\Delta\alpha = 0.0602 + \frac{40}{9} \frac{\alpha}{\pi} \ln \frac{M_Z}{92 \text{ GeV}} \pm 0.0009. \quad (4.22)$$

The theoretical uncertainty in calculating $\Delta\alpha$ leads to an uncertainty in A_{LR} of

$$\delta A_{LR} = \pm 0.0024. \quad (4.23)$$

This is the dominant theoretical error in calculating A_{LR} .

4.3 Statistical Uncertainty

The statistical uncertainty of A_{LR} is directly derived from eq. 4.1 to be

$$\delta A_{LR} = \sqrt{\frac{1 - (A_{LR}^{exp})^2}{P^2 N}} = \pm 0.044. \quad (4.24)$$

Note that doubling the polarization has the same effect on A_{LR} as quadrupling the event sample. For the present data sample (1992 run), the statistical uncertainty is by far the largest uncertainty in determining A_{LR} . For an electron beam with 70% polarization, the statistical uncertainty will equal the presently proposed limit of the systematic uncertainty (~ 0.0015) only at $N \approx 10^6$.

4.4 Result

Tables 4.2 and 4.3 summarize the experimental and theoretical uncertainties in determining A_{LR} . The total is the quadrature sum of the different contributions. Thus, the measured value for A_{LR} is

$$A_{LR}(E_{cm} = 91.55 \text{ GeV}) = 0.102 \pm 0.044(\text{stat}) \pm 0.003(\text{syst}), \quad (4.25)$$

where a small correction due to f_b has been made.

Systematic uncertainty	δA_{LR}
Polarization measurement	0.0027
Helicity dependent effects	0.0020
E_{cm} measurement	0.0007
Total	0.0034

Table 4.2: Experimental uncertainties in the measurement of A_{LR} .

Systematic uncertainty	δA_{LR}
Initial and final state radiative corrections	0.0003
QCD contribution	0.0005
Photon vacuum polarization	0.0024
Total	0.0025

Table 4.3: Theoretical uncertainties in calculating A_{LR} .

Chapter 5

Conclusions

The first measurement of A_{LR} has been successfully completed. Before the SLD value can be compared with other experimental measurements, it must be corrected for the effects of initial and final state radiation and the offset of the SLC E_{cm} from the Z^0 -pole energy (see Table 5.1). Correcting the value of A_{LR} in eq. 4.25 for these effects,

Effect	Correction to A_{LR}
Removal of initial/final state radiation	+0.006
E_{cm} offset from Z^0 -pole	-0.008
Total	-0.002

Table 5.1: Corrections to A_{LR} .

the “bare” value of A_{LR} , A_{LR}^0 , is found to be

$$A_{LR}^0 = 0.100 \pm 0.044(\text{stat}) \pm 0.003(\text{syst}). \quad (5.1)$$

Solving eq. 1.73 for $\sin^2 \theta_W^{eff}$, using the value of A_{LR}^0 , gives

$$\sin^2 \theta_W^{eff} = 0.2375 \pm 0.0056(\text{stat}) \pm 0.0004(\text{syst}). \quad (5.2)$$

In the literature, there is a myriad of expressions for quantities resembling $\sin^2 \theta_W$. There is no fundamental difference between the various quantities; the differences simply reflect which radiative corrections are included in the definition of the quantity. Naturally, before a comparison between any two definitions can be made, the radiative corrections excluded from a particular definition must still be accounted for.

The experiments described in sections 5.2 and 5.3 express their measurement of the electroweak mixing angle in terms of quantities whose definitions differ slightly from that of $\sin^2 \theta_W^{eff}$. Therefore, before discussing the measurements of the electroweak mixing angle by the assorted experiments, it will be shown how the definitions are related to each other.

To begin with, $\sin^2 \theta_W$, as defined in eq. 1.17, is referred to as the “bare” or tree-level (i.e. free of radiative corrections) expression. In addition to its expression in terms of g and g' , the electroweak coupling strengths, using the equations for the boson masses, given in Table 1.1 and eq. 1.15, $\sin^2 \theta_W$ can be written as

$$\sin^2 \theta_W = 1 - \frac{(M_W^0)^2}{(M_Z^0)^2}. \quad (5.3)$$

The “0” superscript has been added to the definitions of the vector boson masses given in section 1.2 to emphasize that these are the tree level definitions for the vector boson masses and not their *measured* values. Replacing M_W^0 and M_Z^0 with their experimentally measured values, M_W and M_Z , one arrives at the definition of $\sin^2 \theta_W$, renormalized to all orders in perturbation theory. In the literature, this renormalized quantity is commonly referred to as $\sin^2 \theta_W$, however, since that “label” has been used, the renormalized quantity will be labeled as

$$\sin^2 \theta_W^\nu = 1 - \frac{M_W^2}{M_Z^2}. \quad (5.4)$$

The reason for the “ ν ” superscript will soon become apparent.

A definition preferred by some theorists is the modified minimal-subtraction renormalization scheme parameter, $\sin^2(\theta_W)_{\overline{MS}}$. It is preferred because it incorporates the radiative corrections in a manner that facilitates theoretical calculations. At the Z^0 -pole, the two definitions are related by $\sin^2(\theta_W)_{\overline{MS}} = C(m_t, M_H) \sin^2 \theta_W^\nu$, where $C(m_t, M_H) = 1.009(1.054)$ for $m_t = 100(200)$ GeV/ c^2 and $M_H = 250$ GeV/ c^2 [51]. The quantity measured at SLD, $\sin^2 \theta_W^{eff}$, is related to $\sin^2(\theta_W)_{\overline{MS}}$ through the simple expression [52]:

$$\sin^2 \theta_W^{eff} = \sin^2(\theta_W)_{\overline{MS}} + 0.0006. \quad (5.5)$$

5.1 Comparison with LEP

Using unpolarized beams, LEP is able to determine A_e (eq. 1.61) through two different measurements. The most direct measurement is made by studying the longitudinal polarization of tau decays [53]. Measuring the polarization of the final state products, allows one to “invert” $A_{FB}^{pol,\tau}$ (eq. 1.70) into P_τ^{FB} , the polarized forward-backward asymmetry of taus. Thus, the initial state electron and positron become the “final” state particles. This relationship gives

$$P_\tau^{FB} = \frac{3}{4}A_e. \quad (5.6)$$

The second measurement of A_e comes from the unpolarized forward-backward asymmetry for electrons A_{FB}^e which is proportional to A_e^2 (eq. 1.66).

The universality between leptons is determined by their relative coupling strengths. LEP has measured these to be [6]

$$\begin{aligned} \frac{a_\tau}{a_e} &= 0.9990 \pm 0.0029, & \frac{v_\tau}{v_e} &= 1.00 \pm 0.13, \\ \frac{a_\mu}{a_e} &= 1.0006 \pm 0.0026, & \frac{v_\mu}{v_e} &= 0.77 \pm 0.21. \end{aligned} \quad (5.7)$$

The tau polarization, P_τ , is defined as the difference of cross sections for producing LH and RH taus divided by the total cross section (similar to A_{LR}). Therefore, assuming lepton universality, measurement of the tau polarization is equivalent to measuring A_e .

Fig. 5.1 is a comparison of the SLD A_e , its errors added in quadrature, with measurements made at LEP. The value of A_{LR} is clearly in line with the other measurements. With only $\sim 10^4$ events, the error on A_{LR} is comparable with individual measurements from LEP experiments that have accumulated $\sim 10^2$ times more data (Z^0 decays to all fermion flavors). For the various LEP measurements, the statistical and systematic uncertainties are of the same order of magnitude.

Fig. 5.2 compares the SLD $\sin^2 \theta_W^{eff}$ to measurements from LEP. The LEP values are averages of many individual measurements made by the different experiments. The LEP average value is an average of 25 separate measurements. The SLD value is within errors of the central value, but clearly does not have the same precision.

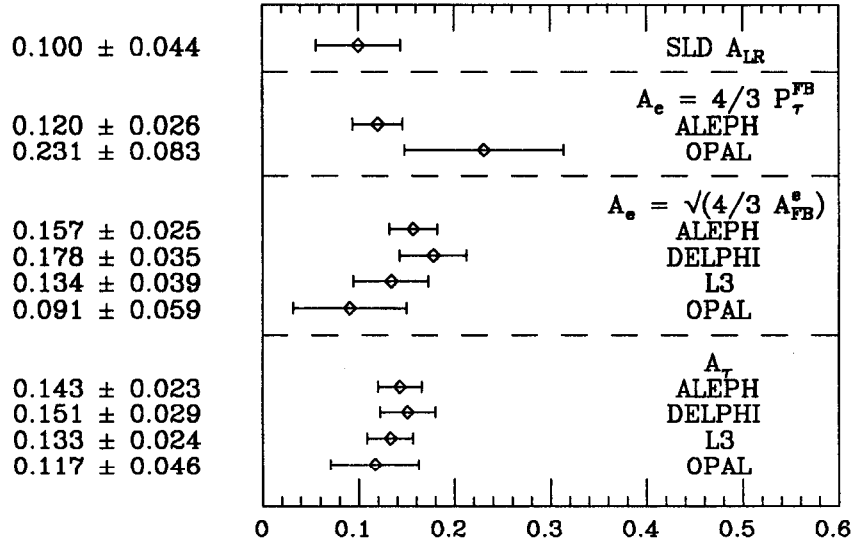


Figure 5.1: Comparison of A_e with LEP results [6].

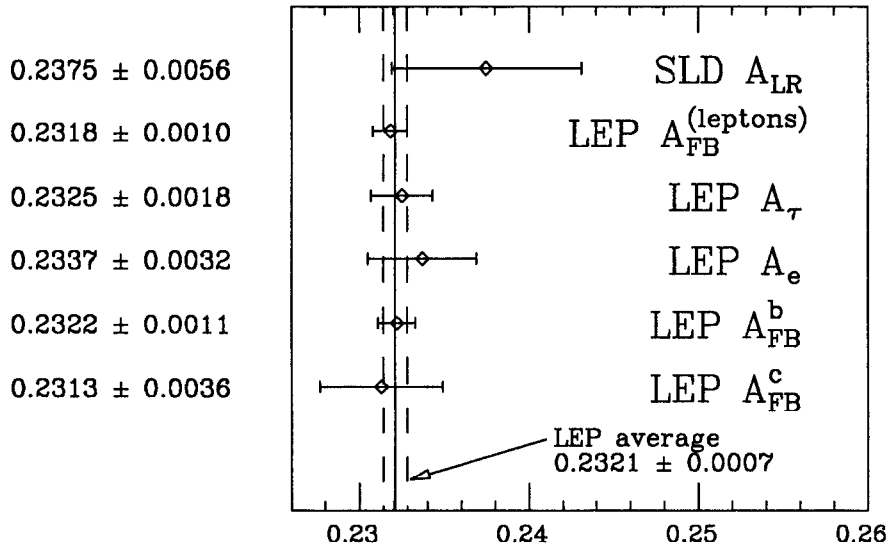


Figure 5.2: Comparison of $\sin^2 \theta_W^{eff}$ with LEP results [6].

5.2 Comparison with Neutrino Measurements

Measurements of the weak mixing angle have been made by scattering neutrinos off various targets. The two classes of neutrino experiments that have achieved reasonable high precision, relative to the Z^0 -pole measurements, are the deep inelastic $(\bar{\nu}_\mu)N$ scattering and the elastic $(\bar{\nu}_\mu)e$ scattering experiments.

The deep inelastic $(\bar{\nu}_\mu)N$ scattering experiments, which measure

$$R = \frac{\sigma(\nu_\mu N \rightarrow \nu_\mu N)}{\sigma(\nu_\mu N \rightarrow \mu X)}, \quad (5.8)$$

are presently the most precise neutrino measurements. The results of the experiments are typically expressed in terms of $\sin^2 \theta_W^\nu$. The current world average [52] of $\sin^2 \theta_W^\nu = 0.2304 \pm 0.0024(\text{expt}) \pm 0.0050(\text{theory})$ from deep inelastic neutrino measurements translates into

$$\sin^2 \theta_W^{eff} = \begin{cases} 0.2331 \pm 0.0024(\text{expt}) \pm 0.0050(\text{theory}), & m_t = 100 \text{ GeV}/c^2, \\ 0.2434 \pm 0.0024(\text{expt}) \pm 0.0050(\text{theory}), & m_t = 200 \text{ GeV}/c^2, \end{cases} \quad (5.9)$$

with $M_H = 250 \text{ GeV}/c^2$. An experiment presently being assembled at Fermilab, E-815, proposes to eventually determine $\sin^2 \theta_W^\nu$ to a precision of ± 0.0012 [54] by studying deep inelastic $(\bar{\nu}_\mu)N$ scattering.

The elastic $(\bar{\nu}_\mu)e$ scattering experiments measure the purely leptonic cross sections, $\sigma(\nu_\mu e \rightarrow \nu_\mu e)$ and $\sigma(\bar{\nu}_\mu e \rightarrow \bar{\nu}_\mu e)$. The CHARM II experiment measured $\sin^2(\theta_W)_{MS}$ to be 0.2325 ± 0.0092 [55, 52]. This corresponds to $\sin^2 \theta_W^{eff} = 0.2331 \pm 0.0092$.

5.3 Comparison with Atomic Measurements

The measurements of $\sin^2 \theta_W^{eff}$ made by the high energy experiments are complemented by the study of atomic parity violating effects, occurring in optical transitions, which result from the exchange of Z^0 's between the atomic electrons and the quarks in the nucleus. The most precise atomic measurement of $\sin^2 \theta_W^{eff}$ to date has

been measured in cesium to be [56, 57]

$$\sin^2 \theta_W^{eff} = \begin{cases} 0.2248 \pm 0.0065(\text{expt}) \pm 0.0036(\text{theory}), & m_t = 100 \text{ GeV}/c^2, \\ 0.2215 \pm 0.0065(\text{expt}) \pm 0.0036(\text{theory}), & m_t = 200 \text{ GeV}/c^2, \end{cases} \quad (5.10)$$

where the results in ref. [57], given in terms of $\sin^2(\theta_W)_{\overline{MS}}$, have been converted to $\sin^2 \theta_W^{eff}$ using eq. 5.5.

A recent measurement [58] of the parity violating optical rotation in lead vapor¹ had a 1% absolute experimental uncertainty in determining $\sin^2 \theta_W^{eff}$. However, the absolute theoretical uncertainty for that measurement is currently at the 8% level. Measuring the optical rotation in thallium, where the potential for reducing the theoretical uncertainty is greater, could potentially be the most sensitive of all atomic measurements in the determination of $\sin^2 \theta_W^{eff}$.

5.4 Summary

The ability to produce high energy, polarized electron beams has been demonstrated. The polarization is routinely measured to high precision. The measured value of A_{LR} (and thus, $\sin^2 \theta_W^{eff}$) is consistent with LEP, neutrino scattering and atomic parity violating measurements. Because the measurement is unique (presently only SLAC can measure A_{LR}), it also serves as a complementary check of the LEP measurements. Unfortunately, the current level of precision attained in measuring $\sin^2 \theta_W^{eff}$ (the absolute uncertainty was 2%) fell below the $\sim 0.1\%$ absolute uncertainty needed to be sensitive to m_t , M_H and any physics beyond the MSM.

5.5 Future Prospects

SLC/SLD has recently completed a 1993 data taking run. SLD accumulated $\sim 5 \times 10^4$ Z^0 's with $\sim 62\%$ electron polarization. The new measurement of A_{LR} is not yet available, but with the higher statistics and an improved systematical error, the combined

¹Polarized light, passing through the lead vapor, is rotated by an angle that is a function of the parity violating interaction.

error on $\sin^2 \theta_W^{eff}$ should be ~ 0.001 . There is presently a proposal to run for several more years to collect $10^6 Z^0$ decays with $P_e \approx 70\%$. Assuming a relative systematic error of 1% in A_{LR} , the precision in determining A_{LR} will be $\delta A_{LR} = \pm 0.0024$ ($\delta \sin^2 \theta_W^{eff} = \pm 0.0003$) which is at the level of the theoretical uncertainty. This single measurement will be highly competitive with the average of 25 measurements from LEP.

What can be done with such high precision? Fig. 5.3 demonstrates the sensitivity of $\sin^2 \theta_W^{eff}$ to m_t (for several values of M_H). Assuming $60 < M_H$ (in GeV/c^2) < 1000 ,

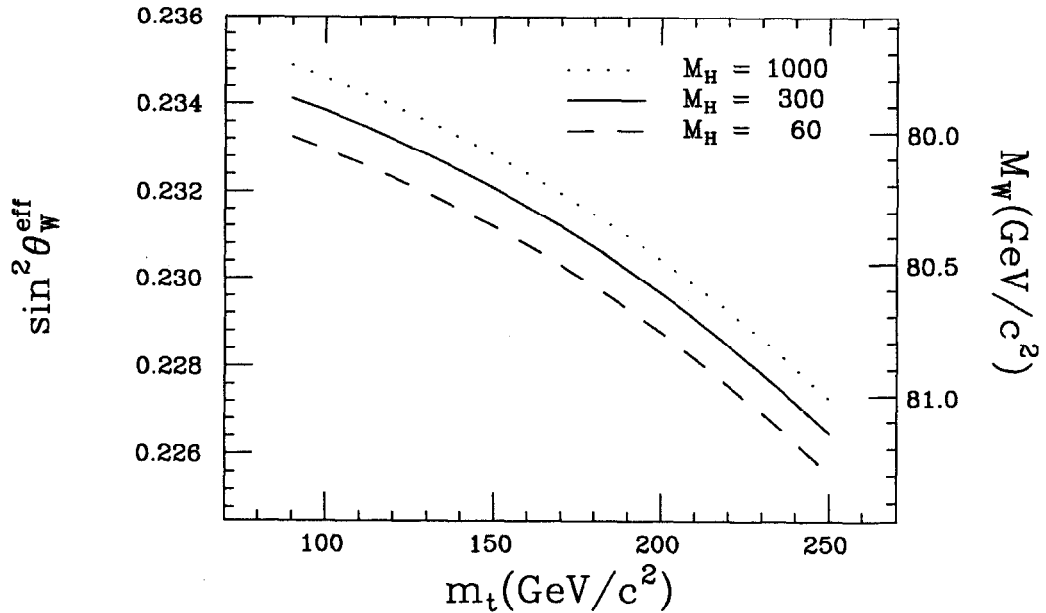


Figure 5.3: $\sin^2 \theta_W^{eff}$ (and M_W) versus m_t [48].

m_t can be constrained to $\pm 25 \text{ GeV}/c^2$. If, for example, the top is discovered and measured to be $(150 \pm 5) \text{ GeV}/c^2$, then M_H can be constrained to a few hundred GeV/c^2 (see Fig. 5.4). Alternatively, $\sin^2 \theta_W^{eff}$, which measures the ratio of the vector and axial-vector couplings through the expression:

$$\sin^2 \theta_W^{eff} = \frac{1}{4} \left(1 - \frac{v_e^{eff}}{a_e^{eff}} \right) \quad (5.11)$$

can be compared with the partial decay width of the Z^0 into electrons, Γ_{ee} . For

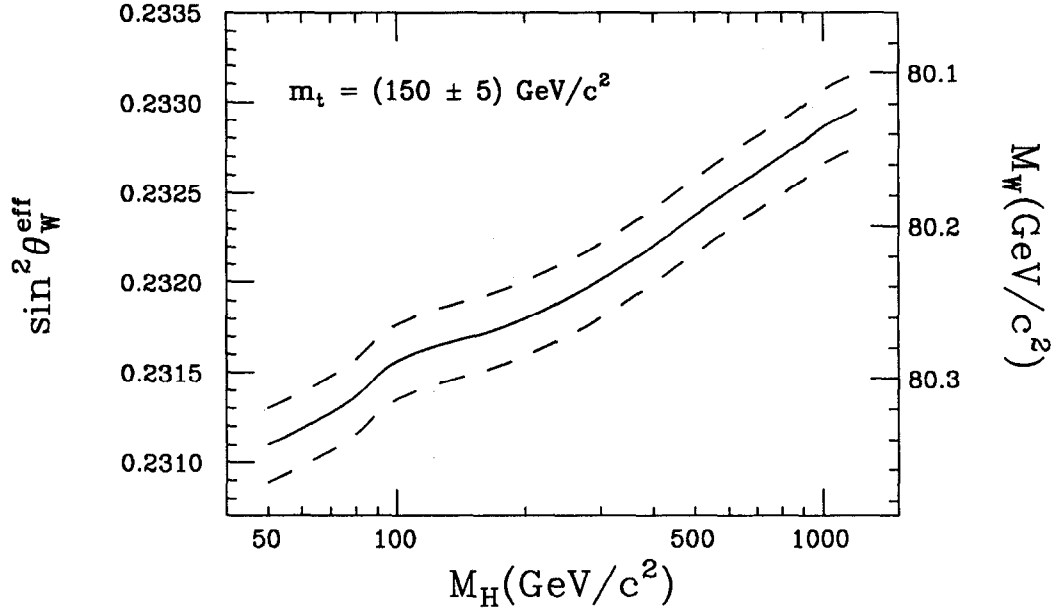


Figure 5.4: $\sin^2 \theta_W^{eff}$ (and M_W) versus M_H [48].

massless electrons, Γ_{ee} is

$$\Gamma_{ee} = \frac{G_F M_Z^3}{6\pi\sqrt{2}} \left[(v_e^{eff})^2 + (a_e^{eff})^2 \right] (1 + \delta_{QED}), \quad (5.12)$$

where δ_{QED} accounts for photon corrections. Note that Γ_{ee} is a function of the quadrature sum of the vector and axial-vector couplings. Fig. 5.5 is a plot of $\sin^2 \theta_W^{eff}$ versus Γ_{ee} . The current LEP value for Γ_{ee} , (83.86 ± 0.30) MeV, is overlaid on the plot [6].

For comparison, Figs. 5.3–5.5 demonstrate the dependence of M_W on m_t , M_H , and Γ_{ee} . An error of ± 0.0003 in $\sin^2 \theta_W^{eff}$ corresponds to a measurement of M_W to a precision of ± 0.04 GeV/ c^2 , well below the current precision of ± 0.26 GeV/ c^2 [59].

In the near future, measurement of A_{LR} will not only be complementary to measurements at LEP, but will be highly competitive with them. The precision attainable in measuring A_{LR} will make it a sensitive probe into the limits of the standard model, hopefully leading to exciting new discoveries!

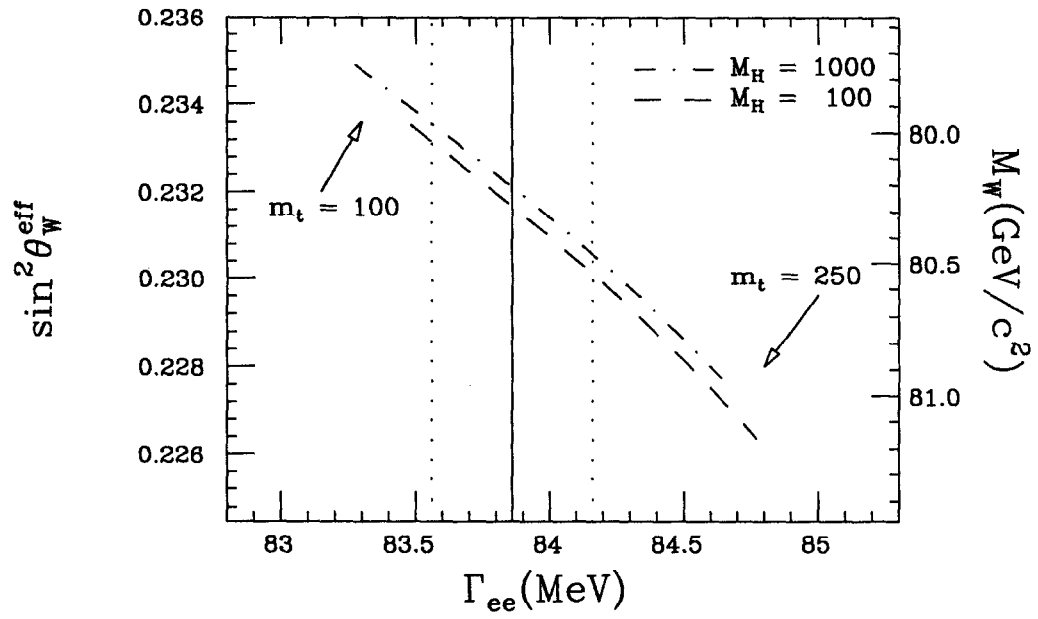


Figure 5.5: $\sin^2 \theta_W^{eff}$ (and M_W) versus Γ_{ee} [48].

Bibliography

- [1] J.D. Jackson, *Classical Electrodynamics*, 2nd edition, John Wiley & Sons, New York, (1975).
- [2] H. Fritzsch, M. Gell-Mann, and H. Leutwyler, *Phys. Lett.* **B47**, 365 (1973); S. Weinberg, *Phys. Rev. Lett.* **31**, 494 (1973); D. Gross and F. Wilczek, *Phys. Rev.* **D8**, 3633 (1973).
- [3] S.L. Glashow, *Nucl. Phys.* **22**, 579 (1961); S. Weinberg, *Phys. Rev. Lett.* **19**, 1264 (1967); A. Salam, *Elementary Particle Theory: Relativistic Groups and Analyticity* (8th Nobel Symposium), ed. N. Svartholm, Almqvist and Wiksell, Stockholm, 367 (1968).
- [4] F. Halzen and A.D. Martin, *Quarks and Leptons: An Introductory Course in Modern Particle Physics*, John Wiley & Sons, New York, (1984).
- [5] Particle Data Group, *Phys. Rev.* **D45**, III.1 (1992).
- [6] The LEP Collaborations, CERN/PPE/93-157, (August 1993).
- [7] Particle Data Group, *Phys. Rev.* **D45**, VII.144 (1992).
- [8] G. Altarelli, R. Barbieri and S. Jadach, *Nucl. Phys.* **B376**, 444 (1992); G. Altarelli, R. Barbieri and S. Jadach, *Nucl. Phys.* **B369**, 3 (1992).
- [9] M. Consoli, W. Hollik and F. Jegerlehner, in *Z Physics at LEP 1*, eds. G. Altarelli, R. Kleiss and C. Verzegnassi, CERN 89-08, vol. I, 7 (1989).
- [10] J.T. Seeman, *Annu. Rev. Nucl. Part. Sci.* 41:389 (1991).

- [11] N. Phinney, SLAC-PUB-5864, (August 1992), in *Proceedings of the XXVI International Conference on High Energy Physics (ICHEP92)*, p. 1971, ed. J.R. Sanford, Dallas, TX, August 1992.
- [12] M. Woods, J. Frisch, K. Witte and M. Zolotarev, SLAC-PUB-5965, (December 1992), presented at the *Workshop on Polarized Electron Sources and Electron Spin Polarimeters*, Nagoya, Japan, November 1992.
- [13] D.C. Schultz, J. Clendenin, J. Frisch, E. Hoyt, L. Klaisner, M. Woods, D. Wright and M. Zolotarev, SLAC-PUB-5768, (March 1992), presented at the *3rd European Particle Accelerator Conference*, Berlin, Germany, March 1992.
- [14] M.L. Swartz, SLAC-PUB-4656, (June 1988), presented at the *SLAC Summer Institute on Particle Physics*, Stanford, CA, August 1987.
- [15] N.W. Ashcroft and N.D. Mermin, *Solid State Physics*, Saunders College, Philadelphia, (1976).
- [16] G.S. Abrams *et al.* (Mark II Coll.), *Phys. Rev. Lett.* **63**, 2173 (1989).
- [17] T. Hansl-Kozanecka and J.M. Yamartino, SLD Physics Note #7, (July 1990).
- [18] M.L. Swartz, SLAC-PUB-4689, (July 1988), in *Polarization at LEP*, eds. G. Alexander, G. Altarelli, A. Blondel, G. Coignet, E. Keil, D.E. Plane and D. Treille, CERN 88-06, vol. II, 163 (1988).
- [19] G. Blaylock, SLD Physics Note #22, (June 1993); J. Kent *et al.*, SLAC-PUB-4922, (March 1989), presented at the *IEEE Particle Accelerator Conference*, Chicago, IL, March 1989.
- [20] S. Drell, SLD Note #226, (September 1992).
- [21] C.Y. Prescott, SLAC-TN-73-1, (January 1973).
- [22] M. Fero *et al.*, SLAC-PUB-6026, (December 1992), presented at the *Workshop on Polarized Electron Sources and Electron Spin Polarimeters*, Nagoya, Japan, November 1992.

- [23] M. Fero, D. Calloway, R. Elia and A. Lath, SLD Note #221, (October 1992).
- [24] B. Schumm and R. Elia, SLD Note #222, (November 1992).
- [25] *SLD Design Report*, SLAC-Report-273, (1984).
- [26] C.J.S. Damerell *et al.*, in *Proceedings of the XXVI International Conference on High Energy Physics (ICHEP92)*, p. 1862, ed. J.R. Sanford, Dallas, TX, August 1992; M.G. Strauss *et al.*, in the proceedings of the *7th Meeting of the American Physical Society, Division of Particles and Fields (DPF 92)*, p. 1758, eds. C.H. Albright, P.H. Kasper, R. Raja and J. Yoh, Batavia, IL, November 1992.
- [27] G. Charpak and F. Sauli, *Annu. Rev. Nucl. Part. Sci.* 34:285 (1984).
- [28] T. Markiewicz and L. Rochester, SLD Note #231, (March 1993).
- [29] J. Va'vra *et al.*, SLAC-PUB-6276, (June 1993), presented at the *First Workshop on RICH Detectors*, Bari, Italy, June 1993.
- [30] D. Axen *et al.*, *Nucl. Instr. and Meth.* A328, 472 (1993); E. Vella *et al.*, SLAC-PUB-6026, (October 1992), presented at the *3rd International Conference on Calorimetry in High Energy Physics*, Corpus Christi, TX, September 1992.
- [31] E. Vella, private communication.
- [32] A.C. Benvenuti *et al.*, *Nucl. Instr. and Meth.* A289, 463 (1990); G.M. Bilei *et al.*, SLAC-PUB-5713, (January 1992), presented at the *2nd International Conference on Calorimetry in High Energy Physics*, Capri, Italy, October 1991.
- [33] S.C. Berridge *et al.*, *IEEE Transactions on Nuclear Science*, NS-37, 1191 (1990); S.C. Berridge *et al.*, *IEEE Transactions on Nuclear Science*, NS-39, 1242 (1992).
- [34] K. Pitts, SLD Physics Note #20, (April 1993).

- [35] The result is based on the measurement made by P.N. Burrows, H. Park, K.T. Pitts, and J.M. Yamartino in SLD Note #229, (January 1993). The affect of the fourth stage in the filter process lowers their result of $(91 \pm 2)\%$ to $(90 \pm 2)\%$.
- [36] J.J. Russell, private communication.
- [37] J.D. Fox *et al.*, *Nucl. Phys. B* (Proc. Suppl.) **23A**, 227 (1991).
- [38] E. Vella and J. Yamartino, SLD Note #213, (February 1992).
- [39] M. Breidenbach, presented at the *SLD Collaboration Meeting*, Stanford, CA, September 1992; H. Band, presented at the *SLD Collaboration Meeting*, Saratoga, CA, April 1992.
- [40] H. Park, R. Ben-David, R. Dubois, R. Frey and P.C. Rowson, SLD Physics Note #17, (March 1993).
- [41] R. Ben-David and H. Park, SLD Physics Note #18, (July 1993).
- [42] L. Rolandi, CERN-PPE/92-175, in *Proceedings of the XXVI International Conference on High Energy Physics (ICHEP92)*, p. 56, ed. J.R. Sanford, Dallas, TX, August 1992.
- [43] F.E. Low, *Phys. Rev. Lett.* **14**, 238 (1965).
- [44] P. Abreu *et al.* (DELPHI Coll.), *Phys. Lett.* **B268**, 296 (1991); O. Adriani *et al.* (L3 Coll.), *Phys. Lett.* **B288**, 404 (1992); M. Akrawy *et al.* (OPAL Coll.), *Phys. Lett.* **B257**, 531 (1991).
- [45] A.G. Frodesen, O. Skjeggstad, and H. Tøfte, *Probability and Statistics in Particle Physics*, Universitetsforlaget, (1979).
- [46] D.A. Evans and W.H. Barkas, *Nucl. Instrum. Methods* **56**, 289 (1967).
- [47] K. Abe *et al.* (SLD Coll.), *Phys. Rev. Lett.* **70**, 2515 (1993).

- [48] Figure was generated using a version of the analytical program *ZSHAPE*, modified to include electron polarization. All figures were generated with $M_Z = 91.187 \text{ GeV}/c^2$. *ZSHAPE* is described in *Z Physics at LEP 1*, eds. G. Altarelli, R. Kleiss and C. Verzegnassi, CERN 89-08, vol. III, 50 (1989). The modification is described in a *SLD Electroweak Memo* by J.M. Yamartino, (December 1992).
- [49] S. Jadach, M. Skrzypek and M. Martinez, *Phys. Lett.* **B280**, 129 (1992).
- [50] B.W. Lynn and C. Verzegnassi, *Phys. Rev.* **D35**, 3326 (1987).
- [51] Particle Data Group, *Phys. Rev.* **D45**, III.59 (1992).
- [52] W.J. Marciano, in the proceedings of the *7th Meeting of the American Physical Society, Division of Particles and Fields (DPF 92)*, p. 185, eds. C.H. Albright, P.H. Kasper, R. Raja and J. Yoh, Batavia, IL, November 1992.
- [53] S. Jadach and Z. Wąs, in *Z Physics at LEP 1*, eds. G. Altarelli, R. Kleiss and C. Verzegnassi, CERN 89-08, vol. I, 235 (1989).
- [54] R.H. Bernstein, *Nucl. Phys. B (Proc. Suppl.)* **31**, 255 (1992).
- [55] G. Rädcl, representing the CHARM II Coll., in the proceedings of the *7th Meeting of the American Physical Society, Division of Particles and Fields (DPF 92)*, p. 415, eds. C.H. Albright, P.H. Kasper, R. Raja and J. Yoh, Batavia, IL, November 1992.
- [56] M.C. Noecker, B.P. Masterson and C.E. Wieman, *Phys. Rev. Lett.* **61**, 310 (1988).
- [57] S.A. Blundell, W.R. Johnson and J. Sapirstein, *Phys. Rev. Lett.* **65**, 1411 (1990).
- [58] D.M. Meekhof, P. Vetter, P.K. Majumder, S.K. Lamoreaux and E.N. Fortson, *Phys. Rev. Lett.* **71**, 3442 (1993).
- [59] Particle Data Group, *Phys. Rev.* **D45**, II.1 (1992).